Identified Particle Spectra from dE/dx Ionization Measurements in Pb + Pb Collisions at 158 A·GeV/c

By

Jason Warren Dunn

B.S. (University of California, Davis) 1991

M.S. (University of California, Davis) 1995

Submitted in partial satisfaction of the requirements for the degree of

DOCTOR OF PHILOSOPHY

in

PHYSICS

in the

GRADUATE DIVISION

of the

UNIVERSITY OF CALIFORNIA

DAVIS

Approved:

Committee in charge

1997

Abstract

The NA49 collaboration studies nuclear matter under extreme conditions of temperature and pressure, specifically in Pb+Pb fixed target collisions at 158 A·GeV/c. The goal is the observation and study of the phase transition between hadronic matter and the Quark-Gluon Plasma(QGP), a deconfined state of freely propagating quarks and gluons. The NA49 experiment is a large acceptance hadron spectrometer comprised of four Time Projection Chambers(TPC's), which record the trajectories of a large fraction of the charged particles produced in the collision. Particle identification is made possible by measuring the specific energy loss, dE/dx, of charge particles in the relativistic rise regime.

This thesis describes the dE/dx analysis procedure in the Main TPC's, including the corrections to the raw dE/dx signal, the parametrization of the dE/dx information, and the statistical deconvolution of the different particle species. The rapidity(y) and transverse momentum(p_T) distributions of charged pions will be presented, including the total yields of π^+ and π^-, and their inverse slope parameters(effective temperatures). In addition, the pion low-p_T excess and coulomb effect are measured and discussed. Finally the implications of the measured pion yields on the entropy production and thus QGP formation will be explored.

Acknowledgements

I would like to thank my advisor, Dr. Paul Brady, for the opportunity to take part in an international collaboration with the reputation of the CERN experiment NA49. It was more than I bargained for, but in a good way ; -). I am also thankful for his ideas, support, and sense of humor.

I am also thankful to Dr. Daniel Cebra, who gave generously of his advice and knowledge over the years. In return I hit many a home run and sank many a basket for his physics IM sports teams. Thanks Sparky.

I am extemely grateful to my fellow NA49 mates, Lynn Wood and Isaac Huang. Lynn was one of my primary software advisors, and I would have never got up to speed on UNIX, PAW, C and the like without his help. Isaac helped me stay sane during our CERN exile, and was extremely helpful during the preparation of this thesis.

I cannot forget the constant support of my wife, Susie. She not only did the first proofread of this thesis, but encouraged me the whole way whenever I was worn out and wanted to quit.

Dedication

This thesis is dedicated to

my God,

my wife,

and my parents.

Contents

List of Figures

List of Tables

Chapter 1

Introduction to Heavy Ion Collisions

1.1 Theoretical Motivation

The primary motivation for colliding relativistic heavy ions is the study of strongly interacting nuclear matter. We want to understand the behaviour of this bulk matter at extreme values of density and temperature. Statistically based lattice Quantum ChromoDynamics(QCD) calculations predict a transformation from a hadron gas, where quarks are bound within individual hadrons, into a deconfined plasma of interacting quarks and gluons at sufficiently high densities and temperatures.

The attempt to create and study the Quark-Gluon Plasma(QGP) has many implications in several fundamental scientific areas. If we can create the QGP in the lab, it will allow us to study a new state of matter which is not seen anywhere else in the Universe, except possibly in such exotic places as the cores of neutron stars. It will allow us to confirm and test some of the fundamental parameters of QCD, one of the foundations of the Standard Model. Studying the QGP also plays a fundamental role in understanding Big Bang Cosmology. The universe probably underwent a transition from the QGP to confined nuclear matter around 10^{-5} seconds after the big bang, when the energy density fell below a few GeV/fm^3. At these energy densities, the deconfined plasma started to hadronize and form particles. The exact path that was followed during hardonization is relevant to understanding such questions as the matter/anti-matter ratios, the missing mass 'dark mass' problem, and whether the Universe is open or closed.

Collisions of ultra-relativistic heavy ions provide us the only known laboratory for creating and studying the QGP. Although we are not absolutely certain at what energy densities and temperatures the plasma will be formed, we believe the NA49 experiment is at or near the threshold of the conditions necessary to create such a state. The primary goal of NA49 and future experiments at the Relativistic Heavy Ion Collider(RHIC) at the Brookhaven National Laboratory(BNL) and the Large Hadron Collider(LHC) at CERN is to understand the transition to and the properties of the quark-gluon plasma.

Table 1.1: Some properties of the various quarks and leptons that make up the 3 generations of the Standard Model.

Quark	Charge	Mass(MeV)	Lepton Doublet
up(u)	2/3	5.6±1.1	e
down(d)	-1/3	9.9±1.1	ν_e
charm(c)	2/3	1350±50	μ
strange(s)	-1/3	199±33	ν_μ
top(t)	2/3	~180000	τ
bottom(b)	-1/3	~5000	ν_τ

1.2 Standard Model of Quarks

Since the existence of quarks was first postulated by Gell-Mann[Gell64] in 1964, to the discovery of the first evidence for quarks at SLAC in the late 60's and early 70's, to the discovery of the last predicted quark at Fermilab recently[Abe95, Abac95], the Standard Model of quarks has been one of the most successful and fruitful physics theories of all time. The Standard Model predicts, and experiments have shown, that there are six flavours of quarks paired into three doublets. Each quark doublet, together with a corresponding lepton doublet form a complete generation. Table 1.1 shows some of the properties of each of the 3 generations of the Standard Model of quarks and leptons. Each of the quarks are fractionally charged, and are fermions with spin 1/2. Furthermore each quark comes in one of three colour "charges", either red, green, or blue. Baryons are made of three quarks or three anti-quarks, while mesons are made of quark/anti-quark pairs.

Colour "charge" was first introduced such that baryons made of the same three quark flavors(such as the Δ^-(ddd)) could obey the Pauli principle. Without the colour quantum number the quarks would all have the same quantum numbers and thus have a symmetric wavefunction, which is not allowed for fermions.

The theory used to describe the colour force between the strongly interacting quarks is known as Quantum Chromodynamics(QCD). QCD[Gros73, Wein73] is a gauge field theory based on the non-Abelian SU(3) gauge group. The gauge field quanta or mediator of the colour force is the massless gluon. Gluons are themselves bi-coloured and thus directly carry and exchange colour. This is in contrast to QED, where the carriers of the electromagnetic(EM) force, the photons, carry no electric charge themselves. This feature of non-Abelian theories allows for 'self-interactions' between the gluons themselves, and leads to vastly different properties of the strong force as opposed to the EM force. The most important difference is the phenomenon of confinement, where coloured objects are trapped inside colour neutral states while keeping their apparent freedom within the colourless hadron.

1.3 Confinement

The confinement of quarks within hadrons can be understood in terms of the colour field lines between two colour sources(quarks), and the resulting potential which is produced[Chen84]. The potential takes the form

$$V(r) \sim \frac{\alpha_s}{r} + \sigma r.$$

At large separations the 2nd term of this potential dominates, requiring an infinite amount of energy to fully separate two quarks. As the separation of the quarks increases, a constant area colour flux tube or 'string'[Namb74] of strongly interacting quarks and gluons forms between the two quarks. The σ in the second term of the potential describes the tension of this string, where $r > 1fm$. As you try to separate two quarks, the potential energy held in the string grows. This rising potential energy coupled with a finite effective quark mass allows the colour string to then split into quark-antiquark pairs, creating quark loops which still conserve colour. As previously mentioned, the gluons carrying the colour force are capable of interacting with other gluons and splitting into two gluons(3 and 4 gluon-vertices). The combination of quark-antiquark pair production and gluon self-interactions leads to a net increase of the colour field in the flux tube as you try to separate the two quarks. This colour anti-screening increases the force as r increases, leading to confinement. This is completely opposite to the scenario in QED, where the EM force is decreased at large distances due to the dielectric screening by the cloud of virtual electron-positron pairs.

At small separations, the quark-quark potential is dominated by the 1/r term, which is pre-dominantly a one gluon exchange potential similar to the Coulomb potential. The constant of the 1/r term, the strong coupling constant α_s , is a running coupling constant which is dependent upon the momentum transfer, q. This coupling constant decreases logarithmically with increasing momentum transfers(small distances). Since α_s approaches zero faster than r, at very small distances the colour force between quarks approaches zero. This phenomenon is referred to as 'asymptotic freedom', as we expect asymptotic freedom for quarks at these momentum and distance scales. This is in agreement with the asymptotic freedom of quarks found in deep in-elastic scattering experiments[Bura80].

1.4 Colour Deconfinement and the QGP

In the high density limit of closely packed colour objects, the property of asymptotic freedom has been taken as an indication that deconfinement may occur. Collisions of relativistic heavy ions allow for the possibility of creating these high nuclear density environments, and probing whether this property may hold for collisions of a system of colour objects rather than for just a single quark within a hadron. In the unique environment of heavy ion collisions, multiple hadrons may be able to overlap with each other, causing each quark in the overlap region to be in close proximity with another quark from a neighbouring nucleon. The concept of an individual nucleon becomes meaningless, and quarks become free to propagate throughout the extended volume of the compressed region. A similar effect will be produced if the colliding nucleons are interacting at higher temperatures, where higher average kinetic energies will lead to ever increasing nuclear overlaps. The prediction for sufficiently high densities and/or temperatures is that a phase transition from quark confined hadronic matter to a plasma of deconfined quarks and gluons will take place. This new state of matter is commonly called the Quark-Gluon Plasma(QGP), and is the holy grail of heavy ion experiments.

The notion that the QGP can be created from either the compression or heating of nuclear matter leads to a critical transition curve in the phase diagram of strongly interacting matter, as shown in Fig. 1.1. In the figure T is the temperature and ρ is the baryon density expressed in units of ρ_0, where ρ_0 is normal nuclear matter density. A transition into the QGP region can be accomplished through various combinations of heating and compression. From the first moment of the Big Bang, the matter of the early universe was thought to be in the QGP state[vanH84] at extremely high temperatures but low baryon densities. As the matter expanded and cooled, hadronization began and matter settled into the states of normal, cool nuclear matter seen today. Alternatively, a cold QGP[Coll75] may exist inside neutron stars at incredibly large densities but relatively low temperatures. In heavy ion collisions the route to the QGP involves a trajectory somewhere in between these two extremes, where both the density and temperatures increase significantly above normal nuclear matter during the collision.

In recent years much theoretical and computing effort has been invested in obtaining estimates of the critical density ρ_c and critical temperature T_c necessary for

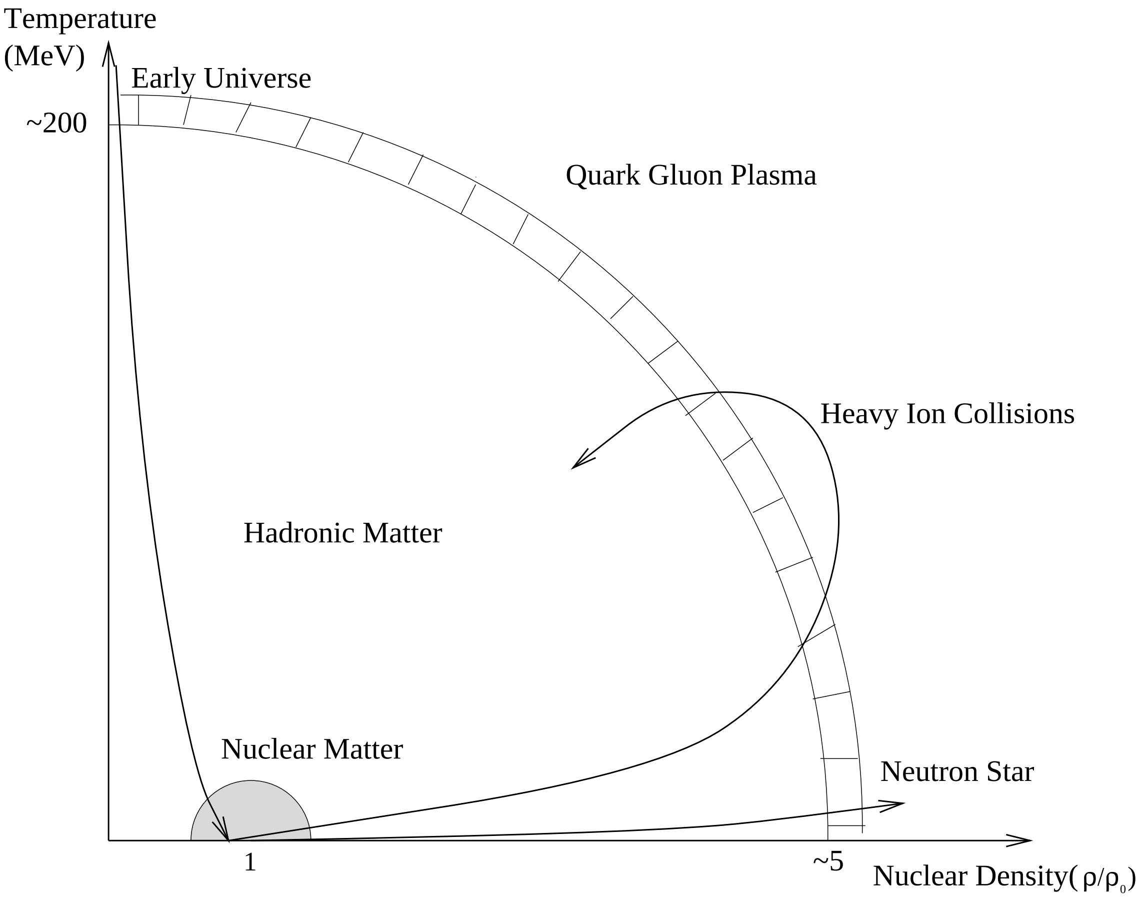

Figure 1.1: The phase diagram of nuclear matter in the temperature-nuclear density plane. Normal nuclear matter is indicated by the shaded region. Quark-gluon plasma conditions are believed to exist beyond the hatched arc at high temperatures and/or densities.

creation of the QGP. This problem has been addressed both in lattice formulations and in various effective Lagrangian methods. When the effective coupling constant α_s is small, perturbative QCD has been used to produce reliable results. But when α_s is large this approach breaks down and QCD predictions cannot be calculated in a quantitative fashion.

Lattice calculations may provide the most efficient approach to solving these QCD problems. In the computer simulation of statistical QCD on a lattice[Wils74] one tries to calculate the relevant quantities from first principles, without any simplifying assumptions. At present, the quantitative results of this approach are limited by the technical restrictions of the computer. Nonetheless the results of lattice QCD give us a reasonably good understanding of the critical behaviour of strongly interacting matter.

Fig. 1.2 shows a recent result of lattice QCD calculations of the critical parameters for two light quark flavours[Kars95]. One sees that at a critical temperature $T_c (T_c \sim 150 MeV)$, the energy density undergoes a rapid transition from low values, corresponding to a hardon gas, to much higher values, corresponding to a quark-gluon plasma. The ratio of the energy densities of the hadron gas to the QGP is related to the ratio of the degrees of freedom of the two states. The QGP has many more degrees of freedom due to the release of the colour degrees of freedom of the partons. The exact temperature of the transition and the order of the phase transition are still open questions, under intense study. However current results

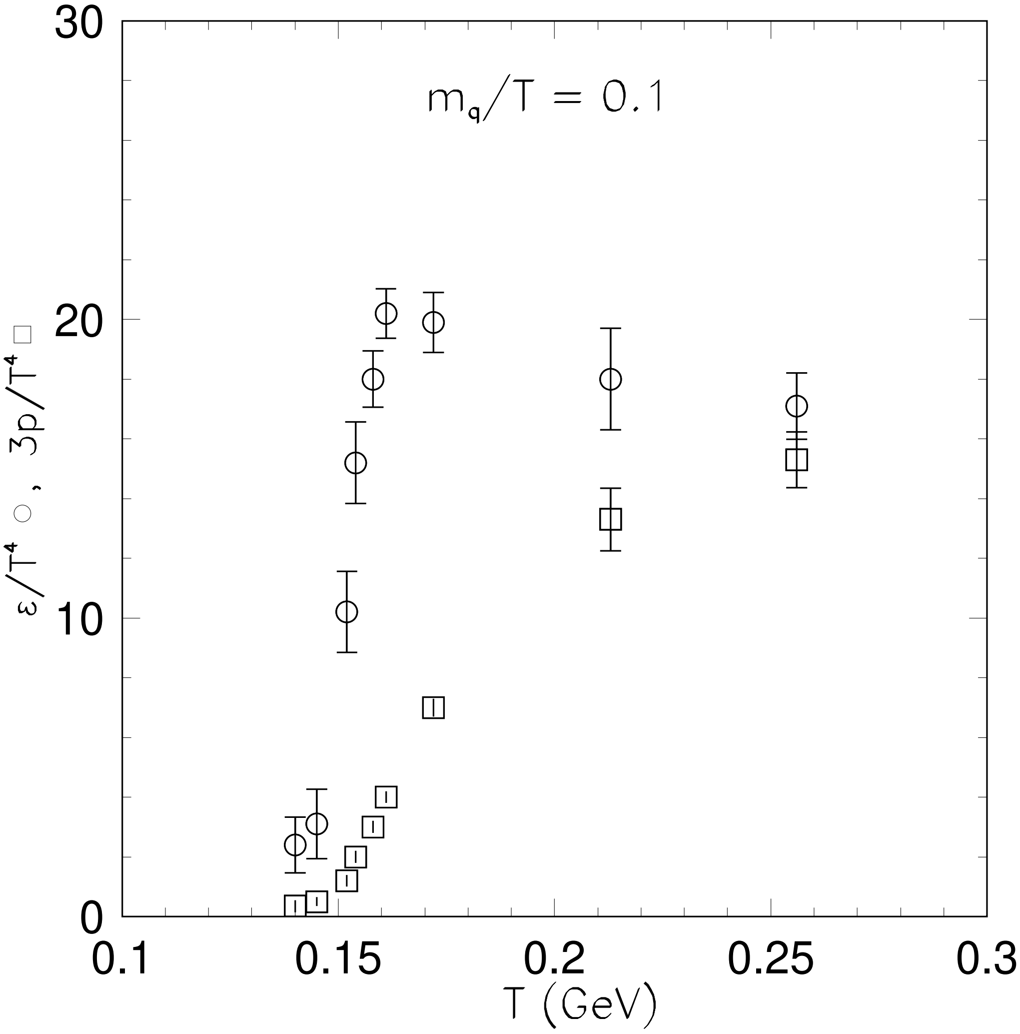

Figure 1.2: A recent result of lattice QCD calculations of energy density and pressure for two light quark flavors. The predicted phase transition is clearly visible between temperatures of 150-200 MeV.

give us a strong clue as to where we expect the transition to occur.

1.5 Heavy Ion Collision Conditions

Relativistic heavy ion collisions offer the one realistic laboratory to create conditions which makes the study of the QGP possible. Since this realization was made an extensive effort has been made to accelerate and collide ions of higher and higher mass and center of mass energies. The origins of the experimental heavy ion program can be traced back to the acceleration of the first ions in 1974 at the Berkeley Bevalac. A summary of the status and planning of heavy ion experiments is given in Table 1.2. The progression of these experiments is clearly towards beams of the highest possible center of mass energy, as well as towards the heaviest beam particle(highest A). What is to be gained by moving to higher energies and higher A values? Recall that in order to create a QGP, certain conditions of energy density and temperature must be reached. In other words, the nuclear matter must be heated and/or compressed to certain critical values. Higher center of mass energies allow for this heating and compression to take place. Higher energies mean that the colliding nuclear volumes will experience higher temperatures as the quark matter in the reaction volume collides and thermalizes. Higher energy densities will also be achieved at higher energies due to the additional Lorentz contraction of the overlapping nuclei.

Table 1.2: Status and planning of heavy ion experimentation. BNL(Brookhaven National Laboratory) is in Upton, New York. CERN(European Center for Nuclear Research) is located in Geneva, Switzerland. The AGS(Alternating Gradient Synchrotron) and RHIC(Relativistic Heavy Ion Collider) are both accelerators at BNL. The SPS(Super Proton Synchrotron) and LHC(Large Hadron Collider) are both accelerators at CERN.

Time:	Machine	Beams	CM Energy[GeV/n]
1986-1993	BNL-AGS	up to ^{28}Si	5
	CERN-SPS	up to ^{32}S	20
1993-1998	AGS+Booster	up to ^{197}Au	4(Pb)
	SPS+Pb Injector	up to ^{208}Pb	17(Pb)
1999(?)-	RHIC	up to ^{197}Au	200(Pb)
2004(?)-	LHC	up to ^{208}Pb	6300(Pb)

Experiments have been moving to the highest possible A values(usually Au or Pb) for different reasons. In order to talk about the thermodynamic ideas of a system of hot quark matter interacting at some temperature we need to have a system in equilibrium. The system has to exist long enough so that a phase of matter can be defined and described. Equilibrium can only be reached and maintained in a large interactive system where the number of collisions per particle is greater than one and thermalization can take place. Only under these conditions do the ideas of a phase transition or temperature make sense. For collisions of individual nucleons no such thermodynamic system exists. For collisions of medium size nuclei, say ^{32}S at the SPS, the limited number of nucleons and the fact that ^{32}S is mostly a surface nucleus makes the system far from optimal. The ^{208}Pb nuclei used at NA49 with a factor of $\sim$7 larger volume make this nucleus a much more viable system for achieving and maintaining a large thermalized system over a longer time scale.

Recall that theoretical predictions have established a range of values for the critical parameters that are necessary for QGP production. Lattice QCD calculations have placed the value of the critical temperature near $T_c \simeq$ 150-200 Mev, corresponding to a critical energy density necessary for deconfinement of $\epsilon_c \simeq$ 1-3 GeV/fm^3. It is important to know whether or not we are at or approaching these critical values at NA49, where we are using Pb beams at $\sqrt{s} \sim$ 17 GeV/A. An estimation of the energy density achieved at NA49 has been made via a measurement of the transverse energy production[Albe95]. We find that the energy density in head-on Pb + Pb collisions at this energy reaches about 3 Gev/fm^3, thus surpassing the critical density predicted by lattice QCD. Assuming equilibrium has been achieved, transverse energy production can be related to energy density in a Bjorken-type scenario[Bjor83], which is a theoretical benchmark used frequently in the field. This formalism builds on the work of Landau[Land53], whose model was built around the classical equations of relativistic hydrodynamics assuming as a constraint the equation of state of a relativistic gas, $p = 1/3\epsilon$, where p is the pressure and ϵ is the energy density. Bjorken adopted this formalism with the additional constraint that at sufficiently high energy a central plateau region develops in the rapidity distribution of the produced particles. In this Bjorken scenario the energy density of the primordial interaction volume is given by

$$\epsilon = (dE_T/d\eta)/\pi R^2\tau,$$

where R is the transverse radius of the participant volume(equal to the radius, $R = 1.12A^{1/3}$ fm, of Pb), and τ is the hadronic formation time, which is assumed to be $\tau = 1fm$, as is commonly employed. The transverse energy density in psuedorapidity at midrapidity is found to be $dE_T/d\eta = 405GeV$ at NA49, corresponding to a central trigger which represents 2% of the inelastic cross section. These values give an energy density of $\epsilon \simeq 2.9\ GeV/fm^3$. This estimate is encouraging, in that it indicates that the energy density achievable at NA49 is at the high end of the currently expected theoretical predictions of where a QGP should occur.

1.6 Heavy Ion Collision Dynamics

The collision of two relativistic heavy ions can be visualized within the context of a simple spectator-participant model. This scenario is shown in Fig. 1.3. Within this model two Lorentz contracted nuclei approach each other, then overlap and undergo an interaction. The region of the interaction is limited to those nucleons in both the projectile and target which lie within the region of geometrical overlap, which are defined to be the participant nucleons. All other nucleons are defined to be spectators; spectators will proceed along with a small perturbation of their initial motion but will essentially not take part in the interaction. The participant region becomes a hot, dense region of strongly interacting quark matter. The centrality of a collision is characterized by its impact parameter, b. The impact parameter is defined to be the distance between the centers of the two colliding spheres. A sketch of two overlapping nuclei with a defined impact parameter is seen in Fig. 1.4. For very peripheral collisions, the impact parameter is equal to the sum of the two colliding nuclei, 2R in this case. This is the case of two spherical nuclei just touching. For impact parameters larger than 2R there is no overlap of the two nuclei and no strong interaction takes place. The impact parameter can vary from 2R in very peripheral collision to close to zero for the most central,

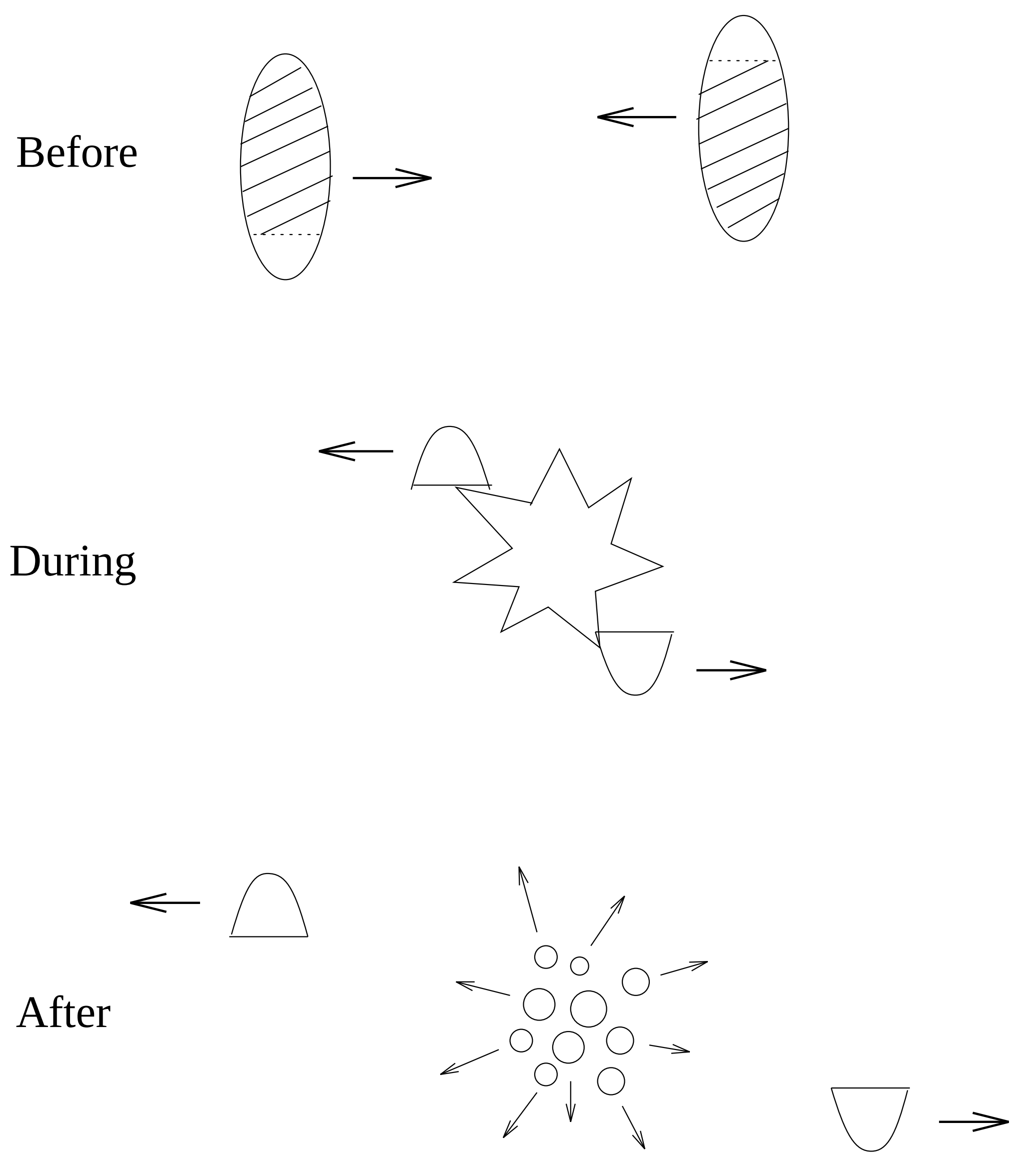

Figure 1.3: A simple picture of a nucleus-nucleus collision. Before the collision, the Lorentz-contracted nuclei approach each other. The shaded parts of nuclei contain the nucleons that will interact (participants) and the unshaded parts those that will not interact (spectators). During the collision, participants form a hot and dense region while spectators keep moving in the original directions.

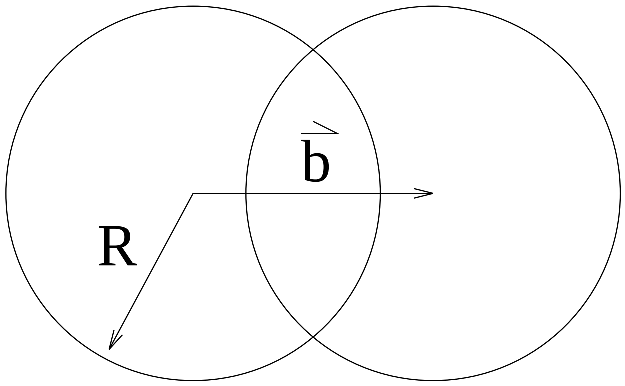

Figure 1.4: The overlap of two nuclei

violent collisions with complete geometrical overlap.

1.7 Nuclear Stopping

The amount of heating and compression which takes place in the two colliding nuclei of a central collision depends on a quantity known as nuclear stopping. The amount of nuclear stopping is a measure of how much of the initial energy is lost by the baryons in the colliding nuclei, or equivalently how efficient the two nuclei are at slowing down or 'stopping' each other. The energy which is initially tied up in the longitudinal beam energy of the baryons is redistributed into transverse degrees of freedom in the form of particle production and kinetic energy. The degree of stopping is inferred from the p_T-rapidity distributions of the final state baryons[Harr96]. Two extreme scenarios can be imagined, and are illustrated in

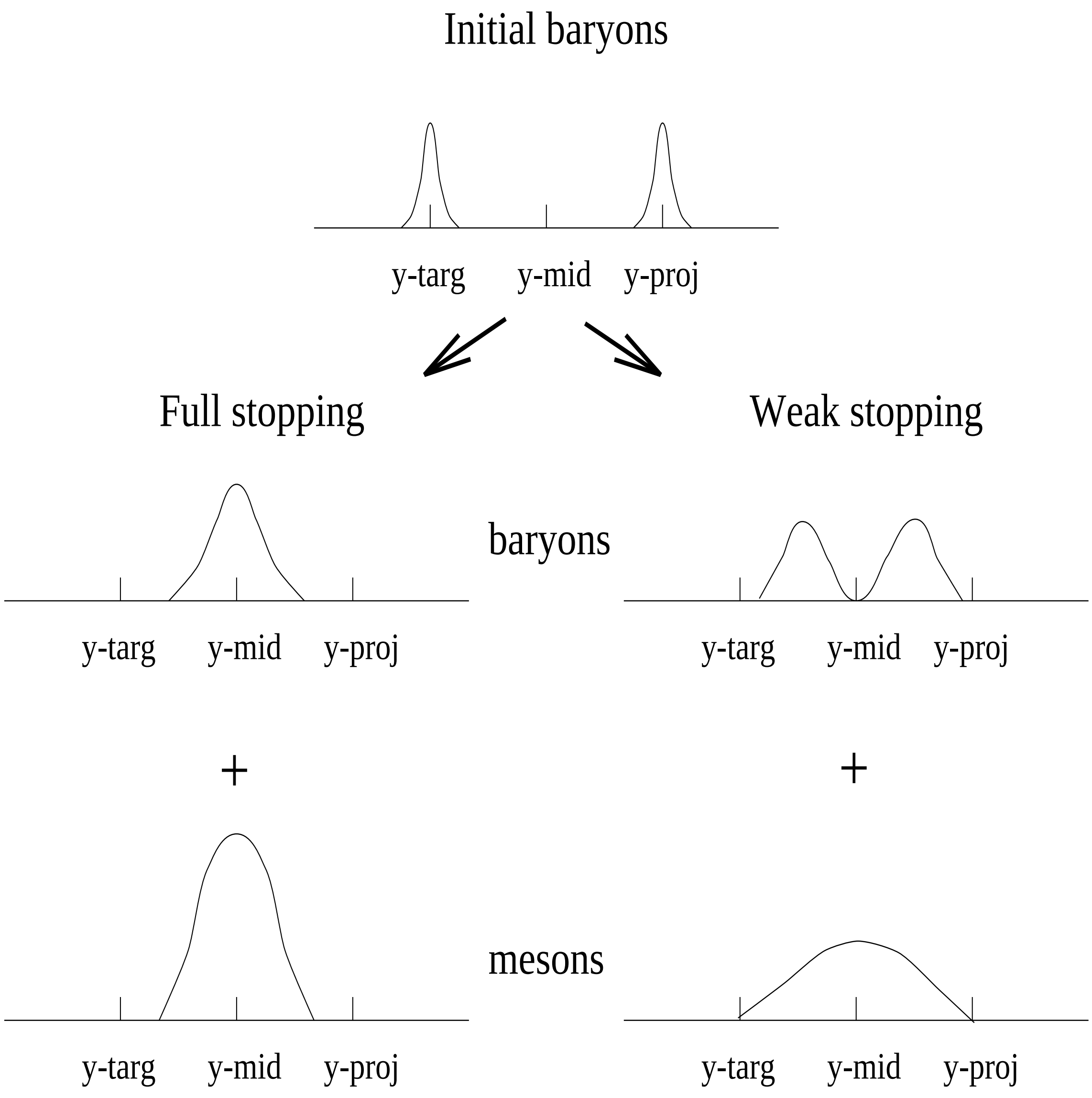

Figure 1.5: Two extreme scenarios of a heavy-ion collision. Left: full stopping scenario in which the initial baryons are completely stopped at the central region in the center-of-mass rapidity, creating a concentrated distribution of mesons in the same region. Right: weak stopping scenario in which the baryons do not completely stop one another and leave behind a wide distribution of mesons.

Fig. 1.5. Initially the rapidity distribution of the baryons are localized at the rapidities of the beam and target. One extreme scenario, depicted on the left hand side of the diagram is that of full stopping. In this scenario the initial baryons lose a majority of their initial kinetic energy, where the resulting final rapidity distribution is baryon rich at mid-rapidity. Alternatively, we can imagine a weak stopping or 'transparent' scenario, depicted on the right. Here the initial baryons are stopped very little and are not moved far from their initial rapidity distributions. The amount of relative stopping is usually defined to be

$$S_R = E_T^{4\pi,B0}/E_T^{max},$$

where $E_T^{4\pi,B0}$ is the transverse energy in the full 4π acceptance and at most central collisions, and E_T^{max} is the maximum possible transverse energy deposition. E_T^{max} is defined as follows: (1) isotropically distribute the total center-of-mass energy, minus the participant baryon rest mass; (2) define E_T^{max} to be the transverse fraction of that energy, $E_T^{max} = (\pi/4)[\sqrt{s_{tot}} - m_{part}]$. At the lower AGS energies the stopping approaches 100% in central Au + Au collisions[Barr93]. At NA49 the relative stopping was found to be (57 $\pm$ 6%) for Pb + Pb central collisions[Albe95], corresponding to an average rapidty shift of $\Delta y \sim 1.6$ units of rapidity . This is still a large amount of stopping and not indicative of significant 'nuclear transparency'.

1.8 Space-Time Evolution of Heavy Ion Collisions

A pictorial view of the space-time evolution of a heavy ion collision is shown in Fig. 1.6. The left-hand side of the diagram shows the probable space-time scenario for a collision in which only a hadron gas is formed, while the right-hand side addresses the various phases and parameters associated with the formation of a QGP. The vertical axis depicts the time-evolution of the system, while the horizontal(z) axis represents the spacial extent in the beam direction. Immediately after the collision the two nuclei are in a pre-equilibrium state. This corresponds to a formation time of about 1 fm/c, after which the strongly interacting quark and gluonic matter approaches thermal equilibrium through partonic scattering. If the temperature and energy density are high enough, and exceed the critical parameters(T_C and ϵ_c), one assumes the QGP is formed. The partons are now thermalized and in a freely propagating plasma of quarks and gluons. The system will keep expanding and cooling, dropping below the QGP critical transition parameters after $\sim$ 5 fm/c. At this point the strong matter likely spends a relatively long period($\sim$ 10 fm/c) in a mixed phase, intermediate between QGP and a hadron gas. During this mixed phase the matter is having to reorder itself from the many partonic degrees of freedom that were released in the QGP phase to the more ordered hadronic states in the hadron gas. Following a mixed phase the

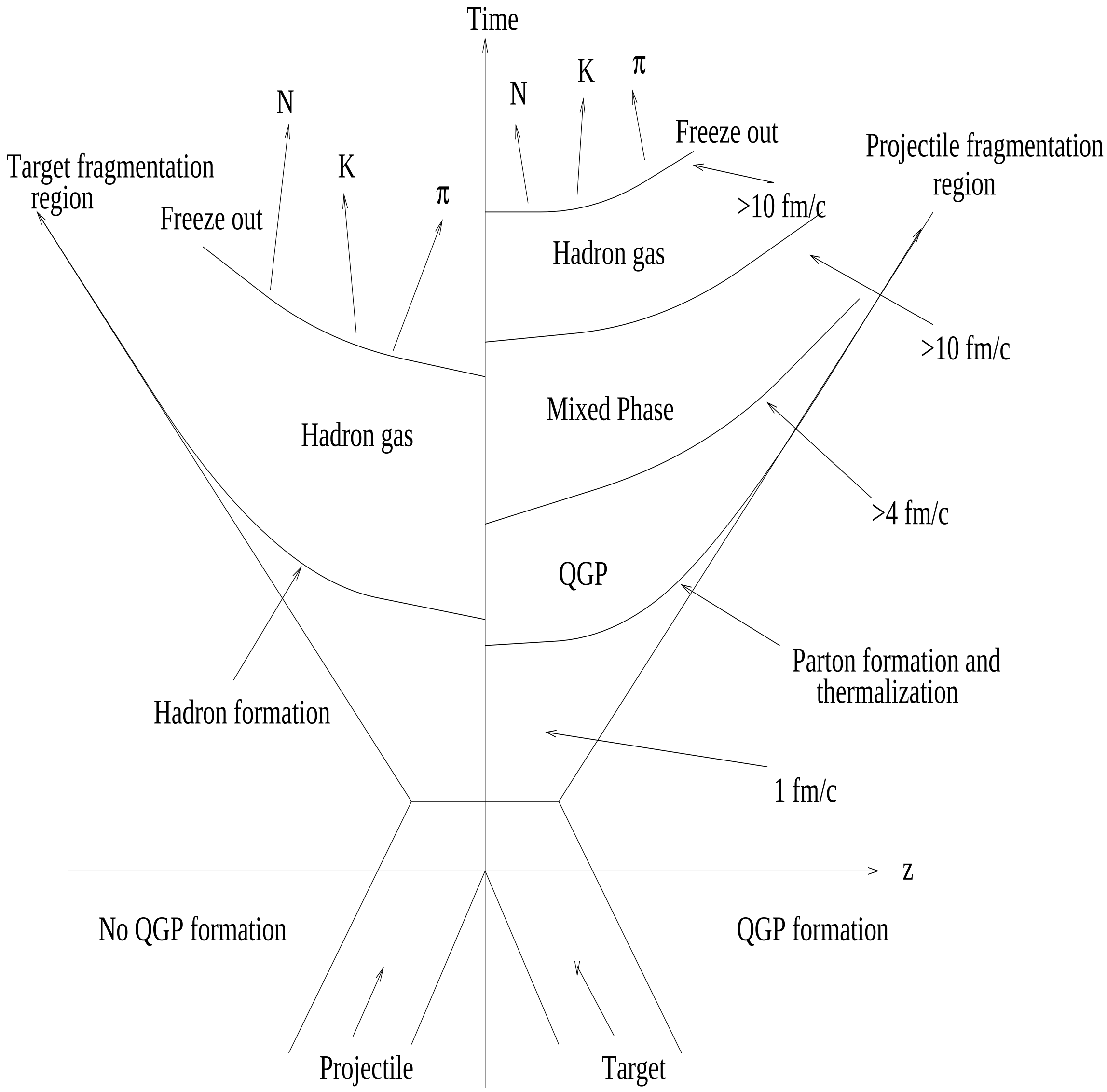

Figure 1.6: The space-time evolution of an ultra-relativistic heavy ion collision. The left hand side of the plot demonstrates the fireball evolution assuming no QGP formation and the right hand side assumes GQP formation.

hadrons continue to interact in a hadron gas until the system reaches freezeout, at which point no further interactions occur. The hadrons that exist at freezeout are the final state particles which are measured and quantified in our detectors.

1.9 Experimental Signatures of QGP Formation

Since the formation of a QGP was hypothesized a large number of possible 'signatures' of the QGP have been predicted. Since no QGP has ever been observed and measured, all such signatures are speculatory. Nonetheless if we reach and exceed conditions under which we think a QGP should be formed, and none of the multiple possible signatures have been observed, we still learn something. Either the conditions created in heavy ion collisions are not yet sufficient to make a plasma, or the formation of this state in such an experiment is impossible.

Some of the proposed signatures of the QGP involve novel phenomenon which are beyond the normal predictions of the Standard Model. But a majority of the predicted signatures of the QGP simply involve anomalies in the yields of certain species of produced particles in normal hadronic physics. This fact makes an accurate assessment of any proposed experimental signature especially difficult for two reasons. The first reason is that your QGP signal must be adequately differentiable from the signal that would be produced by a hot hadronic gas. Many of the most popular proposed QGP signatures, such as strangeness enhancement[Hein88] and

J/Ψ[Satz90] suppression, produces signals which have been found to be close or identical to the hot hadronic gas signal of the same phenomenon. This can make the detection and confirmation of a QGP ambiguous.

The second reason that hadronic signals make an accurate assessment of QGP formation difficult is due to the complex space-time evolution of the QGP previously discussed in Section 1.8. The QGP is expected to form and start hadronizing in the first few fm/c after the collision; the plasma then goes through a very complicated mixed phase followed by the hadronic gas phase. Any hadronic signal runs the risk of losing its memory of the QGP phase after it has proceeded through the hadronic gas phase. For instance if additional strangeness content was produced via the QGP, this additional strangeness production would have to be unfolded from the known strangeness enhancement which can be produced through multiple scattering in a hot hadronic gas.

1.9.1 Electromagnetic Signals

The fact that any hadronic signal of the QGP will be clouded by the evolution of the system has led the heavy ion community to predict and try to measure signals which are produced at the earliest possible stages, but are not affected by the subsequent hadronization. Possible signals of this type are thermal dileptons or direct photons[Gyul84], which are emitted by the plasma and then escape unhindered by hadronic mechanisms. One may also study the effect of the produced medium on the observed production rates of heavy quark bound states such as the J/Ψ and various other charmonium $c/\overline{c}$ bound states[Mats86]. These types of signals require finely segmented electromagnetic calorimetry with excellent energy resolution, as well as muon detection capabilities. NA49 has no such capacity and concentrates on hadronic rather than electromagnetic signals.

1.9.2 Hadronic Signals

Since hadronic signals are prone to suffer from the previously mentioned limitations, the ultimate detection of a QGP is not likely to be claimed from any signal event observable or predicted signature; no smoking gun has thus far been conclusively predicted or observed for plasma formation. The likely scenario for the confirmation of QGP formation will be to have the simultaneous observation of several signatures. As the critical conditions are reached for plasma formation, multiple observables should undergo critical phenomena dictated by the phase transition. The NA49 experiment was, from its inception, intended to be capable of measuring several of the most accepted experimental signatures of QGP formation. Such observables at NA49 include the following:

- entropy produced in the reaction, as measured by the rapidity density and transverse momentum inverse slope(effective temperature) of π^+, π^-

- the pion source radii in transverse and longitudinal directions as measured by HBT $2\pi^-$, $2\pi^+$ Bose-Einstein correlations
- strangeness enhancement, extracted from the measurement of K^+, K^-, K_s^0, Λ, $\overline{\Lambda}$, and ϕ production
- the K/π ratio at mid-rapidity
- rapidity distribution of the net baryon number, or stopping spectrum

Although NA49 will have the ability to measure all of these listed observables, this thesis addresses the measurement of the first observable, the entropy produced in the collision via the pion production. Thus special attention will be devoted to this predicted QGP signature.

1.10 Entropy Production

A discussion of the produced and measured entropy in a heavy ion collision is one of the most fundamental ways to distinguish between the hadron gas(HG) and QGP formation scenarios. At fixed temperature T, the QGP is the phase with the higher entropy. This difference occurs because of the liberation of the color degrees of freedom of the partons in the deconfined QGP phase. Although it is not a closed theoretical question, the universal assumption in the literature is that the total entropy created in the production of a QGP or hadron gas remains constant during the expansion phase[Lee88, Lete92, Lete94]. Thus we have a series of disorder increasing independent reactions, defining an irreversible quantum process. As will be discussed, the manifestation of this entropy production is in the form of particle production at the point of re-hadronization, a majority of which is the production of pions. Thus the entropy released in the collision is to first order proportional to the pion production.

1.10.1 Fermi/Landau Approach

The expectation that the effective degrees of freedom in deconfined matter is significantly higher than in hadronic matter has motivated the study of pion(entropy) production in nuclear collisions as a function of the masses of the nuclei and the interaction energy[Gazd95a,Gazd95b]. The description of pion production in high energy collisions using a statistical approach was first introduced by Fermi[Ferm50] and later modified by Pomeranchuk[Pome51] and Landau[Land53].

Landau began by considering a central collision of two identical nuclei in the center of mass system. In the early stages of the collision the strongly interacting matter is assumed to thermalize and a majority of the entropy is produced. A further assumption is that during the following expansion stage the final state entropy is proportional to the early stage entropy, a standard assumption in the literature[Lete94]. The volume of the interaction region in the early stage, V, is proportional to the Lorentz contracted volume of the nuclei, V_0, according to

$$V \sim \frac{V_0}{\gamma} = \frac{2 \cdot m_N \cdot V_0}{\sqrt{s}_{NN}}, \tag{1}$$

where $\sqrt{s}_{NN}$ is the center of mass energy per nucleon pair and m_N is the nucleon mass. The collision energy density, ϵ, available for particle production is then taken to be

$$\epsilon = \frac{E}{V} \sim \frac{(\sqrt{s}_{NN} - 2 \cdot m_N) \cdot \sqrt{s}_{NN}}{2 \cdot m_N \cdot V_0}. \tag{2}$$

As previously mentioned, the initial energy density creates a certain entropy in the early stage which is available for particle production. This particle production is seen mainly as pions, which typically account for around 90% of the produced particles. The entropy per pion is also weakly dependent on the freeze-out temperature; in the freeze-out temperature range from 100-200 MeV the entropy per pion($\simeq 4.2$) changes by less than 10%[Gazd95b]. Thus to first order the mean pion multiplicity should be proportional to the entropy:

$$\langle \pi \rangle \sim S.$$

Now we need to relate this entropy to the energy density given by (1). The entropy at the early stages can be expressed as:

$$S_E = V \cdot \sigma, \tag{3}$$

where σ is the entropy density. The entropy density can be related to the energy density by assuming some equation of state for the matter. As a best approximation the equation of state(EOS) was assumed to be that for a massless gas of relativistic pions, for which the EOS is[Land53]

$$p = \frac{1}{3} \cdot \epsilon, \tag{4}$$

where p is the pressure and ϵ is the energy density. For the blackbody case here where $\epsilon \sim T^4$ the entropy density is given by

$$\sigma \sim \epsilon^{3/4}. \tag{5}$$

This relation, together with (2) and (3) give us the early stage entropy as

$$S_E \sim V \cdot [(\sqrt{s}_{NN} - 2 \cdot m_N) \cdot \sqrt{s}_{NN}]^{3/4}. \tag{5}$$

Due to the diffuse edge of the nuclear surface, not all nucleons take place in even the most central collisions. This leads to a modification of the volume of the system, in that the effective volume of the colliding nuclei must be scaled by the actual number of participants in the collision, $\langle N_P \rangle$. Taking this into account and using the lorentz-contracted volume found in (1) we arrive at

$$\langle \pi \rangle \sim S_E \sim \langle N_P \rangle \cdot \frac{(\sqrt{s}_{NN} - 2 \cdot m_N)^{3/4}}{(\sqrt{s}_{NN})^{1/4}}. \tag{6}$$

This is the same dependence on pion multiplicity found by Fermi in his original work, when he was trying to predict the energy dependence of pion production. He thus defined the famous Fermi energy variable, F, as

$$F \equiv \frac{(\sqrt{s}_{NN} - 2 \cdot m_N)^{3/4}}{(\sqrt{s}_{NN})^{1/4}}.$$

In the recent Gazdicki analyses, this F variable has been modified to assure that at the threshold energy the pion multiplicity is equal to zero by subtracting the pion mass as follows:

$$F = \frac{(\sqrt{s}_{NN} - 2 \cdot m_N - m_\pi)^{3/4}}{(\sqrt{s}_{NN})^{1/4}}.$$

We now have a functional form which predicts the multiplicities of pion production as a function of energy, as

$$\langle \pi \rangle \sim \langle N_P \rangle \cdot F.$$

The number of participants, $\langle N_P \rangle$, depends on the centrality, i.e. what fraction of the total reaction cross-section(σ_R) is used in triggering the events used in the analysis. For central collisions, typical values used are 2-5% of σ_R. For 5%, $\langle N_P \rangle \simeq$ 0.87 (A + A) in AA collisions.

Besides that in the pions, entropy is also contained in the other particles produced (mainly kaons) and is also transferred to participant nucleons in the form of increased energy. Thus the total entropy , in units of entropy per pion, can be estimated as[Gazd95b]

$$S = 3 \cdot (\langle h^- \rangle - \langle K^- \rangle) + \kappa \cdot \langle K/\overline{K} \rangle + \delta \cdot \langle N_P \rangle.$$

The first term estimates the entropy due to the pions, as the mean number of negative pions is well approximated by the difference of negative hadrons and the negative kaons.(few $\overline{p}$'s or other exotic negative hadrons are produced) The factor of 3 is for the three kinds of pions, whose production rates are nearly equal. The second term describes the entropy carried by the all the kaon species, $K^{\pm}, K^0, \overline{K}^0$. The factor κ is given by the ratio of the entropy per kaon to the entropy per pion, where $\kappa \approx 1.45$ at a temperature of 150 MeV. The third factor accounts for the entropy that is transferred back to the baryons during the expansion of the system, where $\delta \approx .35$[Gazd95b], determined from the shift of the intercept(away from zero) in the the pion multiplicity vs F linear relationship.

This approach of accounting for the entropy produced by particle production provides a conceptual framework for predicting the amount of pion production one would expect as a function of center of mass energy. Using this as a benchmark, one can then look for critical type transition behavior around the energies where QGP formation is expected to occur.

Chapter 2

Experimental Setup

2.1 The CERN Heavy Ion Accelerator Complex

The heavy ion program at the CERN Super Proton Synchrotron(SPS) began in 1986 with the commissioning of an oxygen ion source. Beams up to 200A GeV/c and as heavy as Sulfur were delivered up to 1994. In autumn of 1994 the first Pb beams at 158A GeV/c were made available for the heavy ion community to study.

The heavy ion acceleration procedure at CERN proceeds through multiple acceleration stages before reaching its final beam energy of 158A GeV/c. The heavy ion linear accelerator injector(LINAC3) provides a partially stripped current of $^{53+}$Pb to the proton synchroton booster(PSB). In the PSB the $^{53+}$Pb ions are accelerated to 95.4A MeV/c and then passed into the proton synchroton(PS). The PS accelerates the ions to 4.25A GeV/c before injection into the super proton synchroton(SPS). On the way to the SPS the ions are passed through an Al stipper foil which finishes ionizing the ions to $^{82+}$Pb. The SPS finishes accelerating the Pb ions to 158A GeV/c, at which point the beam is divided and sent to the North and West experimental halls. The NA49 experiment is located in the North experimental area on the H2 beam line in Prevessin, France.

2.2 NA49 Experimental Configuration

The NA49 experiment was designed specifically to study central collisions of lead nuclei at the SPS. The complexity of these events is unprecedented in accelerator-based nuclear and high energy experiments: each central collision produces up to 2000 charged particles. NA49 is a large-acceptance spectrometer with good momentum resolution and particle identification, designed to measure about 60% of the produced charged particles. Because of these very high multiplicities, NA49 has the unique opportunity to do statistically significant event-by-event analysis of many of the possible signals of the QGP phase transition.

The natural choice for three-dimensional imaging of very complex events is the Time Projection Chamber(TPC). As is shown in Fig. 2.1 the NA49 experiment contains four TPC's: two vertex TPC's situated in large dipole superconducting magnets and two Main TPC's downstream of the magnets on either side of the beamline. These tracking chambers are the workhorse detectors of NA49, as they

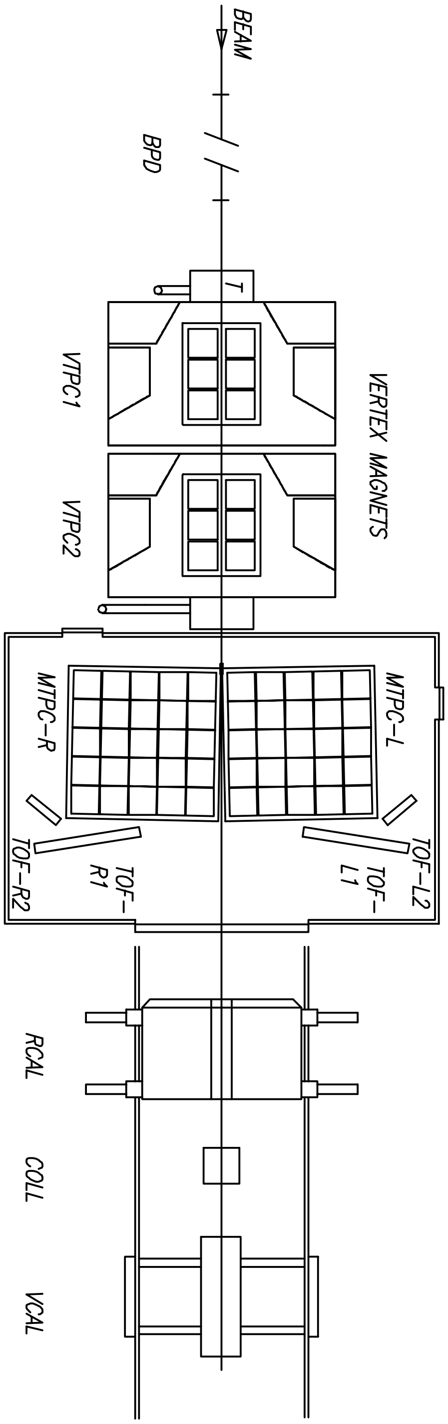

Figure 2.1: The experimental layout of NA49

determine the trajectories and momentum of the charged particles and are the primary source of particle identification(PID). PID is possible in the MTPC's by measuring the specific energy loss, dE/dx, of charged particles in the relativistic rise regime. In the momentum range $3 \leq p \leq 7$ GeV/c particle identification is enhanced by four highly segmented time-of-flight(TOF) wall arrays which are situated just behind the MTPC's. Further downstream of the TPC's and the TOF walls are two calorimeters, a ring calorimeter and a veto calorimeter. The ring calorimeter measures the transverse energy flow in the reactions and has a central hole to allow spectator nucleons to continue on to the forward(Veto) calorimeter. The Veto calorimeter was used to measure the forward energy distribution, and to provide triggering.

For the 1994 run only a subset of the detectors were operational; these include VPTC2 and MTPCR, as well as TOFR and the calorimeters. In 1995 VPTC1 and MTPCL were added, as well as TOFL and the grid-TOF detectors.

2.3 Beam, Trigger and Target

As previously mentioned, NA49 is located in the North experimental area on the H2 beam line. A schematic of the detectors used for triggering in standard TPC runs is shown in Fig. 2.3. Since these detectors are numerous and easy to replace the exact layout and naming scheme can vary from run to run. The beam direction and incident angle are determined by two proportional counters, BPD1 and BPD2, located upstream of the target and separated by $\sim$ 23 m. These Si strip detectors each contain 192 horizontal and vertical strips from which a 200 μm beam position and $\sim$ 10 μr angular resolution is obtained.

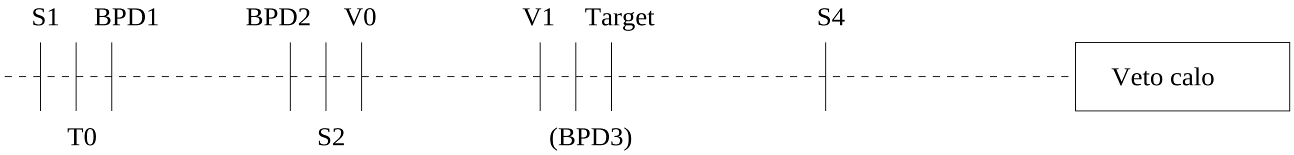

Figure 2.2: A schematic of the NA49 triggering detectors.

The beam Trigger is derived from the signals of the following detectors:

- two beam counters, S1 and S2
- the V0 'veto counter' upstream of the target
- an interaction counter S4 downstream of the target
- from spectator energy measured by the veto calorimeter at the end of the apparatus

A valid beam particle is defined by the coincidence S1 $*$ S2 $*$ $\overline{V0}$. S1 and S2 are Čerenkov beam counters composed of a thin quartz wafer, while V0 is a 10x10 cm^2 veto scintillation counter with a 1 cm diameter central hole. This type of 'hole' detector is used to determine the presence of a beam halo caused by downstream gas interactions, indicative of a contaminated beam which should be vetoed. Thus a signal from V0 prevents the trigger signal from being sent. T0 is a Čerenkov detector used to get a start time for the TOF signal. S4 is a 1-mm quartz Čerenkov counter situated behind the target. S4 measures the signal from the spectator fragments, thus a strong signal from S4 indicates that no interaction has occurred in the target and again the trigger signal is not sent.

The most significant part of the NA49 trigger comes from the veto calorimeter, which allows us to trigger on the centrality of the Pb+Pb event. An anti-correlation between the transverse energy and the forward energy has been demonstrated[Albe95]. This anti-correlation is understandable in terms of a simple spectator-participant model. Before the collision there is no transverse energy, all energy(accept for the nuclei's transverse fermi momentum) resides in the forward direction defined by the beam. As collisions become more and more central the number of participants in the collision goes up and the number of spectators goes down. As the number of participants increases the amount of energy produced transverse to the beam direction increases and the amount of forward energy decreases. The amount of forward energy deposited by the spectators is maximal for very peripheral collisions with large impact parameter. The trigger for a typical central event involves requiring $E_{veto} < 8TeV$, corresponding to approximately 4% of the Pb+Pb inelastic cross section and an impact parameter below 3 fm.

Thus the final trigger for a central collision is S1 $*$ S2 $*$ $\overline{V0} * \overline{S3} * \overline{Veto}$.

The target is a 224 mg/cm^2 lead foil of $\sim$ 1% interaction length. Such a thin target was driven by the needs of the HBT physics analysis. A thicker target would increase the probability for multiple scattering of the produced particles with other nuclei in the target, which would degrade the momentum resolution crucial for HBT analyses.

2.4 Magnets

Two superconducting dipole magnets with a maximum total bending power of 9 Tm at currents of 5000 amps are centered on the beam line. During standard running, Magnet 1 is operated at a field of 1.5 T and Magnet 2 is operated at 1.1 T for an effective bending power of 7.8 Tm. These fields allow momentum determination in VTPC's 1 and 2 and also serve as 'sweepers' to lower the track density of the produced charged particles, giving them a kick in the direction perpendicular to the beam and magnetic fields. The standard field configurations are called STD+ and STD-; the STD- configuration is field up, and the STD+ configuration has the inverse polarity. STD+ sends negatives into MTPC-R, STD- sends positives into MTPC-R.

2.5 Time Projection Chambers(TPC's)

The TPC has been the dominant tracking chamber in high-multiplicity environments for over a decade[Mada84]. Originally developed for the PEP at SLAC, they have sinced been used at Tristan, Delphi, Aleph, NA35, NA36, EOS, and many other experiments. They are also going to be the main detector at two future heavy ion experiments, STAR at RHIC at ALICE at the LHC.

TPC's are able to reconstruct the 3-dimensional trajectories of charged particles, identify the particle by measuring the specific ionization energy they deposit along their tracks(dE/dx), and measure the momentum of a particle through its curvature if tracked in a magnetic field. TPC's are ideal for high multiplicity, 4π tracking environments which require large acceptance.

The TPC consists of a large gas filled volume placed in an electric and (often) magnetic field. Charged particles passing through the detector's active volume leave a trail of ionization as they pass through. A uniform electric field causes this ionization to drift to a highly granular read-out plane where the the ionization is amplified and collected. The combination of the time it takes for the ionization to drift to the readout plane, together with the 2-dimensional location of where on the readout plane the ionization hits allows for 3-dimensional spacial reconstruction of the track.

NA49 uses 4 TPC's to perform charged particle tracking and identification[Broc97].

TPC:	VTPCs		MTPCs	
Length:	260 cm		384 cm	
Width:	200 cm		384 cm	
Height:	72 cm		129 cm	
Drift distance:	69 cm		115 cm	
Drift voltage:	13 kV		16.5 kV	
Gas mixture:	Ne/CO_2		$Ar/CH_4/CO_2$	
Gas composition:	91/9		91/4.5/4.5	
	VTPC1:	VTPC2:	HR:	SR:
Sectors per TPC:	6	6	5	20
Pad-rows per sector:	24	24	18	18
Pads per pad-row:	192	192	192	128
Number of pads/sector:	4,608	4,608	3,456	2,304
Pad width:	3.0 mm	3.0 mm	3.13 mm	4.95 mm
Pad length	16 mm/28 mm	28 mm	39 mm	39 mm
Gap sense-wire/pad-plane:	3 mm	2 mm	2 mm	3 mm
Number of pads per TPC:	27,648		63,360	
Total number of pads:	182,016			

Table 2.1: Main parameters of the NA49 TPC detectors. The MTPC detector has sectors with different pad size: high resolution (HR) and standard resolution (SR).

The design properties of these 4 TPC's are summarized in Table 2.1. The different TPC's are optimized to serve different tasks. The two VTPC's are placed symmetrically in the beamline inside the two vertex magnets. These 2 VTPC's track particles for momentum determination and do so in the highest particle density region of the experiment; therefore the pads of these TPC's have the highest granularity(smallest size). The VTPC's field cages are built in two sections, with a 20cm gap along their centers allowing the beam and spectators to avoid passing through the VTPC's active region. As the amount of ionization deposited goes as Z^2, the charge deposited by Pb(82+) passing through the chamber and ionizing the gas would be $\sim$ 6700 times the charge of singly charged particles. This huge charge would saturate our electronics and cause a loss of information, and possibly space charge effects. The 2 MTPC's are downstream of the magnets and are placed on either side of the beamline at a slight angle, allowing the beam to miss the MTPC's completely. These TPC's track particles for momentum determination and were optimized for dE/dx particle ionization. The total tracklength of 4m sampled 90 times with 4cm long pads gives a design dE/dx resolution of $\sim$ 4%.

All TPC's have been chosen to be rectangular boxes, with readout plane on top and the high voltage cathode plane, which generates the drift field, on the bottom of each TPC. All TPC's have pad readout only.

2.5.1 Readout Electronics

The readout electronics are located on top of each of the 4 TPC's. For each type of TPC, individual readout modules are mounted in a precision machined Al-frame. Six individual readout modules are mounted in each VTPC and 25 readout modules are mounted in each of the MTPC's. These readout modules contain the pad planes and wire planes necessary to gather and amplify the drifted ionization. The electronics used to record this information will be discussed in section 2.8.

The readout modules mounted in the various TPC's are not identical; each has been optimized for tracking in different kinematic regions of the detector. All of the readout modules in the VTPC's and the 5 readout modules in each MTPC nearest the beam are in high track density regions, and therefore have the highest granularity and smallest pad width. These 'high resolution(HR)' modules have pad widths of ∼3 mm. The other 20 modules of the MTPC are in less dense regions and have 'standard resolution(SR)' pad widths of ∼5 mm. In addition to varying pad width the pad angle was also varied to accomodate tracks crossing the TPC's at some angle in the xz(padrow/beam) plane to minimize the tanα effect.

Three different types of wire planes with different functions are located in each readout module above the pad plane. A schematic of these different wire planes and the pad plane are shown in Fig. 2.4, where up in the figure is down in the lab. These three wire planes are the sense/field wire grid, frisch-grid and gating-grid. Ionization electrons in each TPC drift away from the high voltage cathode and towards the wire planes in a uniform electric field. As the electrons drift toward the readout planes, they are accelerated by the strong electric field of the sense wires, held at a high positive voltage of $\sim$ 1000 V in the various TPC's. As they accelerate they gain enough energy between atomic collisions to ionize the gas further, causing a cascading process whereby an avalanche is formed around the sense wire. The slow moving positive ions created during the avalanche then induce an opposite charge on the pad plane above the sense wires. This induced charge, proportional to the original number of electrons, is read out as the pad charge. The amplification factor is $\sim 10^4$. The field wires between the sense wires function to help shape the electric field around the sense wires, causing all electrons to accelerate towards one of the alternating sense wires.

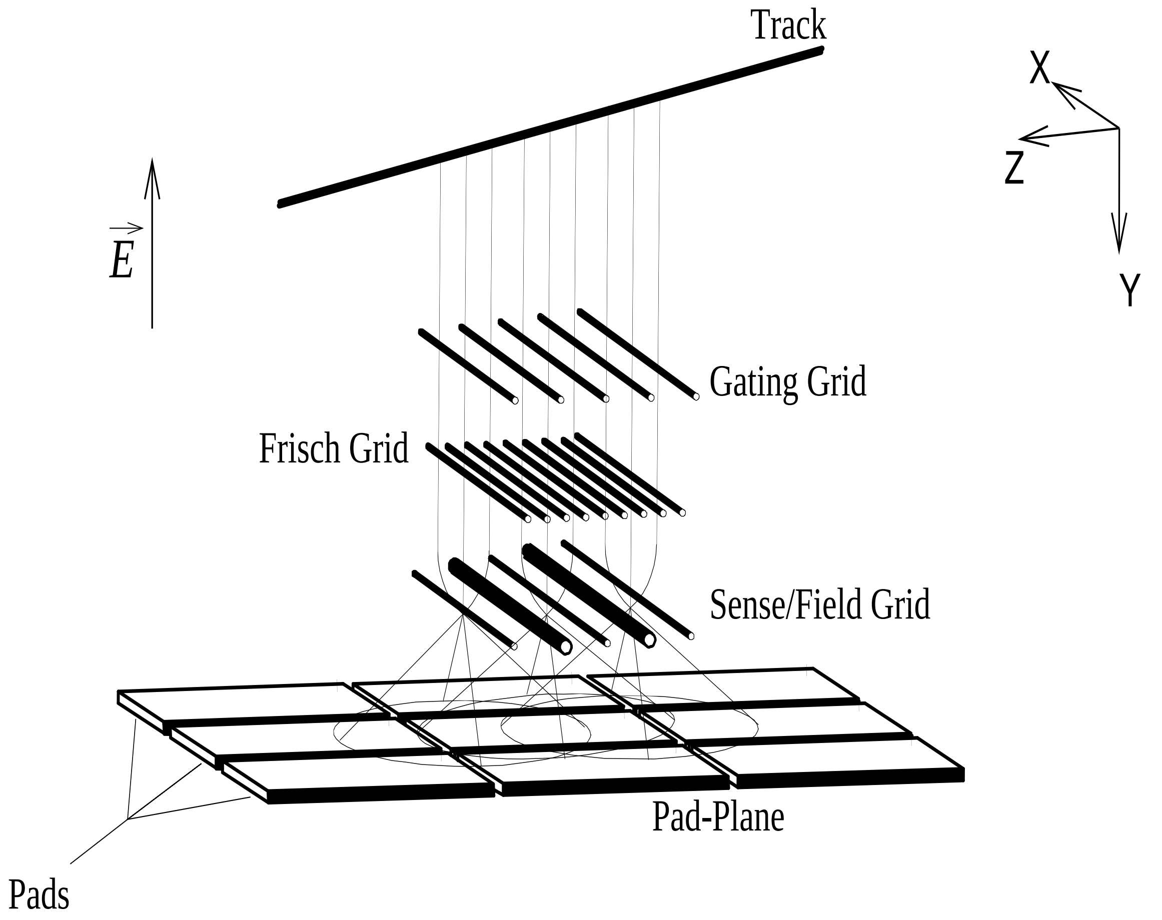

Figure 2.3: Shown is a schematic of the various wire planes and the padplane which is present in each of the NA49 TPC's. Up in the figure is down in the lab.

The next plane is the Frisch-grid, located 2.5 mm below the field/sense wire grid. This grid electrically shields the drift region from the collection region above. The fields caused by the sense wires and avalanches around the sense wires are large and constantly varying. These fields are isolated from the rest of the drift region by the Frisch grid, whose wires are all set to zero V. This grid is necessary to prevent later signals, yet to be collected and amplified, from feeling a distorted drift field and thus ambiguous drift speed and arrival time.

The last wire plane is the gating grid, located 6.5 mm below the Frisch grid. This grid is conditioned by the trigger to be either open or closed. A central trigger causes the gating grid to be opened, allowing ionization to pass through the grid. While open the gating grid wires are all set to the value of the electric field at the corresponding y(drift direction) value, and thus have no effect on the drifting electrons. The gating grid consists of alternating wires at ± 50 V when the gate is closed. The field lines thus connect between neighboring wires, and ionization electrons follow these wires and cannot pass.

2.5.2 Field Cage and Gas Box

The NA49 field cage/gas box construction were primarily driven by two main considerations:

- the need to keep the field cage as low mass as possible to minimize secondary scatterings from material in the field cage
- the need to keep the TPC active volume as gas tight as possible; any diffusion of electro-negative O_2 or H_2O will attach electrons and degrade the ionization signal arriving at the pad plane

The materials chosen for the field cages were driven by the first constraint; particles must enter through the material of the TPC walls but too much material would lead to an unacceptable amount of multiple scattering and secondary particle production. The field shaping electrodes of both TPC's were thus chosen to be 25μm Aluminized mylar strips. These strips were tension mounted around ceramic posts, which formed the support structure for the high voltage plane at the bottom of the TPC's. Ceramic was chosen for its excellent stiffness, to maintain the rigid tolerances demanded by the TPC's. Ceramic posts were located at the corners of the MTPC's and both sides of the VTPC's, and two additional supporting rods were located on each edge of the MTPC. These rods were fitted into the high voltage plane at the bottom of the chamber, the base of which was a 5 cm thick honeycomb structure. Precision aligned strips also shaped the field at the bottom of the chamber. The high voltage at this lower plane was graduated up the TPC by a resistor chain mounted on the ceramic support posts, maintaining a uniform drift field up to the Al readout chamber structure, kept at ground.

The gas box structure was constructed independently of the field cage and then mounted by lowering the readout chamber structure and field cage down on to the gas box. In order to minimize diffusion of electro-negative molecules, the gas box was constructed as a doubly-layered window structure. Both layers were constructed with a base of G-10 fiberglass and thin G-10 horizontal support arms. 125μm mylar windows were then mounted vertically around these support arms. The gas volume inside the gas box was kept at a slight overpressure to discourage diffusion of air into the active volume of the TPC. In addition, the narrow outer volume between the two layers of the gas box was filled with circulating nitrogen gas. The continuous circulation of the gas in this outer layer was intended to remove contaminants before they could reach the active inner volume.

2.5.3 Gas Choice

The gas choice was a crucial parameter in the design of the NA49 TPC's. The criteria for the choice of the gas was that the gas should provide a high two-track resolution capability and have a small Z to keep space charge effects and delta-electron production low. To satisfy the need for high two-track resolution a gas with low transverse and longitudinal diffusion constants and small drift velocities is needed. The final choices are listed in the previously shown Table 2.1(See Pg. 39). Gases were chosen with transverse and longitudinal diffusion coefficients of the order of 250 $\mu/\sqrt{cm}$. Ne has slightly better diffusion properties but is $\sim$ 7 times more expensive than Ar and so was only used in the VTPC's where two track resolution is most challenging due to higher track densities. The drifts speeds in both types of TPC's is $\sim$ 2 cm/μs.

2.6 Time of Flight(TOF)

The NA49 detector is outfitted with two different types of TOF detectors on both sides of the system to aid in particle identification(PID)(see Fig. 2.1) The first and larger TOF-R1 wall, operational during the '94 run, was designed to aid in mid-rapidity identification of Kaons from 4-7 GeV/c, where the K/p branches of the dE/dx curves are merged. The identical TOF-L1 was added for the '95 run. In addition, improved funding allowed for the construction of the Grid-TOF(TOF-L2, TOF-R2) for the '95 run, which aided PID in the momentum range $\sim$ 3-5 GeV/c. In these momentum ranges, a combination of TOF and dE/dx information from the MTPC is needed to determine PID.

TOF, Marburg(TOF-L1, TOF-R1)

These TOF walls consist of 891 individual scintillators on each side, read out by photomultiplier tubes. The TOF signal is given by the difference of the start time, given by the TO Cerenkov counter, and ending with the photomultiplier signal. The timing resolution was determined to be $\sim$ 75 ps.

Grid-TOF, Budapest(TOF-L2, TOF-R2)

Unlike the larger TOF walls which are composed of a large number of individual scintillators, the Grid-TOF is composed of horizontal and vertical sheets of scintillators. The two layers of scintillators are built from vertical and horizontal rods, and are perpendicular to each other, so that particles cross both scintillator planes. Altogether the detector uses 45 vertical and 48 horizontal rods, with 372 photomultipliers.

2.7 Calorimeters

NA49 uses two calorimeters, a Ring Calorimeter and a Veto Calorimeter(see Fig. 2.5)[Huan95]. These calorimeters have been used in the previous CERN experiments NA5, NA24 and NA35[Marz83]. In addition to providing on-line triggers for event selection, the calorimeters measure forward and transverse energies. Forward energy gives us a measure of the spectators of the event while transverse energy measures how violent or central the collision was.

Ring Calorimeter

The Ring Calorimeter is a hollow annulus with an inner radius of 28 cm and an outer radius of 149 cm. It has an electromagnetic part in the front followed by a hadronic part, each divided into 24 azimuthal sectors. The electromagnetic part is a Pb/Plexipop scintillator sandwich of 16 radiation lengths (X_0) and one interaction length (λ_{int}) thick. The hadronic portion is a Fe/Plexipop scintillator sandwich of 6 λ_{int}. Each of the 24 sectors are then subdivided into 10 cells, each with the same psuedo-rapidity coverage. Together this calorimeter contains 240 cells and readout channels for full azimuthal coverage, in the psuedorapidity range $2.1 < \eta < 3.4$.

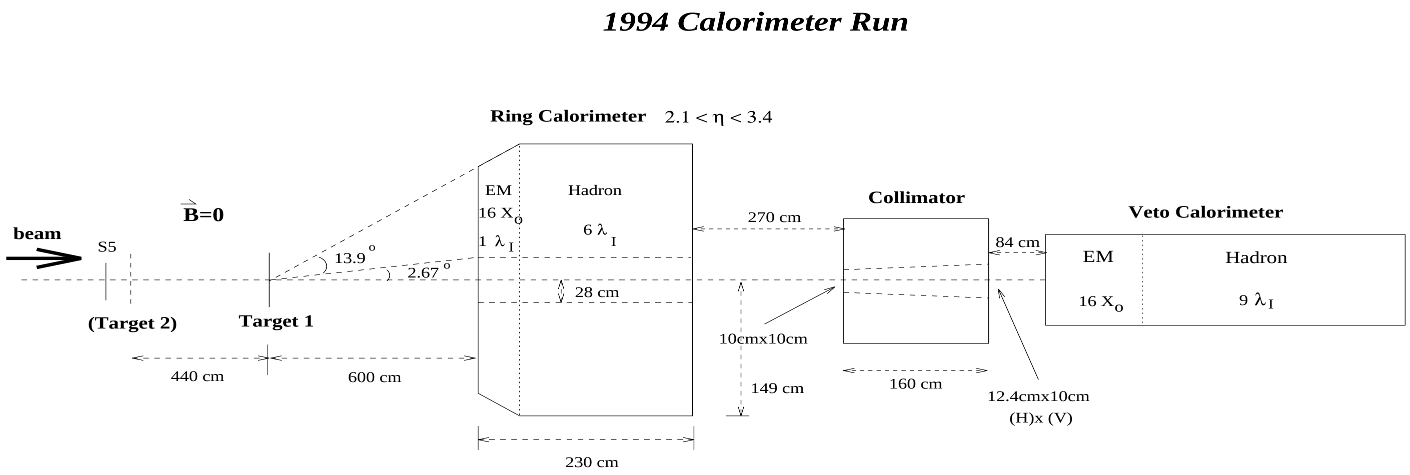

Figure 2.4: Top view of the 1994 Calorimeter run setup.

Veto Calorimeter

Downstream of the Ring calorimeter is an iron collimator defining the acceptance of the forward or Veto Calorimeter. This acceptance is $\sim 0.3^\circ$ around the beam in the lab frame, covering the projectile-spectator region of the collision. The Veto Calorimeter is also divided into electromagnetic and hadronic sections. The electromagnetic section is Pb/Plexipop scintillator of 17 X_0, the hadronic portion is Fe/Plexipop scintillator of 9 λ_{int}.

2.8 Data Acquistion(DAQ)

The data processing demands of heavy-ion detectors is growing at a rapid clip, as accelerators provide heavier elements at higher energies. Such violent nucleus-nucleus collisions produce extremely high multiplicities of charged particles, and tracking and recording the data from this huge amount of data in a timely matter is demanding. The information density at NA49 arises primarily from more than 180,000 electronic channels on our TPC's, each with 512 time samples. Thus a raw event from the NA49 TPC has a data volume of 93 MBytes. With our trigger rate of ≈ 10 events/sec this amounts to a raw data rate of ~ 1 GByte/sec. Since the occupancy rate of the TPC's averages only about 10%, the data is zero suppressed before it is written to tape, making the recorded size of one central lead-lead collisions about 8-10 Megabytes.

The NA49 DAQ[Bies96] was designed to take advantage of the SPS beam cycle, which is a $\sim$ 19s cycle. This 19s cycle corresponds to 5s of beam and a 14s dead time. The beam dead time means that the data can be recorded at a rate of about 4 times slower than the input rate. The DAQ logic is therefore organized in two phases, the buffering of the data during the 5s of beam and the compression and recording of the data in one continuous stream during the 19s cycle[Rauc94]. The TPC electronics chain was designed to handle the readout and buffering of the data; optical cables transfer this data to a VME system which processes the data and then moves it to the high-speed SONY tape drive.

A schematic of the highly integrated NA49 electronics chain is shown in Fig. 2.6. The demanding requirements of this chain, including a large number of channels, high packing density, and cost minimization, led to the choice of a custom electronics system. The design follows the readout structure developed for the EOS experiment[Rai90]. Signal amplification, shaping, storage, and digitization of 32 TPC pads are performed on one front-end(FE) card that is directly mounted on the TPC pad plane. This FE card contains two custom designed chips. One contains the preamplification and pulse shaping stages, and the other contains an analog storage device(SCA) and the analog to digital converter(ADC). The matching of the diffusion characteristics of the gases, reasonable drift velocities, and overall length of the drift volume led to a shaping time constant of 180 ns, a clock frequency on the SCA of 10 MHz, and 512 time samples per pad to cover the 50 μs

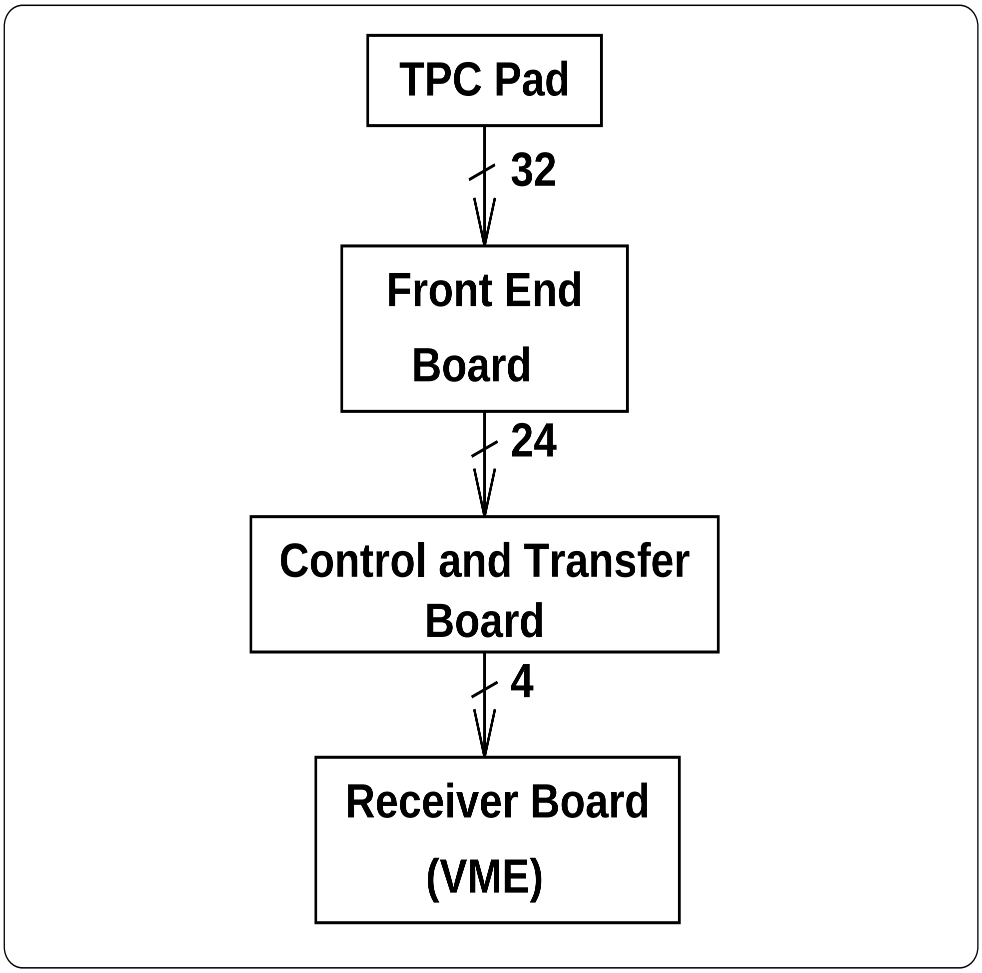

Figure 2.5: Schematic of the NA49 electronics chain.

drift time.

The digitized data of 24 FE cards are then collected by a control-and-transfer(CT) board through flat cables. The CT boards provide the signals necessary for controlling the custom IC's on the FE cards, including power and voltage monitoring. The data of all 768 channels are then multiplexed by the CT board into a fiber link, sending the data to a receiver board located in the NA49 counting house 20 meters away. Each VME receiver board collects data from four CT boards, equivalent to 3072 TPC pads. These receiver boards serve as data storage channels during the 5 second beam burst. The data on these boards is first passed through a Xilinx chip, where the data is pedestal subtracted for the different biases which resides on each SCA cell. A digital signal processor(DSP) is then used to perform zero suppression to reduce the data volume. The DSP code scans the input memory looking for pulses in time(drift) direction, a pulse being defined as two adjacent time slices above some threshold value.

The readout from the calorimeters is performed via LeCroy CAMAC ADCs and the TOF data is recorded via FASTBUS ADCs and TDCs. The output from the TPC's, TOF walls and calorimeters are then combined into one data stream and recorded on high output SONY tapes, each tape capable of storing 100 GBytes of data.

2.9 Laser Calibration System

A high precision laser system has been built for NA49[Renf96]. It allows the generation of a pattern of laser tracks covering a large part of the volume of each of the four TPC's. Special care was used to insure that such a calibration system would be of extremely low mass(minimizing the amount of scattering material in the particle's trajectories), and operational inside the magnet-field filled environment of the TPC's. Strict design goals were incorporated into the system, with a pointing accuracy of 100 μm desired.

2.9.1 Motivation

Such a laser calibration is desirable for a number of reasons. First, the laser system can be used to check the performance of the TPC's electronics and drift fields before a test beam or real beam is available, or while the beam is inoperative. The laser tracks are also used as a check on other determinations of the drift velocity within the TPC's. But the most crucial application of the laser system is in monitoring the quality of the fields in the TPC's. Laser tracks are used to serve as checks of the uniformity of the electric drift fields for both types of TPC's, and as a check of the magnetic field distortions in the VTPC's. The magnetic field of the vertex magnets varies strongly over the volume of the vertex TPC's. The resulting distortions of the track coordinates can be up to several centimeters. A correction table for these distortions is derived from a precise measurement of the magnetic field. The laser tracks are then used to check the distortion correction in different regions of the TPC volume and to verify the precision of the correction, but not to derive the correction itself.

2.9.2 General Layout

A schematic of the NA49 laser system is shown is Fig. 2.7. The laser itself is a frequency quadrupled NdYAG laser with 266 nm output, with 4mJ power output in a 8 ns pulse. Such a short wavelength laser is necessary to ionize the TPC gas, the short pulse being necessary to keep the laser tracks sufficiently localized in time(drift direction). The laser itself is mounted on a support system located on top of the vertex magnet in a climate-controlled hut. A series of several optical components are then used to control the position, intensity, polarization, and focusing of the beam before being split and transferred down from the laser hut to the various TPC's. The beam steering and control stage consists of 2 translation stages driven by stepper motors and one 3-dimensional rotating piezoelement. The translation stages are mounted on top of each other, allowing movements in perpendicular directions, with one step corresponding to 1 μm. The piezoelement is mounted on the last translation stage and consists of 3 independently controlled piezo stacks which allow angular variations in all directions up to 12 mrad. This steering system delivers the beam to the TPC where the final laser beam control

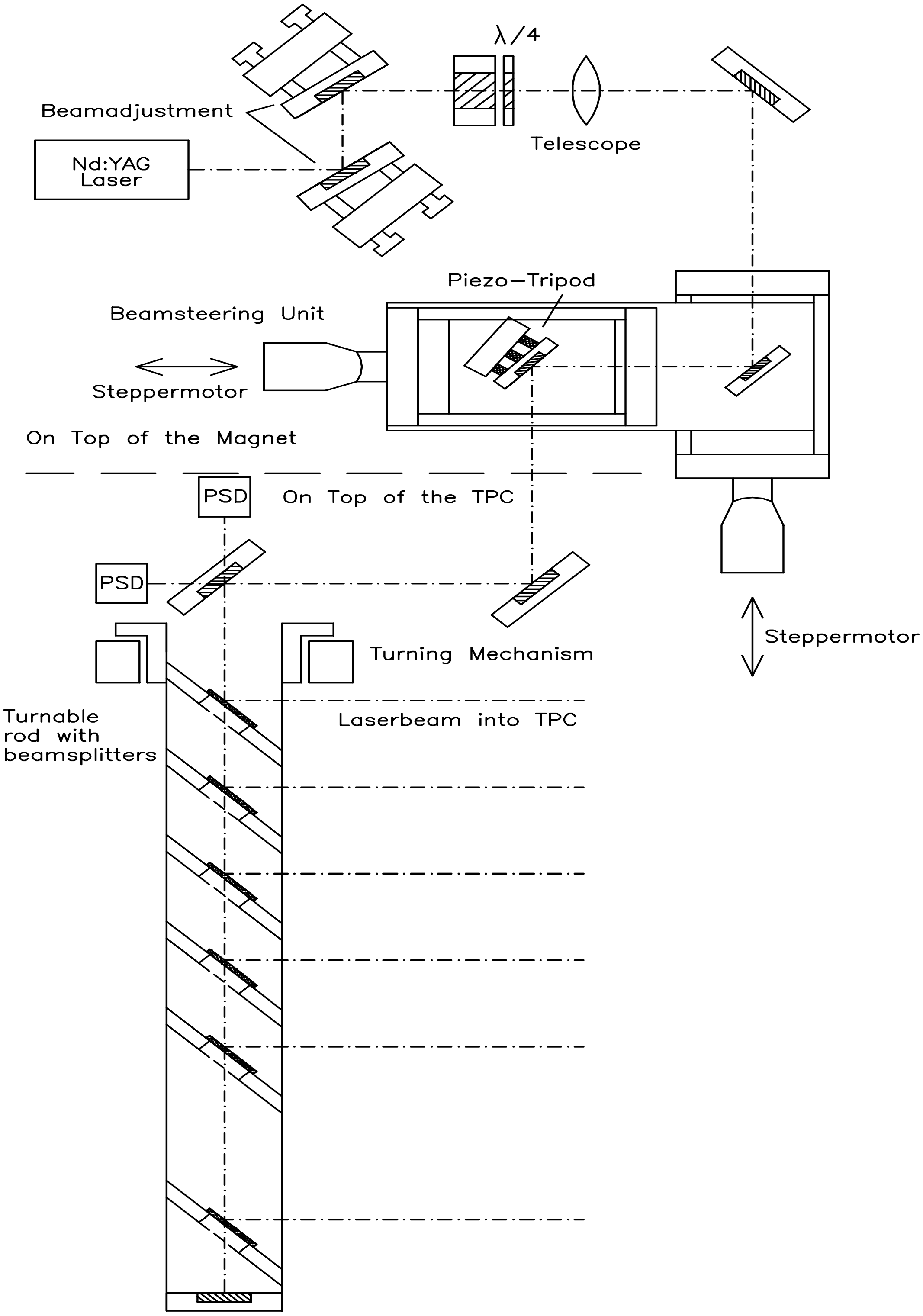

Figure 2.6: Schematic view of the components of the NA49 laser system

element, the turning mechanism is located. This turning mechanism is mounted on the TPC support frame and is completely free of magnetic parts(due to the magnetic field). The purpose of the turning mechanism is to distribute laser beams to different positions in the TPC as the turning mechanism rotates multiple beams at different heights to several different angular positions in the TPC's. The turning mechanism holds stiff, finely milled ceramic tubes which contain beam splitters to distribute the ionizing UV beams at 10 cm intervals throughout the volume of the TPC. The ceramic tube is held in place by a friction bearing and the movement is controlled by a mechanism resembling a balance wheel. A sequence of opening and closing two pneumatic valves activating two pistons moves the turning mechanisms in 3 degree steps. Two position sensitive diodes mounted on the turning mechanism are used to monitor the position of the beams.

Chapter 3

MTPC Event Reconstruction

3.1 Introduction

The MTPC event reconstruction package is known as MTRAC(Main TPC Reconstruction and Analysis Code). Its function is to take the raw data(existing as digitized ADC counts on each pad in the chamber, each with 512 time buckets) and organize it into a final track data structure. This final structure includes the found clusters and tracks, along with the track momentum, dE/dx, and other spatial information. The four main components of MTRAC are as follows:

- cluster finder, to organize the ADC counts into distinct groups
- track finder, which uses the found clusters to establish single particle tracks
- momentum reconstruction module

- dE/dx Client

The cluster-finder and track-finder use algorithms to search for cluster and track patterns, and then organizes these patterns into a subset of useable information. The momentum reconstruction module swims the straight tracks found in the MPTC's back through the magnetic field in order to determine a momentum value. The dE/dx module then uses the found charge clusters for each track to determine a truncated mean charge value for each track. All this information is stored in the global data structures defined for the MTPC analysis environment, which is then transferred to a DST(Data Summary Tape) to be used for the offline analyses.

3.2 Cluster Finder

The MTPC cluster finder contains algorithms which reduce the complicated 3-dimensional array of ADC counts to an organized set of clusters for a given event. The final cluster information contains the coordinates of the given cluster, the number of pads in the cluster, and the total charge of the cluster.

The reduction of the cluster information is done in several iterative steps. Each step makes the charge information more organized, localized, and compact, until the final clusters are produced. The four general steps of reduction include the following:

- **hits**
- **groups**
- **padclusters**
- **clusters**

A **hit** is defined to be a time-sequence of ADC values on a given pad where the start and the stop of the sequence is triggered by a cut on the ADC value, which is called the 'threshold' value. The threshold value is used to reduce the recording of noise on channels which are otherwise empty of any real signal. The threshold ADC value is 5 ADC counts. A hit may, and often does contain more than one peak.

A **group** is the second level of cluster organization. A group is defined to be the corresponding hit if the hit has only one peak. (refered to as a 'pure group') For hits which contain more than one peak, a group is defined as the sequence of all ADC values between the time minima of the hit, with the expectation that the multiple peak structure is due to multiple particle tracks.

A **padcluster** is the third level of cluster organization. A padcluster is defined to be a set of groups on neighbouring pads, whose peaks in the time direction(time centroids) are within a given range, set to be three time-slices. An additional criterion is that there must be at least 2 neighbouring groups to make a pad cluster, to allow for a gaussian fit to determine the cluster centroid. The average padcluster consists of 3 or 4 groups.(corresponding to 3 or 4 pad hits) These groups are merged in the pad direction into a padcluster. These padclusters may still contain multiple peaks in the pad direction.

A **cluster** is the last level or cluster organization, and is the final basic unit which is used in the track finding and fitting algorithms in the next step of MTRAC. A cluster is defined to be a padcluster if the padcluster has only one peak in the pad direction. If the padcluster has several peaks, it is split into several clusters such that each cluster contains only one peak in the pad direction. Now the charge information has only one peak in both the time and pad directions, and should be indigenous to only a single track.

The final charge of a cluster is simply summed in the time and pad directions, rather than fit. This method of dividing the charge between merged and overlapping clusters is less elegant and accurate than performing gaussian fits to the cluster to extract the charge. Fitting the clusters is another level of complication and much more time-intensive during the reconstruction phase, and so was not implemented in the first version of MTRAC. However the degradation of the dE/dx resolution(to be discussed in more detail in $\oint$ 6.3) in the high track density regions has led to the development of other cluster fitting techniques, using gaussian fits. These methods are presently being pursued and may be included to try and improve the dE/dx resolution in future data sets.

3.3 Track Finder

The MTRAC track finder uses the found clusters from the cluster finder as a set of 3 dimensional space points to begin trying to search for and identify all particle tracks that passed through the active volume of the MTPC. The track finder uses two different types of track finding with slightly different approaches in order to maximize the final number of found tracks. The two approaches are referred to as the 'Projective Tracker' and the 'Track Follower'. The first tracker uses a projection technique which projects a point through the TPC volume, sufficient for finding a majority of the obvious tracks.($\sim$ 80%) The second approach, which attempts to follow a trail of points, is sufficient for finding the remaining $\sim$ 20%.

The 'Projective Tracker' begins searching for tracks by projecting each cluster to the middle plane of the TPC using some initially arbitrary extrapolation point. Clusters are searched for in a box-like cell around this projection, and an initial fit and track estimate is performed if the number of clusters in the cell exceeds a given minimum number of points, which is usually 15. At this point all clusters in the cell whose distance to the initially fitted track is greater than a given value(called the 'fit distance') are dropped. The track is then refit with the remaining clusters, and all the clusters on this fitted track within a certain distance (called the 'hide distance') are marked to not be used for further track passes.

After the 'Projective Tracker' has found a majority of the obvious tracks, the remaining points are subjected to the 'Track Follower' to attempt to find any remaining tracks. This approach is sometimes referred to as 'follow your nose' style tracking. The 'Track Follower' uses an iterative approach which starts with an initial track, where the initial track is any point extrapolated to the next padrow-plane. In the next padrow plane the tracker searches for the cluster which is closest to the intial track. If there is a cluster in this plane closer than a given maximum distance, it is added to the existing initial track and the the track is refit. This procedure is repeated until one of the following conditions occur:

- There are no clusters closer than the maximum distance on a given number of planes past the initial plane
- There are no clusters closer than the maximum distance on a given number of successive planes
- All planes have been searched

At this point the tracker checks whether enough clusters(15) were successfully found. If so, a track has been found, and all cluster belonging to that track are marked as being found.

The total number of found tracks is shown in Fig. 3.1 for 1000 central events from run 808, '95 data set. The field configuration is STD+, which sends h+ to MTPCL and h- to MTPCR. The average number of negatives found is $\sim$ 315,

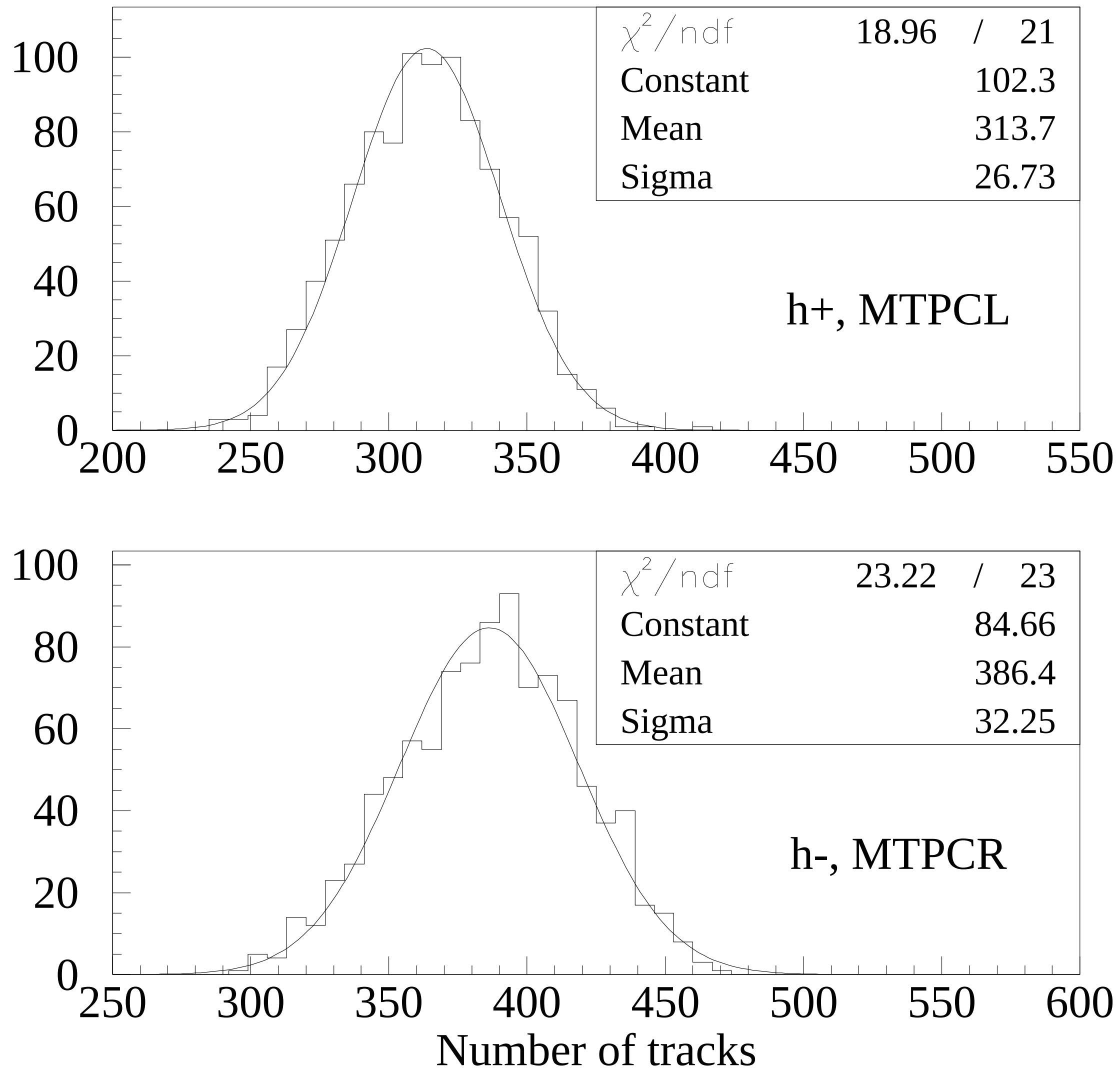

Figure 3.1: The total number of found tracks is shown for 1000 central events from run 808, '95 data set. The field configuration is STD+, which sends h+ to MTPCL and h- to MTPCR. The top histogram is h- in MTPCR, the bottom is h+ in MTPCL.

while the total number of positives found is ~ 385. The difference is, to first order, equivalent to the number of identified protons minus anti-protons. Secondary but significant differences occur from the asymmetries between positive and negative pions and kaons.

3.4 Momentum Reconstruction

After MTRAC has finished track finding, the momentum reconstruction module can access the found tracks with their 3-dimensional spacial orientations. The magnetic field in both vertex magnets has also been accurately measured[Lasi95]. The magnetic field strength vectors were measured with Hall probes in a 4x4x4 cm grid inside of both magnets. For tracks inside a magnetic field, the momentum of the track is determined in a straightforward manner from a measurement of the radius of curvature. In our field-free MTPC's downstream of the magnetic field, the known orientation of the track must be extrapolated backwards through the measured magnetic field. This extrapolation uses a Chebyshev polynomial transformation to determine the final momenta. In this transformation a Runge-Kutta evaluation of the transformation function is performed in 2 cm steps. The uncertainty in the momentum measurement, $\Delta p/p$, was determined to be ~ 2 MeV/c in the transverse(x,y) direction and ~ 5 MeV/c in the longitudinal(z) direction.

3.5 dE/dx Client

The dE/dx client follows track finding and is responsible for computing a truncated mean charge value for each track found by the track finder, using the cluster charges for all clusters on a given track. The truncated mean is calculated after a number of corrections have been performed to the raw cluster charge. An introduction to dE/dx, as well as a thorough discussion of the truncation and correction procedure is given in Ch.'s 4 and 5.

Chapter 4

Introduction to dE/dx

The primary method for particle identification(PID) in the NA49 TPC's is through the measurement of a particle's specific ionization deposited in the chamber. Time of Flight(TOF) techniques are also used, but TOF methods are very expensive over large solid angles and are most effective only at lower momenta($\leq$ 7 GeV/c). The choice of the NA49 MTPC's design parameters were motivated by the desire to achieve $\pi/K/p$ particle separation in the relativistic rise regime($\geq$ 7 GeV/c) via dE/dx ionization measurements.

By ionization measurement we mean an indirect estimate of the mean energy loss, Δ, of a charge particle as it passes through a gas-filled volume. The energy loss of a charged particle rises with $\beta\gamma$ and a measurement of it may be used to estimate the velocity. The physics of this energy loss has been well understood for many years, and this technique has been used extensively in high-energy physics detectors for almost two decades.

4.1 Bethe-Bloch equation

The basic physics of the energy loss by a fast-moving charged particle via its Coulomb interactions with charged particles in matter can easily be understood in terms of a semi-classical treatment[Fern86]. A particle of mass M, charge z_1e, and velocity v_1 is incident on a particle in some material with mass m, charge z_2e, and initially at rest. The interaction takes place at some impact parameter, b. The moving charge will create an electric field, whose transverse component will interact with the charged particles in the medium. The momentum transfer or impulse, Δp can be calculated, yielding the energy transfer ΔE. Because of the small electron mass, the energy loss is due primarily to collisions with the electrons in the material. If we integrate over the impact paramater range we get the total energy loss per unit length, dE/dx.

Such a semiclassical treatment of the energy loss gives an insufficient treatment of the quantum nature of the particles. A proper quantum treatment must include the quantum ideas that:

- energy transfer to the atomic electrons can only occur in discrete, quantized amounts
- the particles in question have a wave nature

In the early 1930's Bethe and Bloch properly treated the problem of energy loss in the framework of quantum mechanics. The mean differential energy loss dE in a distance dx is computed for particles with a mass m$\gg m_e$ by the Bethe-Bloche formula:

$$\frac{dE}{dx} = \frac{4\pi e^4 {z_1}^2 N z_2}{m\beta^2 c^2} \cdot \left(ln \frac{2m\beta^2 c^2}{I(1-\beta^2)} - \beta^2 \right).$$

where e is the charge of an electron, z_1 is the charge of the incident particle, N the number of atoms per unit volume in the material, z_2 is the atomic number of the material, m the electron mass, β=v/c, and I is the mean ionization potential for the given material. In later years this equation was discovered to be incomplete, and has since been modified to take two effects into account:

- the density correction δ in the case of ultra-relativistic particles
- the shell correction K, accounting for the electronic shell structure

Fermi first developed a theory of dielectric screening that explains the reduction of energy loss for distant collisions, known as the density effect. A thorough treatment of the density effect, including calculations for different materials has been performed by Sternheimer and Peierls[Ster71]. Ultra-relativistic particles polarize the medium with their strong transverse electric fields, causing a screening of the atomic electrons and a reduction in the energy loss, described by the factor δ.

This phenomenon is known as the density effect because it is dependent on the density of the medium. It causes the energy loss in the relativistic rise to increase as $ln\gamma$ instead of $ln\gamma^2$, and causes the loss to become constant at very large γ. The constant ionization loss at large γ is referred to as the Fermi plateau.

A shell correction K also reduces the amount of energy loss. This factor results from the fact that lower energy incident particles will not interact with the most tightly bound innermost electrons in the material. Thus the corrected form for the mean energy loss of ultra-relativistic particles takes the form:

$$\frac{dE}{dx} = \frac{4\pi e^4 {z_1}^2 N z_2}{m\beta^2 c^2} \cdot \left(ln\frac{2m\beta^2 c^2}{I(1-\beta^2)} - \beta^2 - \delta - K \right).$$

At NA49, dE/dx measurements are performed for different particle species (mainly $\pi^{\pm}, K^{\pm}, e^{\pm}, p, \overline{p}$) in the MTPC's. A momentum determination is made by swimming all particles back through the magnetic field. As a particle's momentum is only dependent on its mass and velocity, and since the mean dE/dx is only a function of a particles velocity, a mass determination is made. Different bands form for particles of different mass when dE/dx is plotted vs momentum. The distinct regions of behavior predicted by the Bethe-Bloch formula can clearly be seen in Fig. 4.1[Lehr83]. The ionization values initally fall off as $1/\beta^2$ for small values of β. The curves then go through minimum ionizing. The curves then rise as $ln\gamma^2$ until the density effect $\delta(\beta)$ causes the ionization to rise less steeply, as $ln\gamma$. The

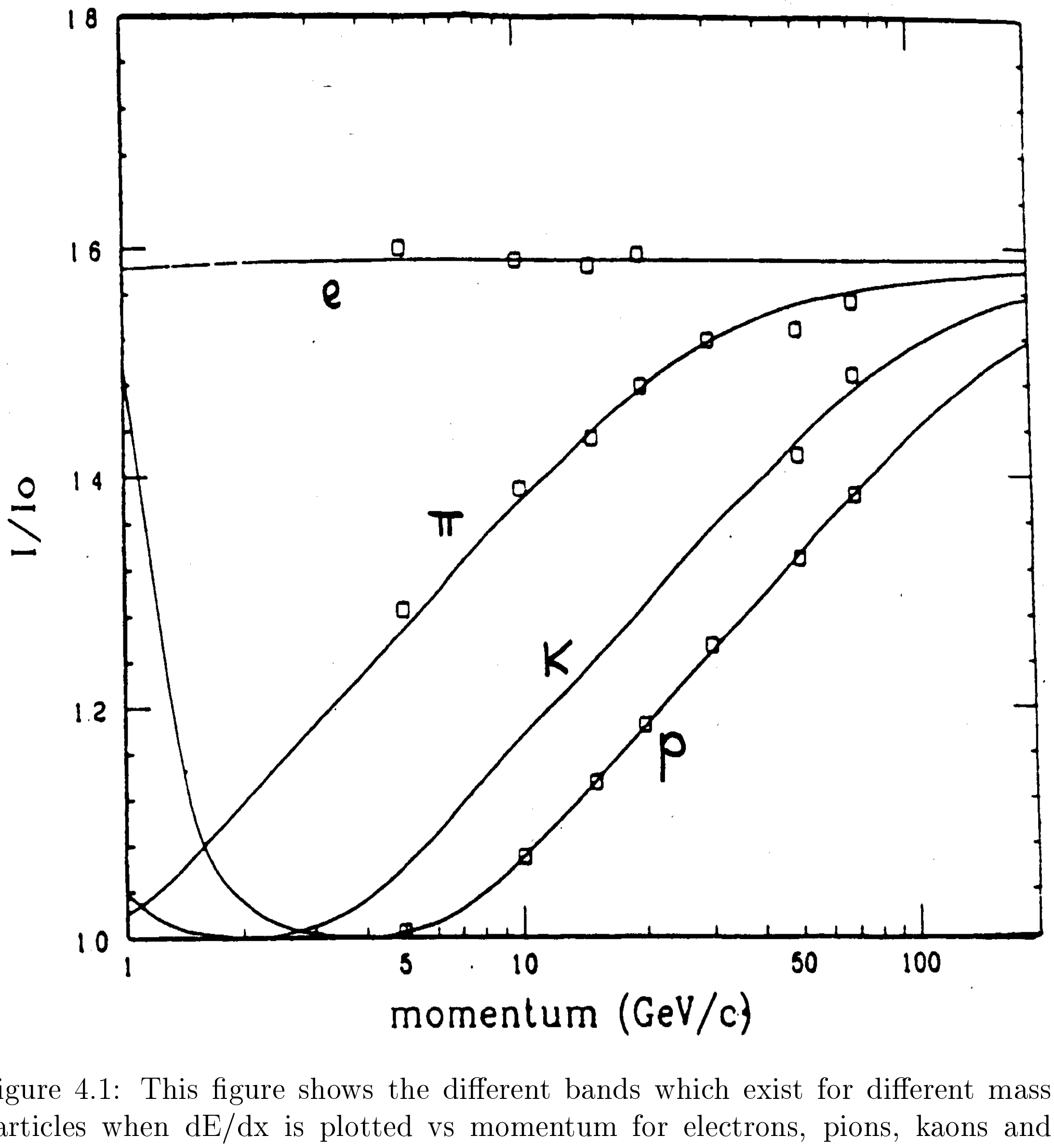

Figure 4.1: This figure shows the different bands which exist for different mass particles when dE/dx is plotted vs momentum for electrons, pions, kaons and protons. Here the dE/dx ionization(I) is normalized to minimum ionization, I_0. The $1/\beta^2$ region, mimimum ionizing, relativistic rise, and fermi plateau are all clearly seen.

ionization then saturates in the Fermi plateau as a constant energy deposition is reached for large values of β.

4.2 Truncation procedure

The energy loss predicted by the Bethe-Bloch equation only provides information about the average energy loss per distance by a charged particle. The actual energy loss of repeated measurements will vary due to statistical fluctuations. The most probable energy losses are those in the lower half of the range of possible energy transfers. The large energy transfer events are less frequent and are due to 'knock on' collisions with orbital electrons in which the maximum energy transfer can be achieved. These high energy recoil electrons are historically called 'delta electrons' or 'delta rays'. These less probable events in which delta rays are produced causes the energy loss distribution to be asymmetric with a tail on the high energy side, known as a Landau distribution. In Fig. 4.2 some Landau charge distributions are shown for the MTPC-R.

In order to obtain the optimum dE/dx value for a given track with multiple sampling, a 'truncated mean' procedure is used. This procedure for calculating the mean dE/dx value gives better resolutions than taking the simple mean of all the charge values in the Landau distribution. This is due to the fact that the high energy tail is more dominated by statistical fluctuations. The truncated mean

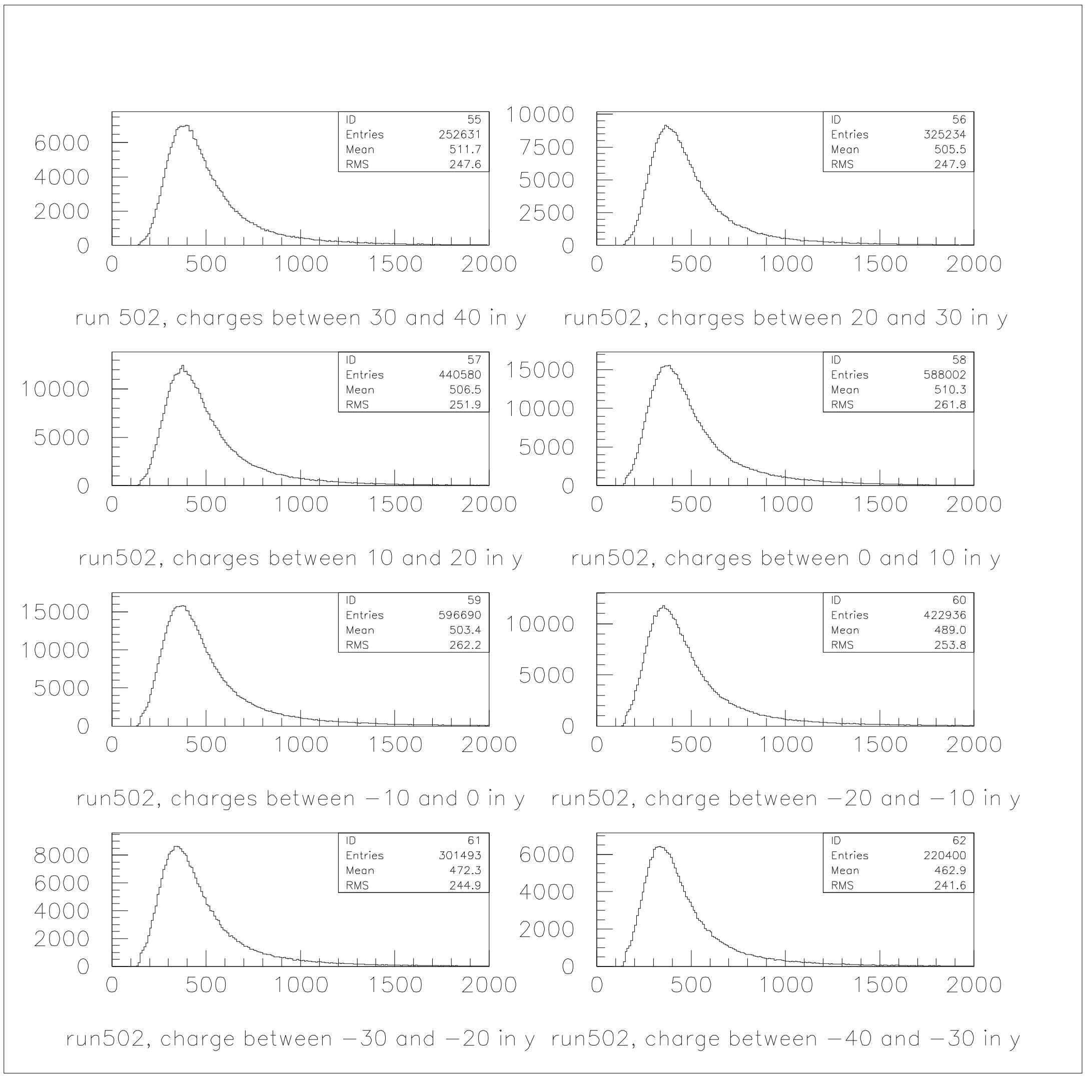

Figure 4.2: Typical Landau distributions in the MTPC-R for 100 events in run502, '94 data taking period. The charge distributions are split into clusters arriving from different 10 cm depth slices in the 1.2m total drift of the TPC. The Landau nature of the non-symmetric charge distribution is seen from the fact that the mean of the distributions are near 400 ADC counts whereas substantial charge values up to 1500 ADC counts are recorded.

procedure involves discarding the highest 30-40% of the charge entries, cutting away the high energy tail and leaving a distribution well approximated by a gaussian. For NA49 the truncated mean procedure involves discarding the top 35% of the measurements and the lowest 10%(which can suffer from various systematics), and computing the mean from this truncated distribution. This value is called the truncated mean charge, and contains the final dE/dx information for each track.

4.3 NA49 dE/dx Specifications

As previously stated the NA49 MTPC's were designed with the goal of achieving $\pi/K/p$ particle separation in the relativistic rise regime($\geq$ 7 GeV/c). This lead to certain design choices(pad lenth, total number of padrows, gas type and pressure) necessary to achieve a desired dE/dx resolution. Empirical equations describing the dE/dx resolution achievable in various gases have been developed by Walenta[Wale79] and Allision and Cobb[Alli80]. For the gas combination Argon-Methane(similar to the MTPC gas composition), the dE/dx resolution is found to be[Wale79]

$$\frac{\sigma(dE/dx)}{< dE/dx >} = 0.47 \cdot (pl)^{-0.32} \cdot N^{-0.43},$$

where l is the padlength in cm, p is the pressure of the gas in atmospheres, and

N is the number of samples taken(equivalent to the # of padrows in the NA49 MTPC's). For our chambers, l = 3.95 cm, p = 1 atm, and N = 90, giving a theoretical resolution of 4.4 %. A thorough discussion of the achieved resolution in the NA49 MTPC's will be presented in $\oint$ 6.3.3. The achieved resolution is a function of momentum, due to increasing track densities at higher momenta.

Chapter 5

Corrections to dE/dx

5.1 Correction Procedure

Several corrections to the raw cluster charge are necessary in order to determine an accurate and optimized truncated mean charge for a given particle. These corrections, each to be discussed, include the following:

- electronics gain calibration from pulser data
- gas gain 'kalibration' from kypton data
- effective tracklength correction
- y-dependent(drift direction) correction
- sector equalization

- time-dependent corrections

5.2 Electronics/Pulser Calibration

As mentioned earlier, the NA49 TPC's contain over 180,000 electronic channels. In order to compensate for the unavoidable gain variations in such a large number of readout channels, it is necessary to have a measure of the output of all channels to a known input signal, in order to calibrate and have a uniform gain across all channels. Therefore as a standard procedure in TPC experiments, field wires are pulsed with a pulser of known input. With respect to this response to a known uniform input a relative gain correction can be derived and applied to the raw data.

The calibration constants for NA49 are determined through the offline analysis of specific pulser runs, taken once per day during the run period in order to keep track of any time-dependent variations. All calibration constants are determined for each pad.

The pulser is capable of pulsing the fieldwires in a single shot mode or in a so-called 'ramp-mode'. In single-shot mode the pulser transmits single pulses at an arbitrary selectable pulseheight, while in ramp-mode it transmits succesive signals at a fixed frequency and equal pulseheight. This mode is used to model high track density in the chamber. One pulser run consists of 480 events with 16 different pulse heights(single-shot mode), and 270 events of the ramp-mode with up to 9 pulses of one single pulseheight. The relative gain constants are determined by performing a linear fit to the different pulseheights averaged over the corresponding 30 events. The offline gain calibration is performed with the inverse form of this relative calibration. At present the ramp-mode is not used for the calibration due to various difficulties.

The importance of the calibration is given by the magnitude of the non-uniformity of the electronics gain. In NA49 these effects are moderate but non-negligible as seen in the distributions determined in the single hit mode and displayed in Fig. 5.1 for a padrow of VTPC2[Kueh95]. The width of the gain distribution before the calibration has a $\sigma = 9.5\%$, while the uniformity of the gain response after the calibration is better than 1%.

5.3 Gas Gain/Krypton Calibration

In addition to the pulser calibration, a very similar procedure is used to correct for variations in gas gain across the chamber due to such things as mechanical imperfections of construction materials(such as sagging wires or variation in wire spacing) or edge effects. This gas gain correction can be determined by the use of a krypton soure (^{83}Kr), for which the charge spectrum and therefore the charge deposited in the chamber is very well known[Whit95]. The Kr source has a 3 peak

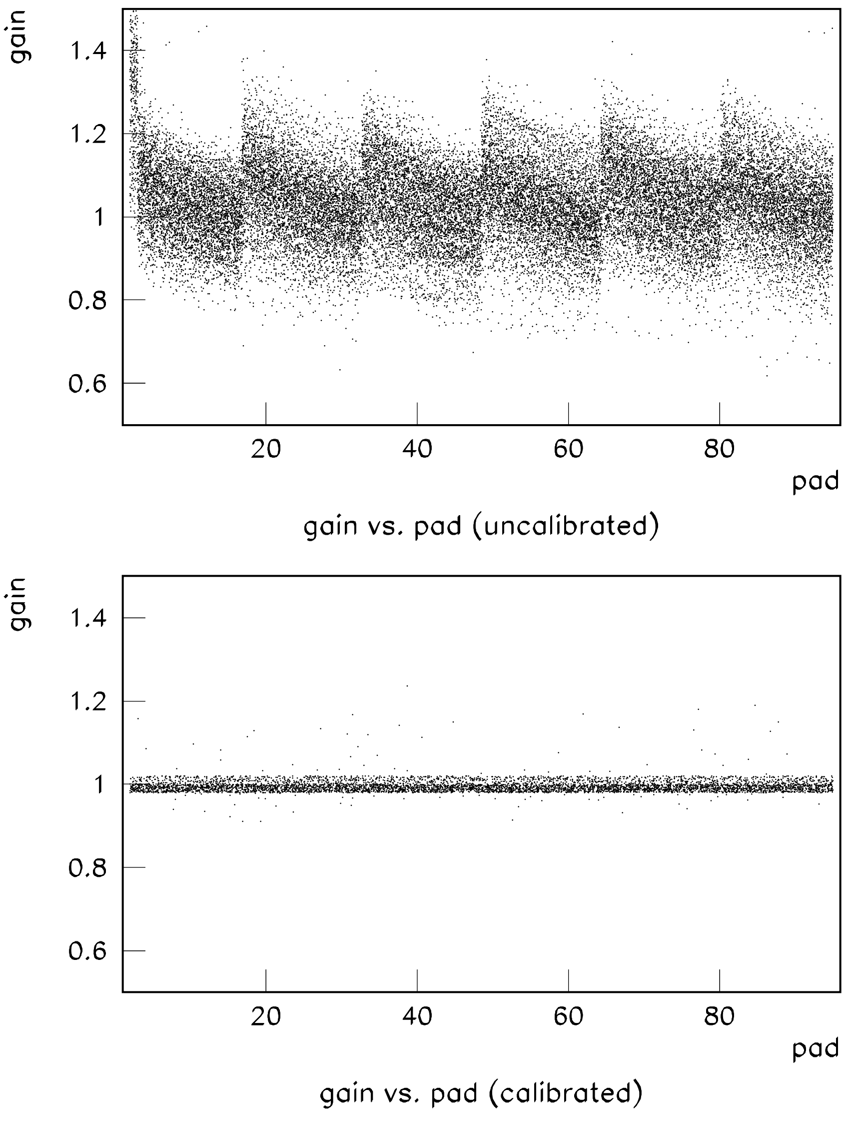

Figure 5.1: Uncalibrated and calibrated gain constants vs padnumber for a padrow in VTPC2.

structure which stems from a 41 KeV sum peak and 9 and 31 keV single peaks of the decaying electrons. In applying this correction, a pad area correction must also be considered. The ionization induced by the krypton decay will deposit a constant charge on the pad plane independent of pad area, and thus a correction must be made for the different pad sizes in the TPC's. If, after correcting for pad area and electronics gain, we continue to see variations in the charge distribution, we know that these variations must be intrinsic to the TPC and need to be removed.

The kryton calibration proceeds by determining the relative changes in gas gain from some standard reference distribution. In the context of the MTPC, each pad row($18 rows * 25 sectors = 450$) is subdivided into 6th's ($450 * 6 = 2700$), and then for each of these subdivisions a charge distribution histogram is produced and compared to an arbitrary reference histogram. A multiplicative factor is then determined to match the reference. This relative factor is a measure of the gas gain for that section of the TPC and is called a kalib factor. When done for all 2700 distributions, a set of krypton calibration factors are generated which show not only global sector-to-sector changes in gas gain but also local variations on the level a few percent within one pad row. Fig. 5.2 shows the final kalib factors for the MTPC[Ferg95]. The large discontinuity is the break between the HR and SR sectors. As is seen from the distribution there is about a 15-20% difference in gas gain between the HR and SR sectors. The behavior and shape of the kalib factors has the inverse shape of the average raw charge per sector, shown in Fig. 5.3. The

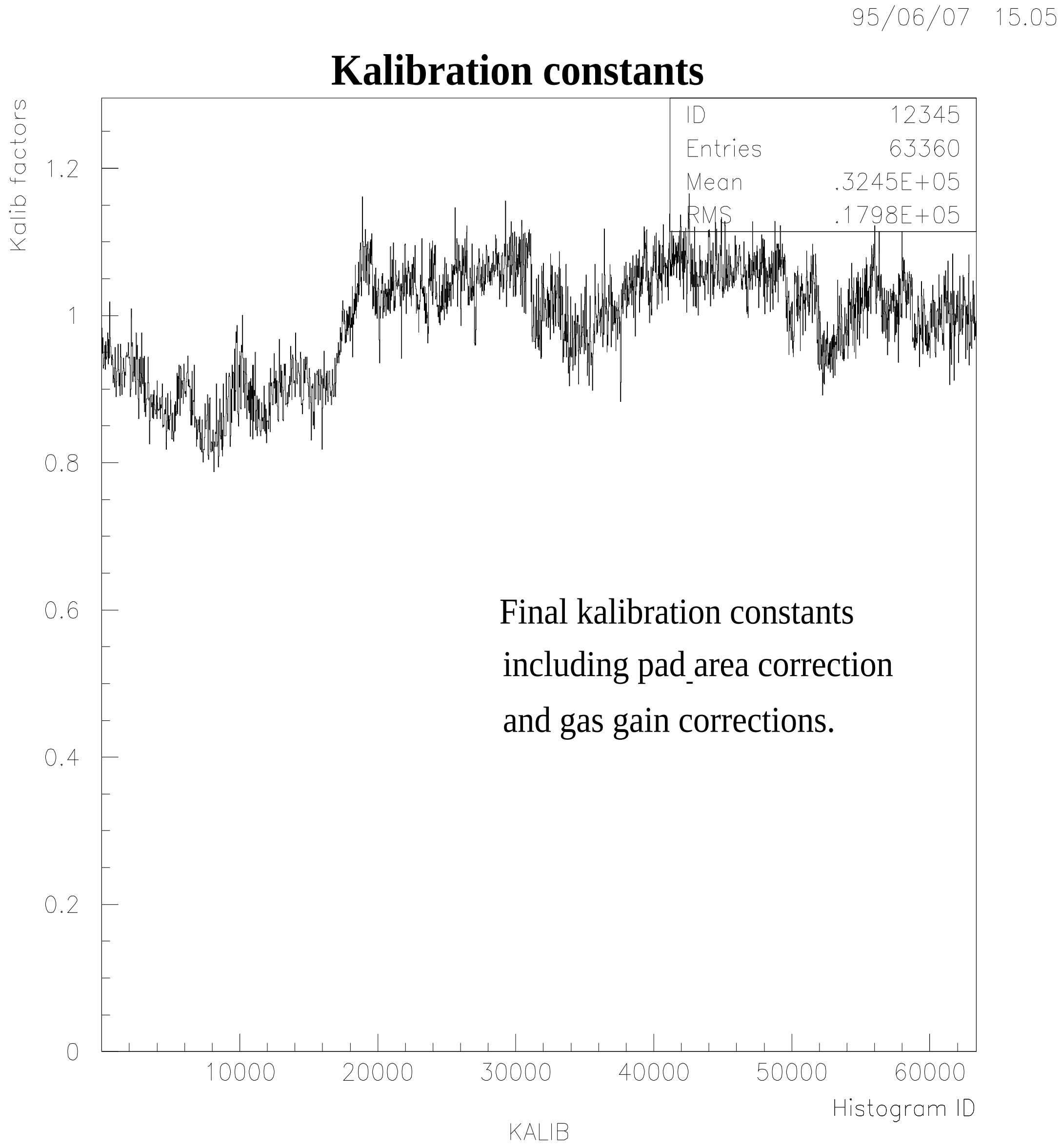

Figure 5.2: kalib factors are shown for the MTPCR, sectors 1-25, from left to right. The discontinuity takes place at the break between the HR and SR chambers.

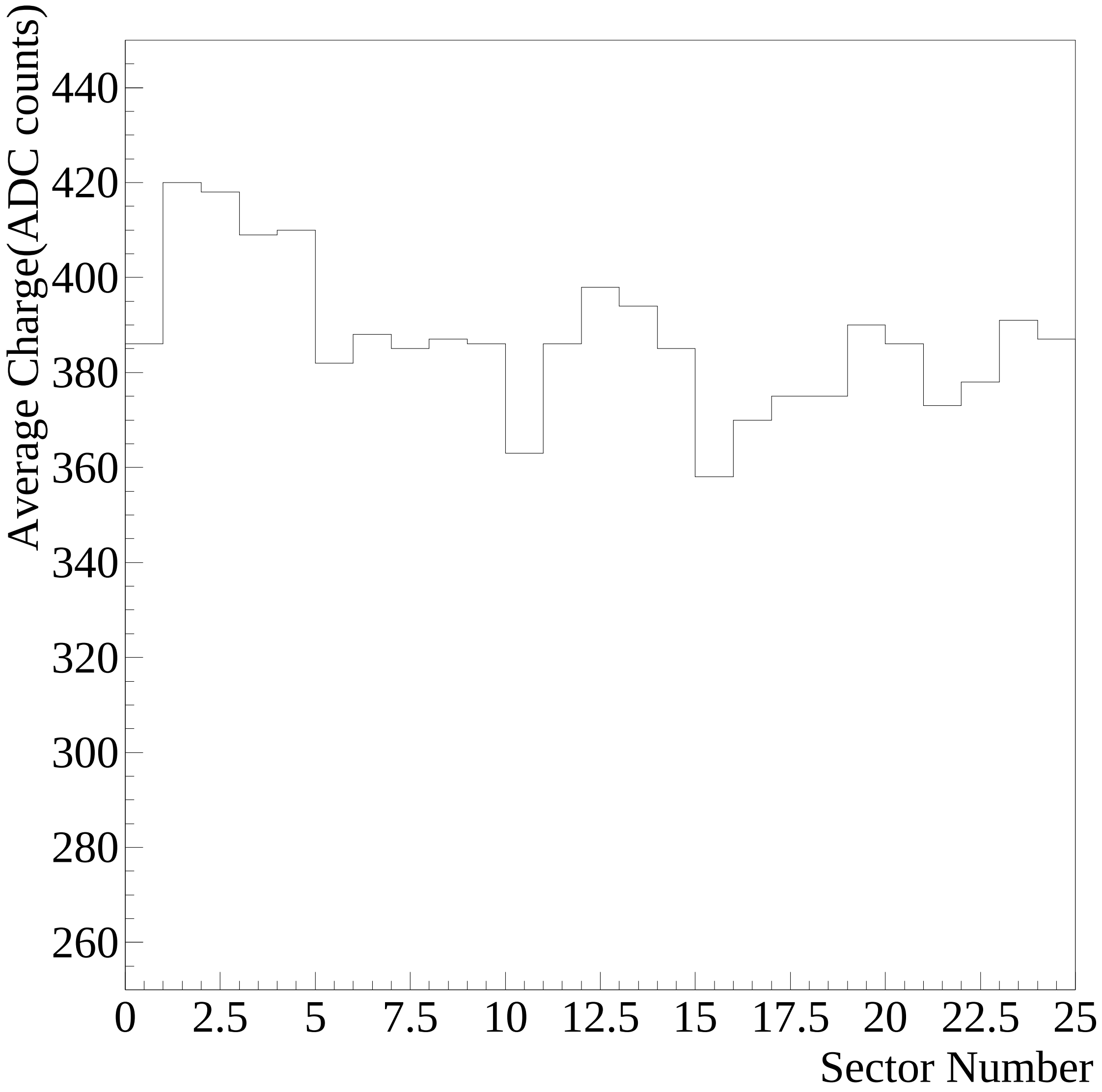

Figure 5.3: Average raw charge(in ADC counts), for the 25 sectors of MTPC-R for run 502, '94 data run. Sectors 1-5 are HR sectors(higher gain), sectors 6-25 are SR sectors.

correlation between these two shapes is very encouraging, assuring us that the gain differences seen in the krypton data exist and are being corrected for in the actual data.

The results of this calibration procedure(called kalibration) can be seen by examining krypton data after applying these corrections. Fig 5.4 shows the kalib factors after the kalibration has been applied. The kalibration factors are not applied to the exact same data from which the kalibration was determined, so the resulting distribution is not completely flat. The remaining fluctuations are indicative of the statistics of the number of samples used for the kalibration, however the same charge per cluster is seen everywhere in the chamber to within 0.75%. The slight remaining difference between the HR and SR sectors is probably due to an imperfect pad area correction.

5.4 Effective Tracklength Correction

The effective tracklength correction is a straight-forward geometrical correction due to varying tracklengths of particles in the TPC's. Tracks passing throught the chamber with some horizontal angle(λ) or dip angle(ϕ) will have a longer geometrical pathlength than a track passing through the chamber parallel to the beam direction and with no dip angle. As ionization is deposited roughly equally along the length of the track, those particles with longer pathlengths will artificially

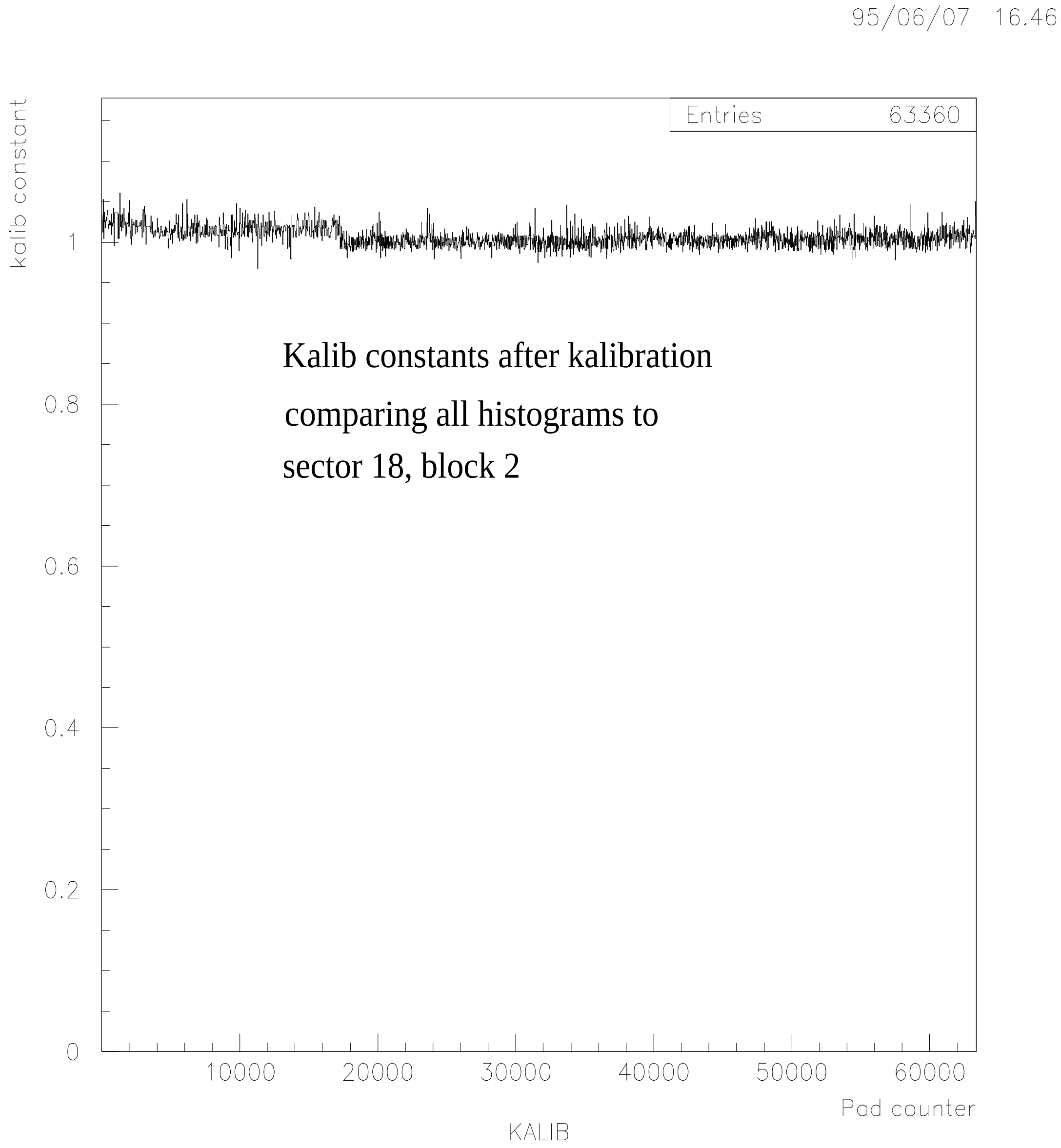

Figure 5.4: kalib constants after the krypton kalibration has been applied. The charge response is now very uniform chamber wide to within .75%.

deposit more charge than the $\lambda = \phi = 0$ tracks. In the correction all tracks are scaled to the same length via a correction of the form:

$$Q_{corrected} = Q_{measured} * cos(\phi) * cos(\lambda).$$

Fig. 5.5 shows the net effect of this correction. The net result of the track-length correction lowers the truncated mean charge distribution down 2.3%, which corresponds to the average $cos(\phi) * cos(\lambda)$ value for all tracks in the MTPC's.

5.5 Drift-dependent Correction

A crucial correction to the raw cluster charge comes about from the y-dependent(drift direction) losses the ionization experiences. The main sources of y-dependent charge losses are thought to be due to:

- electron attachment due to electro-negative gas contaminants such as H_2O and O_2
- threshold losses from zero suppression, which truncate the tails of the diffusing charge distributions

To first order the loss due to electronegative contaminants is due to O_2. Losses from H_2O are at least an order of magnitude smaller[Fisc94]. Electron attachment due to O_2 follows an exponential in drift distance dependent on the quantity of O_2 present. The form of the loss is given by:

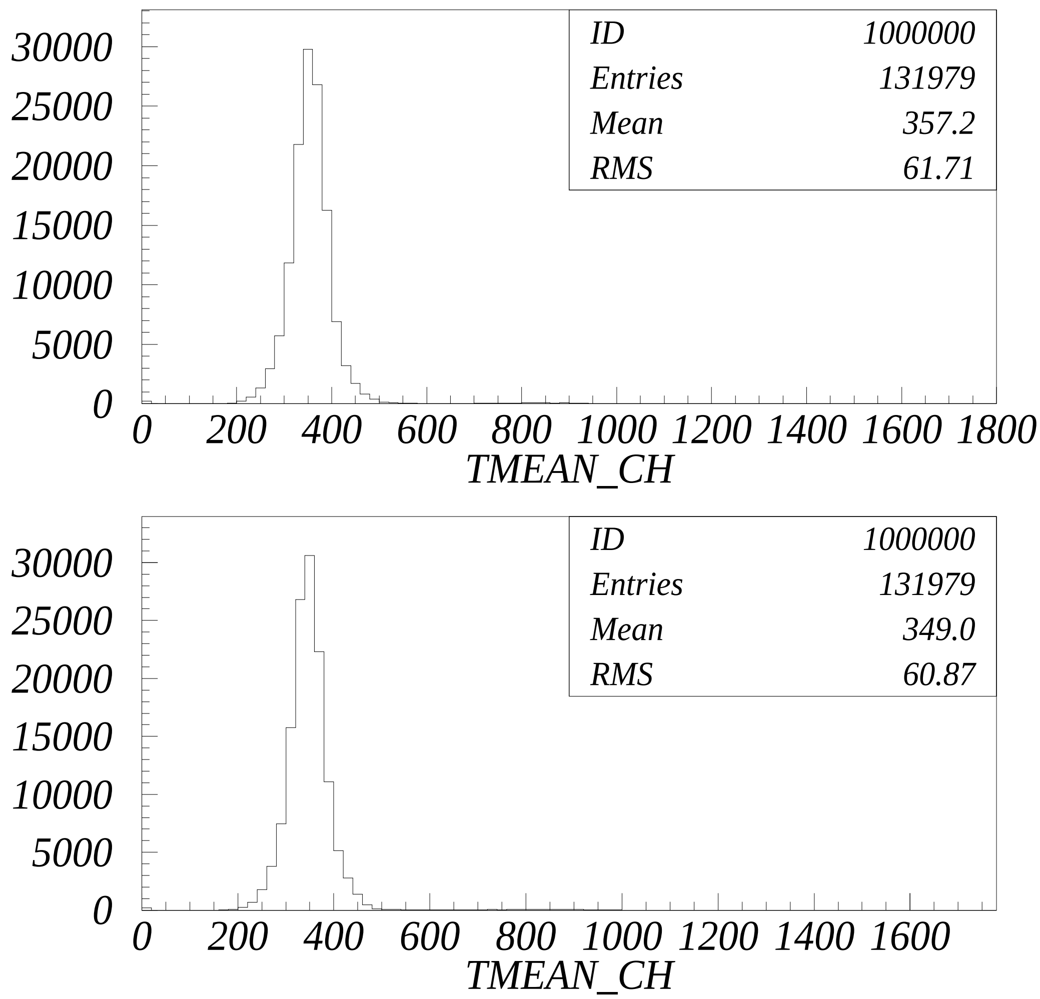

Figure 5.5: Truncated mean charge distributions for all particles in MTPCR before and after the effective tracklength correction. The truncated mean shifts down by 2.3% after the correction, as expected from the average azimuthal and dip angles in the chamber.

$$N(y) = N(0) * e^{-(PPM(O_2)*C)*y},$$

where N(0) is the original number of electrons, N(y) is the number after drifting some distance y, $PPM(O_2)$ is the parts per million of O_2 contamination in the gas, and C is some constant depending on the gas composition. A study of the coefficient C has been performed[Weni95]. The value of C for the MTPC gas composition is $1.6 * 10^{-4}$/cm. The loss is $\sim$ linear for low values of $PPM(O_2)$ and equals $\sim$ 0.75 %/($PPM(O_2) * m$). Average O_2 levels in the chamber are $\sim$ 6-7 PPM giving about a 5 %/m effect.

Threshold losses result from the zero suppression algorithms used after cluster finding to reduce the amount of data actually written to tape. Clusters are found by scanning the TPC pad signals in the time direction for at least two consecutive time buckets which have a signal greater than a prescribed threshold. The threshold is used to reduce the recording of noise. However the threshold settings also cut off the tails of the signal. A simple analytical method has been developed to determine how much charge loss is caused by the loss of the tails of signal, and to determine how the loss depends on pad width, time bucket size, diffusion constants and drift distance[Brad96]. The effects of diffusion, pad response, and electronic shaping produce a signal which can be approximated by a gaussian both as a function of time and pad direction. It is found that the correction to the cluster charge is expected to be inversely proportional to pad width(w) and time bucket size(Δt) and to be approximately linear in drift distance. It is also proportional to the ratio of the equivalent threshold charge(q_{th}) and to the total cluster charge(Q). The results of this calculation give a fractional charge loss $\Delta Q/Q$ as follows:

$$\frac{\Delta Q}{Q} \approx \frac{8.4\sigma_x\sigma}{w\Delta t}\frac{q_{th}}{Q} ,$$

where $\sigma_x^2 = \sigma_p^2 + \sigma_t^2 y$ and $\sigma^2 = \sigma_e^2 + \sigma_\ell^2 y/v_d^2$. σ_x describes the gaussian charge distribution along the pad-plane(x) direction, and σ describes the analogous distribution in the time(y) direction. σ_p is the pad response gaussian parameter and σ_t describes the diffusion charge gaussian in the tranverse(pad-plane) direction. σ_e is the preamp/shaper electronic time response, σ_l describes the diffusion is the longitudinal(drift) direction, and v_d is the drift speed in the TPC.

The following is a sample calculation using the above result, and some typical values from the NA49 MTPC:

Typical values: $\Delta t = 100ns$

$v_d = 2.2cm/\mu sec = 22\mu m/ns$ $\sigma_\ell = 310\mu/\sqrt{cm}$ $\sigma_e = 75ns$

$\sigma_t = 250\mu/\sqrt{cm}$ $\sigma_p(HR) = 2.2mm$ $\sigma_p(SR) = 2.8mm$

$q_{th}/Q \approx 1/80$ for $Q_{truncated}$, $w(HR) = 3.63$, $w(SR) = 5.45mm$

Fig. 5.6 shows a plot of the expected y dependence of the percentage charge loss, as based on the given paramters. Also shown are the values for charge loss

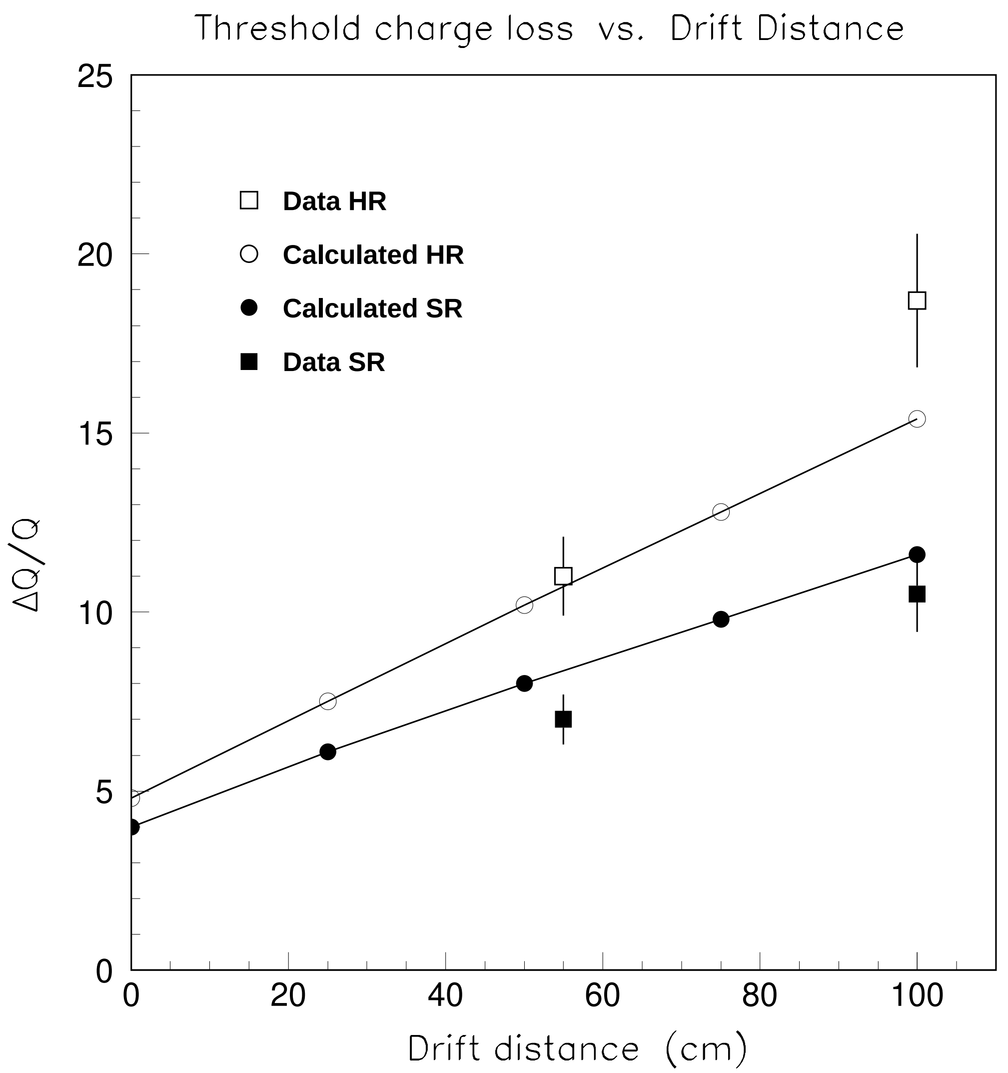

Figure 5.6: A plot (for SR and HR) of the expected y (drift distance) dependence of the percentage charge loss, as based on the above parameters for diffusion, drift velocity, pad geometry, etc. Also shown are the values for charge loss obtained from 1994 data. The latter charge loss values for these three runs have been corrected for oxygen attachment losses which averaged $\sim$5%.

obtained from 1994 data, runs 433, 443 and 502. The latter charge loss values for these three runs have been corrected for oxygen attachment losses which averaged $\sim 5\%$. As can be seen from the graph the combination of expected losses to due $\O_2$ contamination and the calculated threshold losses are in fairly good agreement with the data.

The final method for correcting for y-dependent losses is to perform an effective correction for all known and unknown effects, assuming an exponential form. Thus the form of the correction is

$$Q_{corrected} = Q_{measured} * e^{-\alpha y},$$

where y is the drift distance and α is derived from the data for each different type of sector in the MPTC's(HR, SR, SR'). Different coefficients are needed for the different types because different losses are seen due to differences in pad size and orientation. The data agrees nicely with the assumed exponential form, and since α is small, a linear fit describes the data well, as shown in Fig. 5.7.

The final drift correction factors used for the dE/dx analysis of the '95 data are shown in Table 5.1. Results are given in terms of (% charge loss)/m.

One additional correction was added to the y-dependent corrections in the 2nd reduction of the '95 data[Mock95]. In analyzing the '94 and first-pass '95 data the high momentum dE/dx information was falling short of Bethe-bloche predictions and making any parametrization in the region above $\sim$ 20 GeV(tracks mainly in

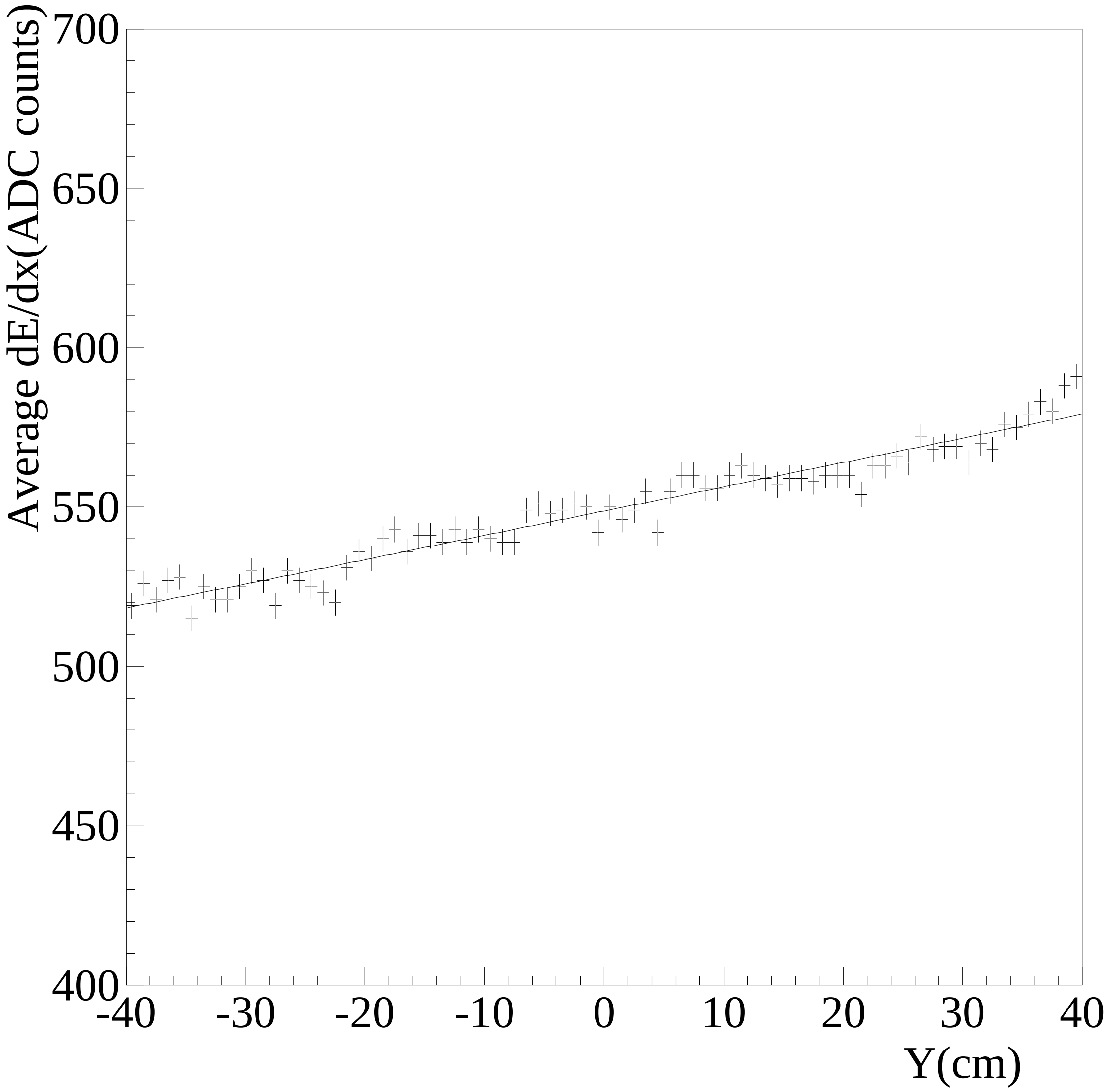

Figure 5.7: Shown is the y dependence of the average truncated mean for all particles in the MTPCR's HR sectors for run 502, '94 data. 0 is the midpoint of the chamber, so the loss over the middle 80cm of the 1.2m drift length is shown.

Table 5.1: Drift correction factors from the '95 data. All values are in units of (% charge loss)/m. L and R correspond to MPTC-R and MTPC-L.

configuration	Trigger	HR-L	SR-L	SR'-L	HR-R	SR-R	SR'-R
STD+	Central	25.1	19.6	17.5	19.4	15.4	13.1
STD-	Central	21.8	18.7	16.8	20.6	17.2	14.6

the HR region) difficult. Further analysis discovered that there was an additional non-linear loss in the HR regions of the MTPC around the mid-plane due to the high track density caused by the protons. Although these particles were found to be losing more ionization, they also have a higher dE/dx value due to there higher momenta values. These two competing effects made the average dE/dx vs y look flat and did not contradict a linear correction. When the average dE/dx vs y was examined for fixed high momenta, this additional loss in the high track density region was seen and corrected.

5.6 Sector Equalization

The combination of the pulser and krypton calibrations remove a majority of any global sector-to-sector gain variations. However gain variations still exist after these steps and must be removed. The most probable cause for these variations are differences in the high voltage supplies which feed each sector's anode wires, and difficulties matching the HR and SR gains with the krypton correction.

The procedure used to get the sector-correction constants involved analyzing data events with all other corrections performed. For $\sim 10^4$ events histograms were produced of the landau-distributions in each sector for different momentum bins. Since a particle's dE/dx value is momentum dependent, the relative sector-to-sector gains were derived by comparing two rows at a time(i.e. HR and SR) in a momentum range for which each type has high statistics. Once the relative sector-correction constants were found, a correction of the form

$$Q_{corrected} = Q_{measured} * C_i$$

was applied, where C_i is the sector-correction coefficient for the ith sector, where i = 1, 25 for the 25 sectors of each MTPC.

5.7 Time-dependent Correction

Fluctuations in temperature and gas density(correlated to air pressure) have been shown to cause variations in the energy loss of particles in a TPC's gas volume[OPAL87]. Since the air pressure and temperature constantly fluctuate with the weather, this will lead to time-dependent fluctuations in the average dE/dx. These factors, as well as any other unknown effects which degrade the stability of the gas over time, lead to the need for a time-dependent monitoring and correction of the dE/dx. One approach to correcting the dE/dx is to normalize the data on an event-by-event basis. With this approach, each acceptable track in a given event can be histogrammed according to there momenta, fit, and then renormalized to some arbitrary value. The concern with this approach is you may normalize out fluctuations in real physics, such as extra kaon production where the average dE/dx value per event should be different. Furthermore, even with $\sim$ 1000 tracks/event the corrections will be limited by statistics and negligibly useful. Another approach to correcting the data would be to try and understand the fluctuations in dE/dx from the measured pressure and temperature differences. This approach is presently being attempted and will be incorporated in next years production if successful. For this analysis, 50K events of STD+ and STD- (taken over several hours) provide sufficient statistics for the analysis and do not show any time-dependent effects, because of the brief time period.

Chapter 6

Parametrizing the dE/dx Data

6.1 Motivation

What we finally measure in our chambers is not the actual energy loss, dE/dx of the particles. We measure and record the result of a complicated process which includes:

- energy loss in the gas
- Production of primary and then secondary, etc. electrons
- Drift, diffusion, and then capture of these electrons
- The avalanche and amplification at the sense wires
- Pulse shaping and amplification in the front-end electronics

- The various software corrections discussed in Ch. 5

It is not reasonable to expect to be able to predict all these processes exactly, and thus know what absolute value of dE/dx we are recording. Furthermore, the functional dependence of the most probable energy loss is not well known for all gas mixtures, especially the non-standard mixes used at NA49. What is used to fit and understand the functional form of our dE/dx data in the relativistic rise is a parametrization of the most probable energy loss developed by the JADE collaboration[Ambr86] and then used in the TPC's of the mother experiment to NA49, NA35[Gunt94]. The parametrization is based on the Bethe-bloche formula with all the correction terms, but with 4 free parameters which are fit to describe the gas mixture and TPC systematics of the given experimental setup.

6.2 JADE Parametrization

The JADE parametrization of the relativistic rise contains the physics of the relativistic rise, with scaling factors to describe the differences in detector response and other systematics. The parametrization also has two parameters which describe the behavior of the relativistic rise, whose behavior varies for different gas choices. The general form of the parametrization is

$$\frac{dE}{dx}(\beta) = C_1 \frac{1}{\beta^2} \left(C_2 + ln \left(\frac{1}{1-\beta^2} \right) - \beta^2 - \delta(\beta) \right),$$

where C_1 and C_2 are constants to be fitted. C_1 is a factor describing the target electron density and acts as a scaling factor on the energy loss function. C_2 is a constant which determines the minimum ionization of the function.

The density correction term, $\delta(\beta)$, reduces the logarithmic $\ln\gamma^2$ rise of the energy loss due to the ongoing increase of β. The contraction of the particle's electric field into a strongly spiked tranverse electric field component(which is responsible for the increased energy loss in the relativistic rise) eventually causes dielectric screening as the medium polarizes, reducing the relativistic rise into the famous 'Fermi plateau'. This term, studied extensively by Sternheimer and Peierls[Ster71], and following there formalism, takes the form

$$\delta(\beta) = \begin{cases} 0 & for \;\; X_0 \\ 2ln(10) \cdot (X - C_3) + C_4 \cdot (X_1 - X_0)^3 & for \;\; X_0 < X \leq X_1 \\ 2ln(10) \cdot (X - C_3) & for \;\; X_1 < X \end{cases}$$

where $X = log(\beta\gamma)$. X_0 and X_1 are responsible for the distinct functional behavior of the relativistic rise and are given by

$$X_1 - X_0 = \left(\frac{2ln(10)}{3a} \right)^{\frac{1}{2}}$$

and

Parameter	Fit result
C_1	23.679
C_2	10.588
C_3	2.373
C_4	0.197

Table 6.1: The results for the four fit parameters of the JADE parametrization in the NA49 MTPC's.

$$X_0 = C_3 - C_4 \cdot \left(\frac{X_1 - X_0}{2ln(10)}\right)^3.$$

C_3 and C_4 are constants to be fit by the data; C_3 yields the height of the Fermi-Plateau and C_4 is a constant whose value depends on the spectrum of oscillator strengths and dispersion frequencies of the atoms in the given gas, according to the dispersion oscillator model used by Sternheimer and Peierls. As previously mentioned X_0 and X_1 describe the distinct functional behavior of the relativistic rise. After passing through minimum ionizing, the ionization rises in the relativistic rise as $ln(\gamma^2)$, with $\delta = 0$ up until X_0. At this point the $\delta(\beta)$ term kicks in and the ionization begins rising less rapidly, as $ln(\beta)$. The ionization loss rises as $ln(\gamma)$ until X_1, at which point the energy loss saturates in the Fermi-plateau.

The parametrization is used to normalize the experimentally measured dE/dx values, providing a global fit to the dE/dx values for all four different particle species($\pi^{\pm}, K^{\pm}, e^{\pm}, p, \overline{p}$), providing a smooth curve in $\beta\gamma$ space for all particle species at all momentum values. The results for all fitted constants of the parametrization are shown in Table 6.1.

6.3 Parametrization Procedure

The parametrization for the NA49 MTPC dE/dx information is derived from the data itself. If dE/dx information is binned in small momentum bins(~ 0.5 GeV/c) and plotted for all particles, different bands form for each particle as in Fig. 4.1. To obtain one global curve for all particles, dE/dx information is again histogrammed into small momentum bins but plotted vs $\beta\gamma$. Now all the dE/dx information is found on one curve, where different particle species are found on distinct regions of a global parametrization curve due to their differing masses(according to the Bethe-Bloche formula).

6.3.1 Fits

The dE/dx information for the different particle species in different momentum bins are derived from fits to the corrected dE/dx information. In order to avoid systematics between MTPCR and MTPCL, only data from MTPCR is used for the parametrization and subsequent data analysis. Positive and negative particle spectra can be looked at in the same chamber(MTPCR) by looking at different runs of the two standard magnetic field configurations; the STD+ configuration puts negatives in MTPCR, the STD- inverted field puts positives in MTPCR. The dE/dx information for MTPCR is binned into 0.5 GeV/c bins and plotted for STD- and STD+ as in Fig 6.1, where in this plot the $9 < p(GeV/c) < 9.5$ bin is shown. A clear difference between the positive hadron(h+) and negative hadron(h-) spectra is seen. This difference is due to the small production of anti-protons, compared with the large population of protons present, due to the initial baryon number in the projectile and target nucleons. A large central pion peak is visible for both h- and h+, however the kaon and proton peaks are not separable for the h+ spectra. They merge and form a shelf to the left of the pion peak. For the h- spectra this is not the case, since anti-proton production is a factor of $\sim$ 10 less than kaon production[Eckh96]. The roughly equivalent production of protons and K+, combined with small p/K separation(about 1/2 the π/K separation), makes extracting parametrization information from the positives difficult. For this reason the parametrization is derived from the negatives, for which the π^-, K^-, and e^- peaks are reliably found; the anti-proton peaks are not used because they are found less reliably. The anti-proton production rate is an order of magnitude less than the kaon production, swamping them in the noise of the kaon and pion tails. The parametrization derived from the negatives is then used for the positives, after checking that the pion peaks for the h- and h+ are the same. The pion peak for the h+ is still easily extractable, even if the K+ and proton peaks are not.

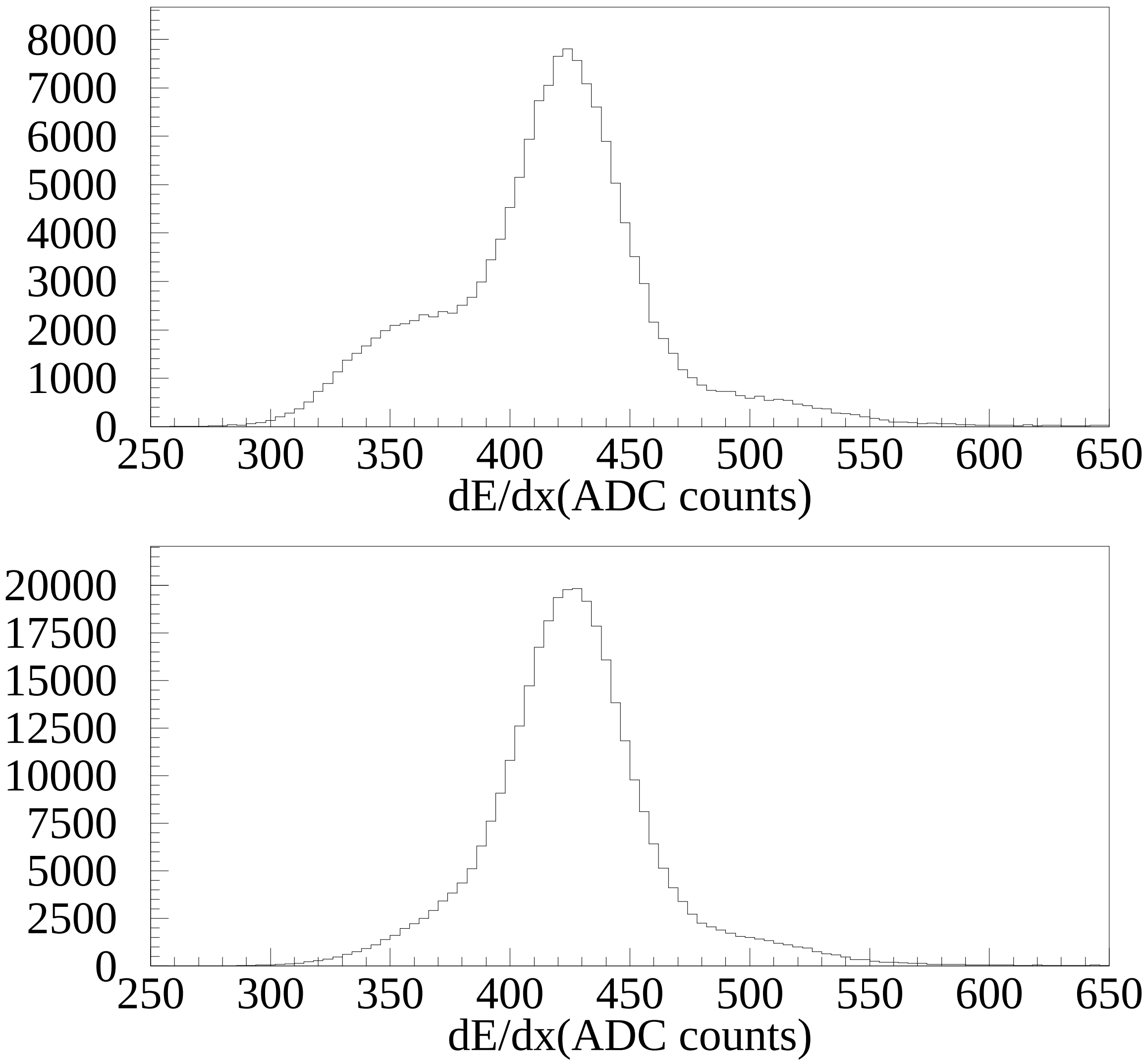

Figure 6.1: Plotted is the contrast between the dE/dx distribution for positives and negatives. The top plot shows positives, including protons, while the bottom plot is for negatives, with very little anti-proton contribution. Data shown is for the $9 < p(GeV/c) < 9.5$ bin.

The parametrization is derived from h- spectra in MTPCR, using ~ 40 K events from runs 808-820, in the '95 data set. The dE/dx spectra are fit in 0.5 GeV/c bins using a functional form which is a 9 parameter fit to the superposition of 4 gaussians for the 4 particle species:

$$F(dE/dx, p, C_i, \mu_i, \sigma_i) = \sum_i C_i \cdot exp\left(-\frac{(dE/dx - \mu_i)^2}{2\sigma_i^2}\right) \; with \;\; i = e^-, \pi^-, K^-, \overline{p}.$$

Here p is the momentum bin considered, the C_i's are the heights(or count) of each particle species at the mean energy loss($dE/dx = \mu_i$), μ_i is the mean energy loss for a given species, and σ_i is the width of the distribution for each species. The 9 parameters of the fit correspond to 4 heights(C_i's), 4 means(μ_i's), and 1 common percentage width(σ_i), as each particle's distribution has a similar percentage width.

The results of these fits to the h- spectra are shown in Fig. 6.2. Here data from 5-19 GeV/c are shown, histogrammed into bins of 0.5 GeV/c. Small momentum ranges are selected in order to minimize the spread in dE/dx due to the steady rise of the energy loss as a function of momentum in the relativistic rise. The 4 mean energy loss values(μ_i's) for each particle species, shown in these figures as vertical lines, are used to determine the parametrization.

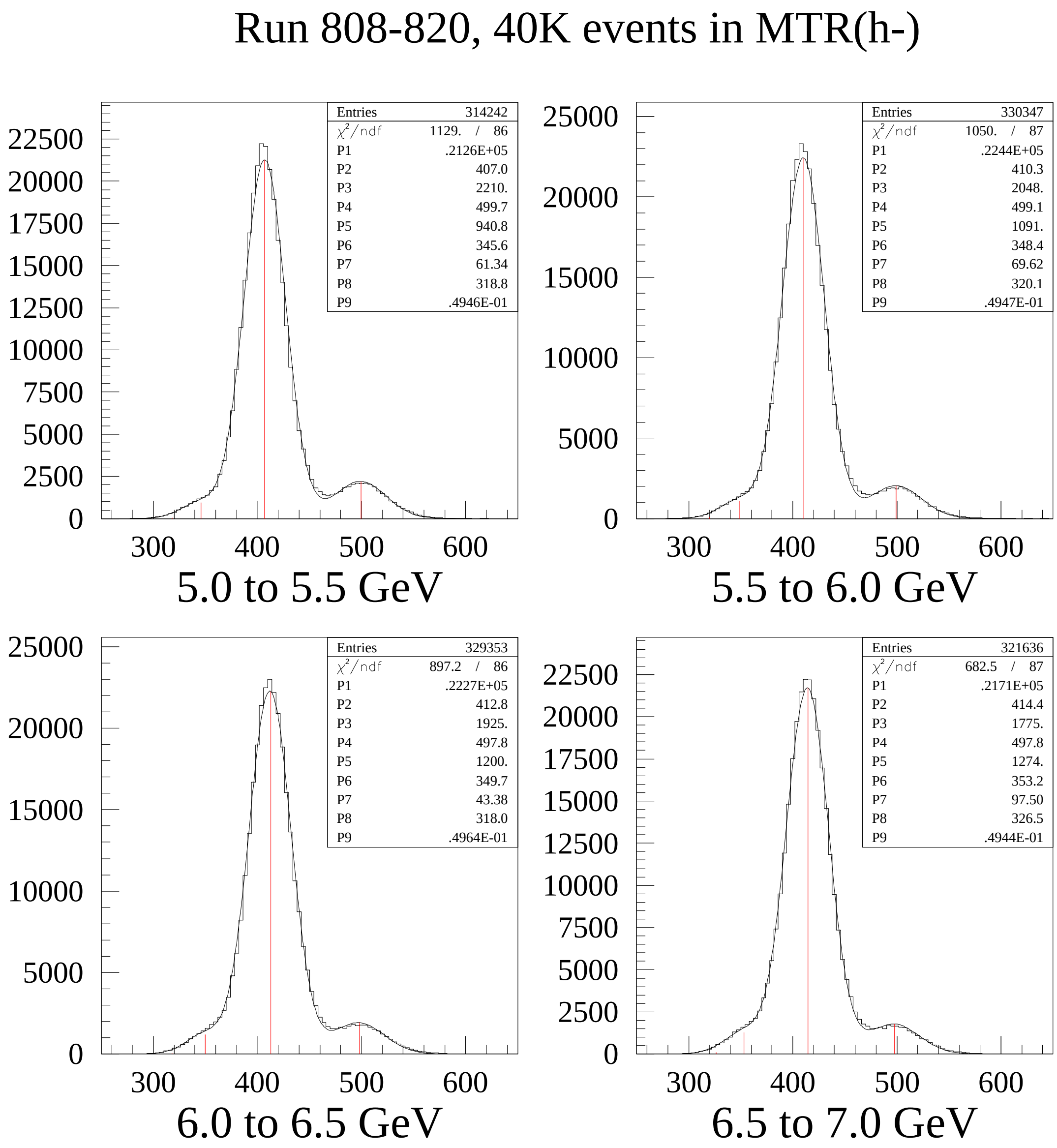

Figure 6.2: Results of the four-gaussian fits to negative hadrons(h-) for runs 808-820, '95 data. The four vertical dotted lines represent the gaussian heights of the 4 particle species. The largest central peak is that of the pions. The electrons are to the right of the pions and the kaons and the tiny anti-proton gaussians are to the left. The data shown are for momentum values from 5-19 GeV/c, binned in 1/2 GeV bins.

Run 808-820, 40K events in MTR(h-)

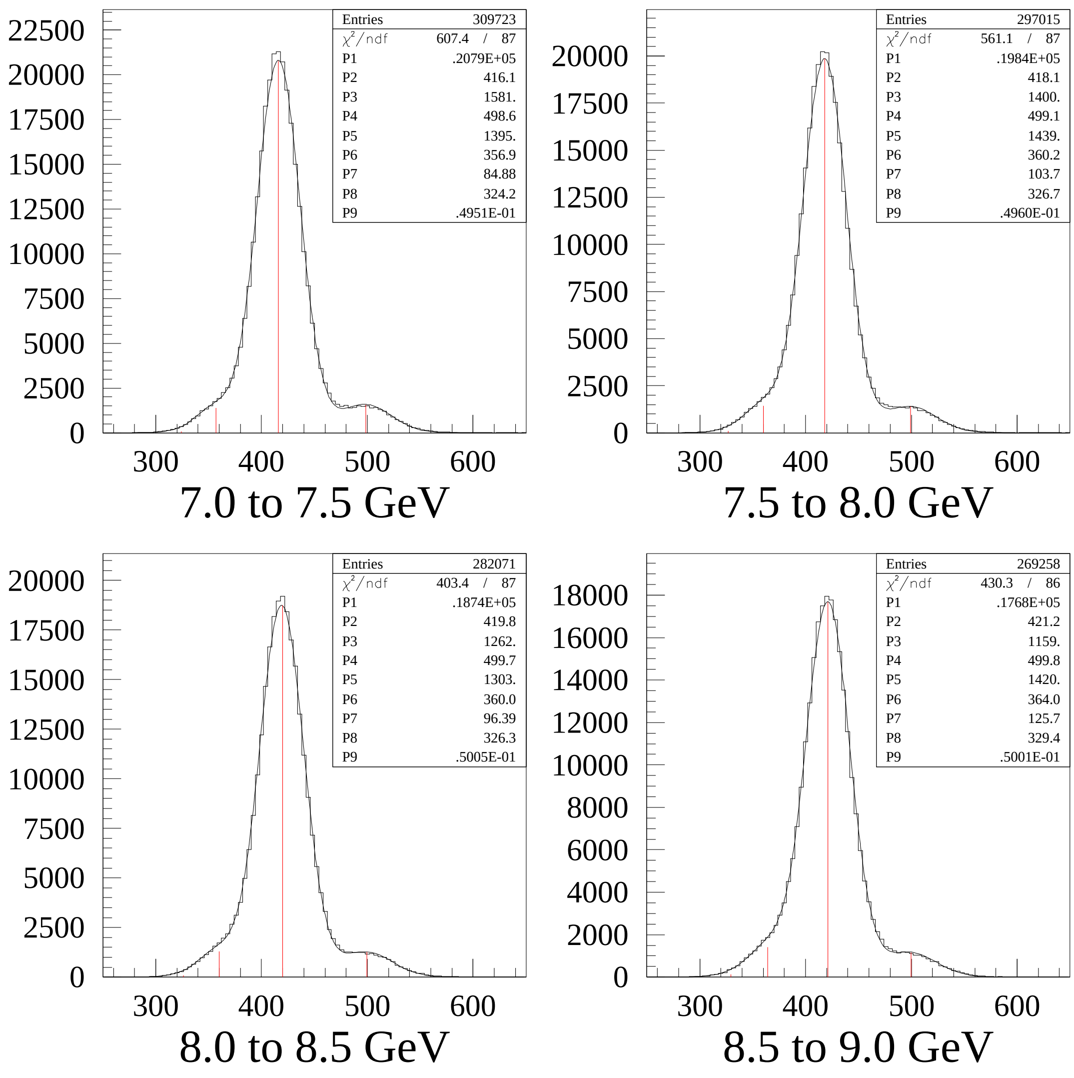

Run 808-820, 40K events in MTR(h-)

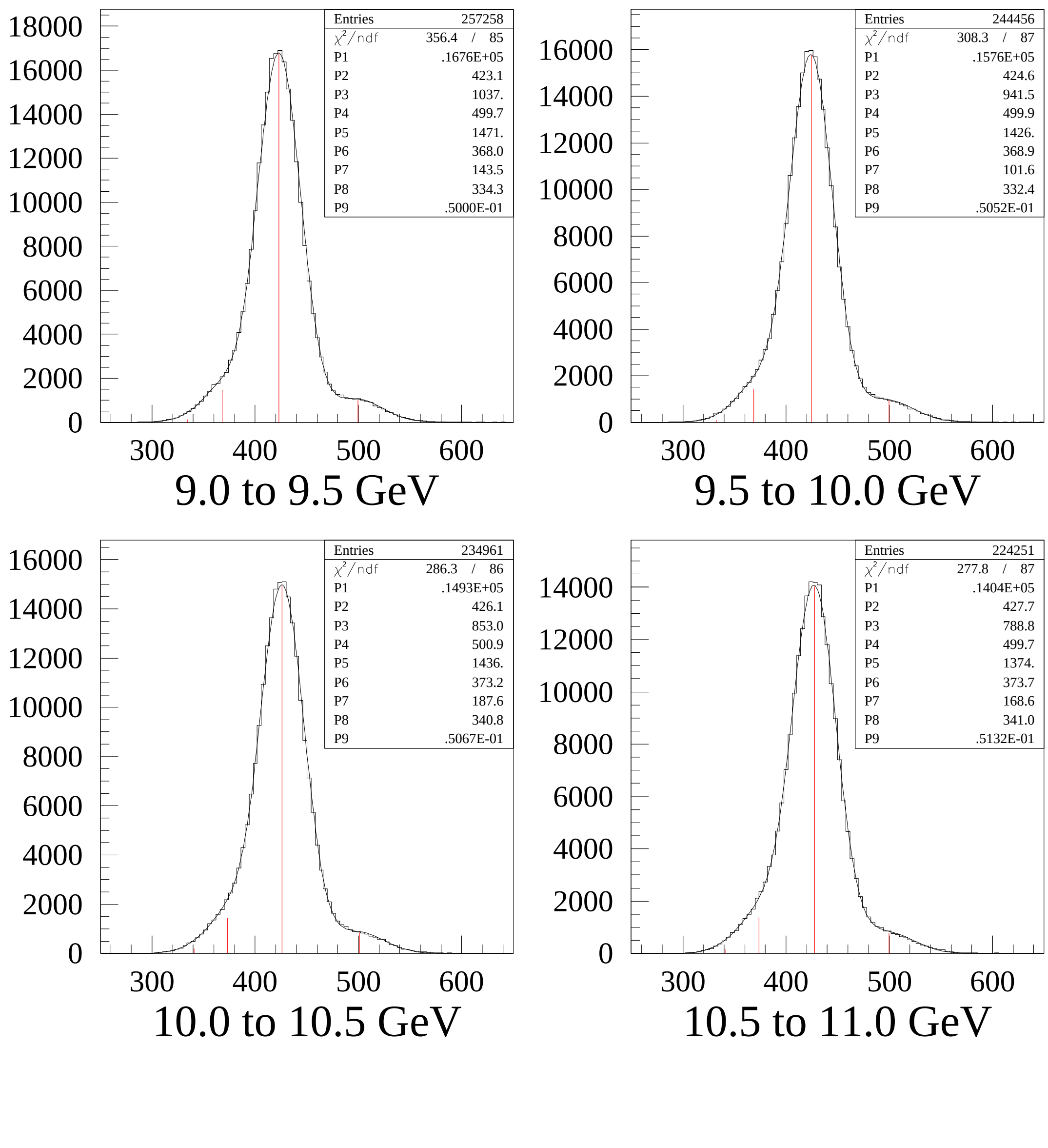

Run 808-820, 40K events in MTR(h-)

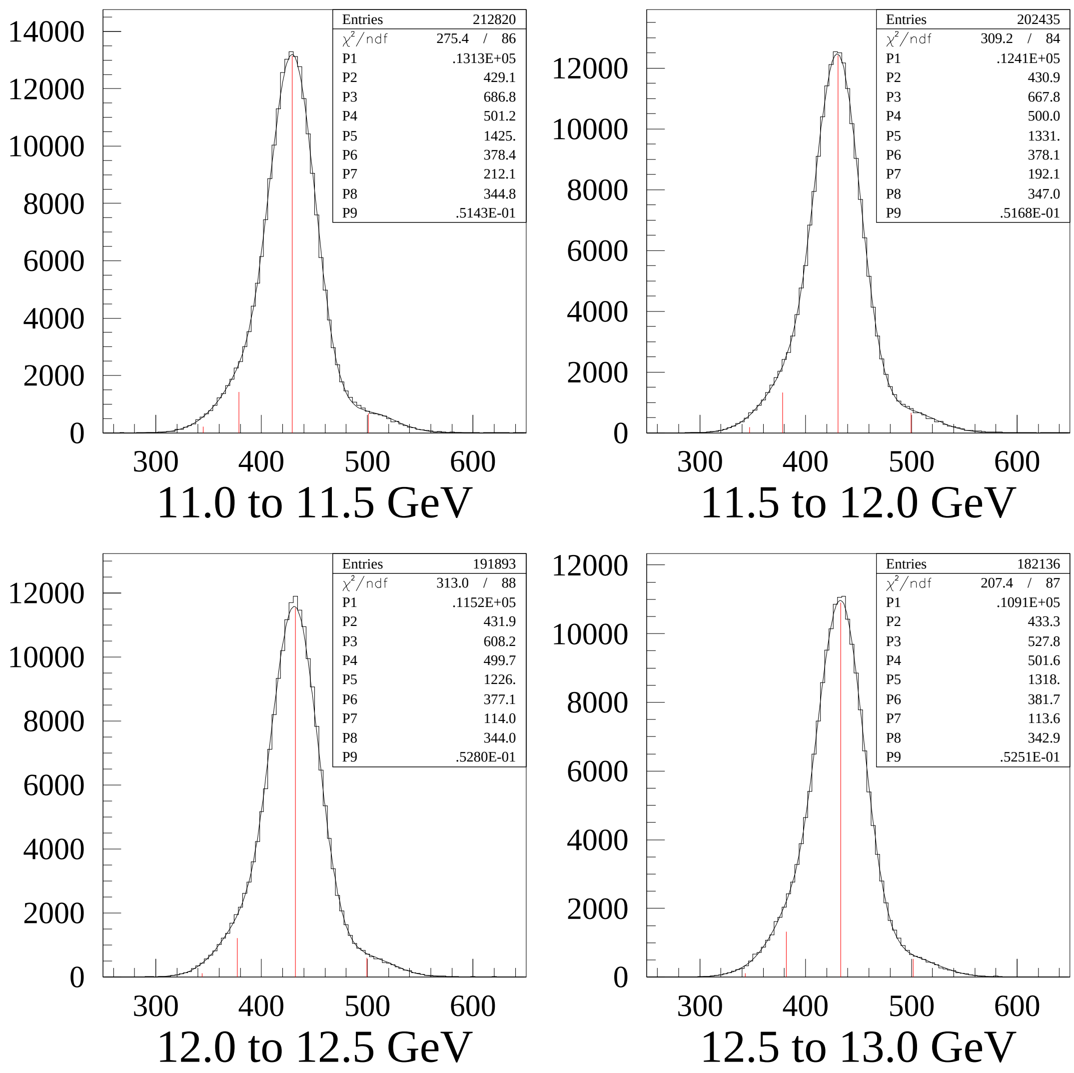

Run 808-820, 40K events in MTR(h-)

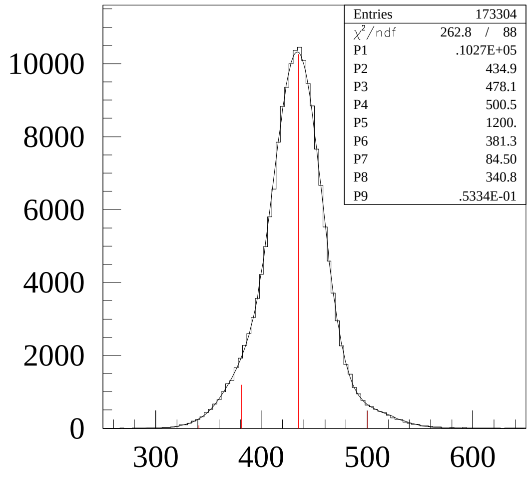

13.0 to 13.5 GeV

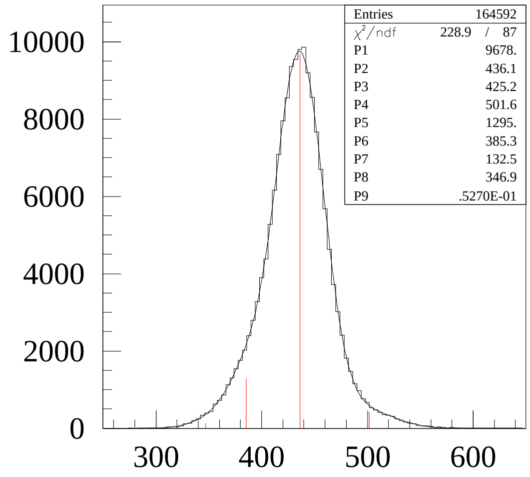

13.5 to 14.0 GeV

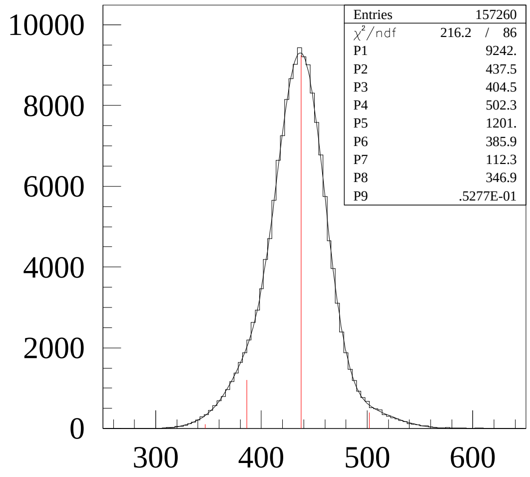

14.0 to 14.5 GeV

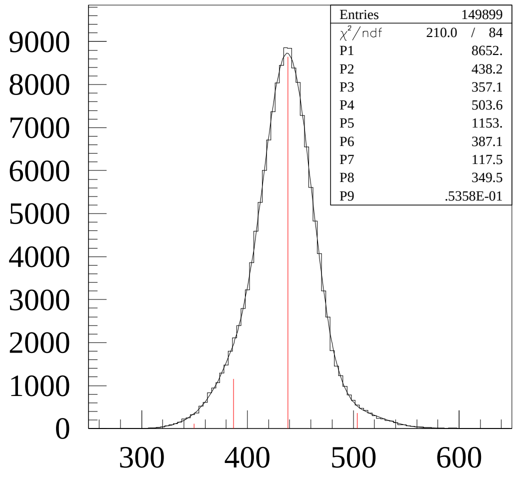

14.5 to 15.0 GeV

Run 808-820, 40K events in MTR(h-)

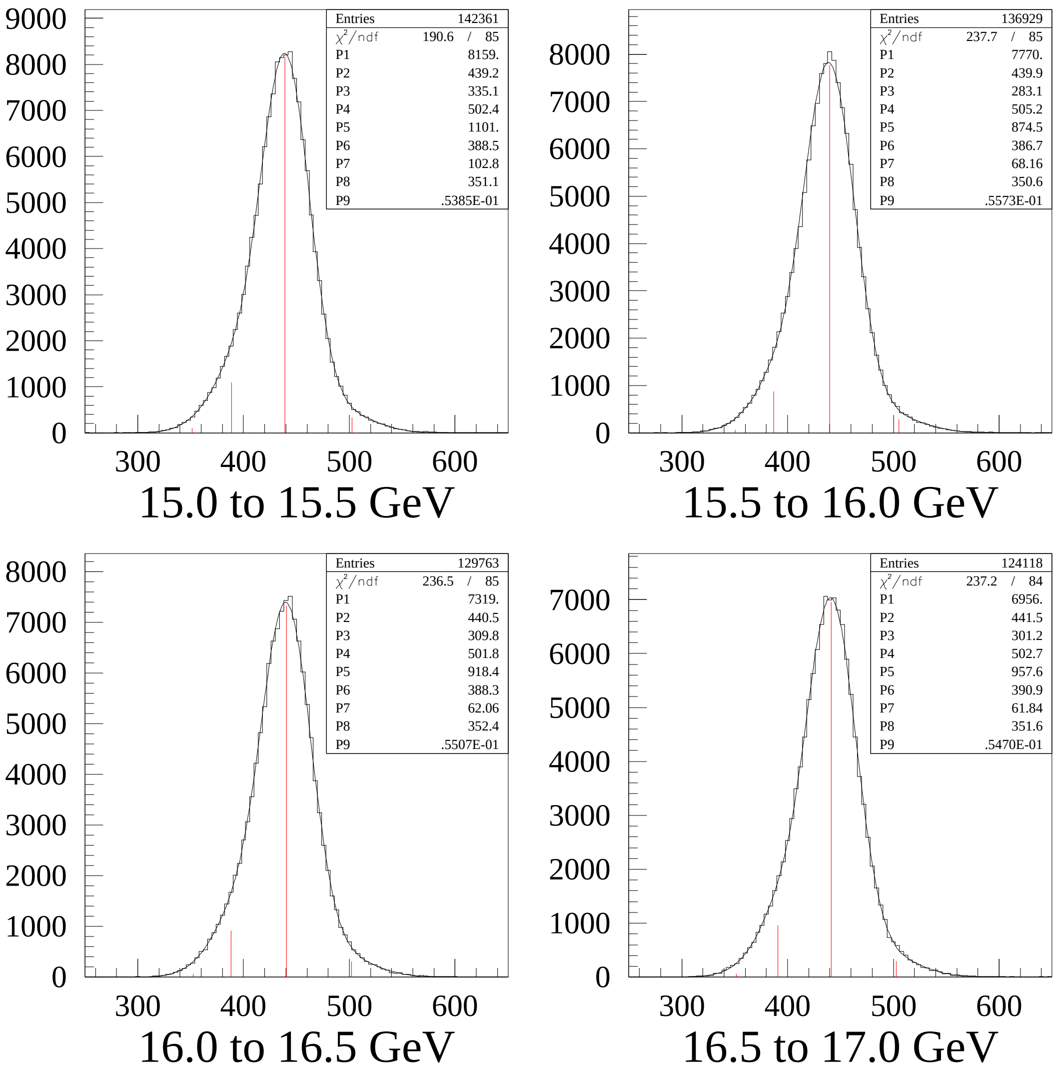

Run 808-820, 40K events in MTR(h-)

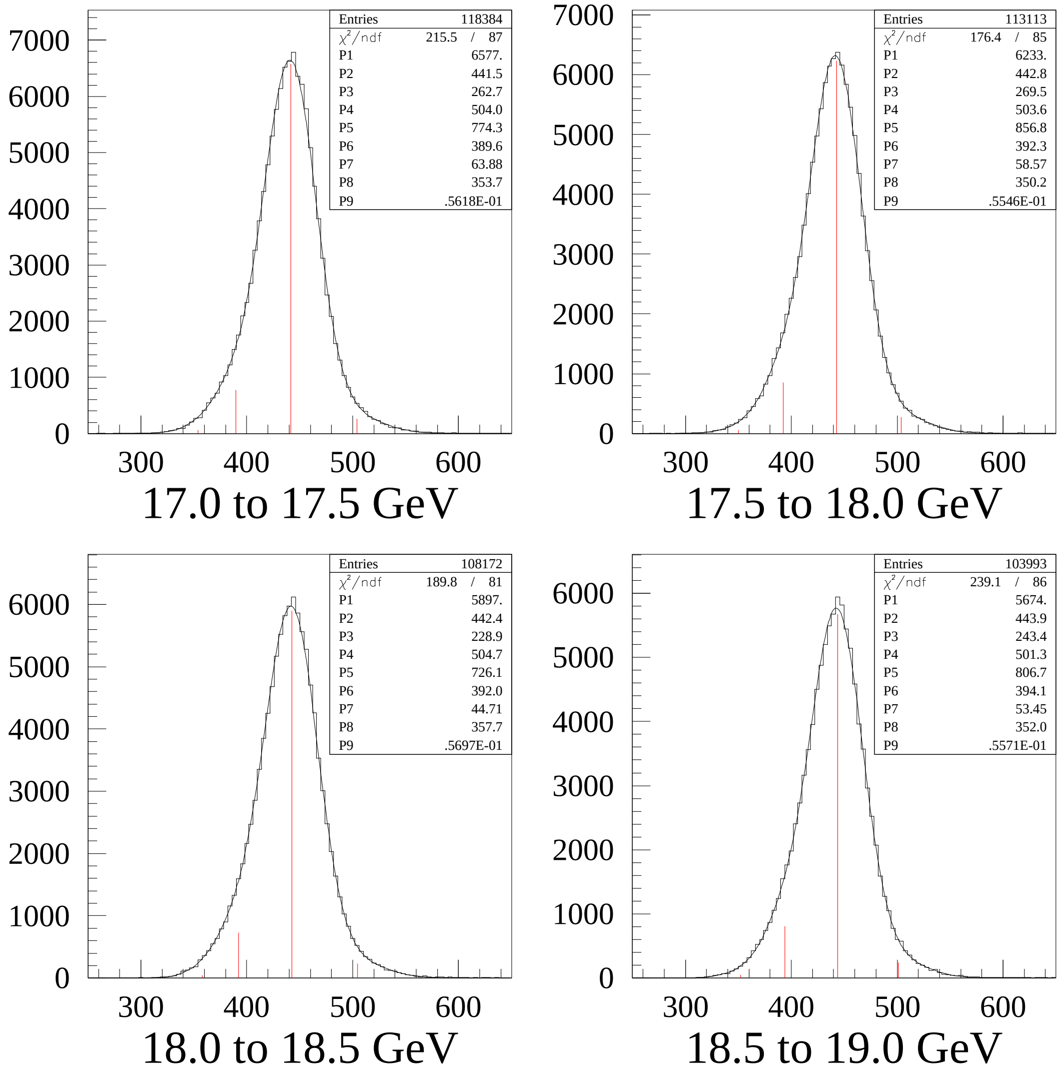

6.3.2 Results

Following the 4-gaussian fitting procedure the mean value, μ_i, for each particle species is obtained. The means for the π^-, K^- and e^- are then taken and plotted as a function of $\beta\gamma$, for all momentum bins below $\sim$ 20 GeV/c. Above this value the production of electrons and kaons is falling off and the fits become less reliable, and the information below 20 GeV/c is sufficient to map out all the features of the universal curve. The results of this procedure are seen in Fig. 6.3. The dE/dx data is normalized to the minimum of the ionization, I_0, as is common in the literature. All of the data points for the various species lie reasonably on the fitted universal parametrization curve except for the two systematic 'hooks' visible in both the pion and kaon points for lower momentum, from approximately 3-7 GeV/c. Since these hooks take place in both particle species in similar mometum ranges, it is likely that the behavior is due to some detector systematic in a certain localized geometric region of the MTPC. One possible cause is some remaining mismatching between the gains of different MTPC sector types(HR, SR, SR'). The sector correction procedure is intended to remove these mismatches but any time-dependent drift of the voltage inputs to these different sector types could cause such a systematic error.

For particle identification above momentum of 7 GeV/c, these systematics are not a problem. Since the K/p branch of the ionization curves are fully merged at 3 GeV/c, and do not achieve their full separation until 7 GeV/c, these systematics

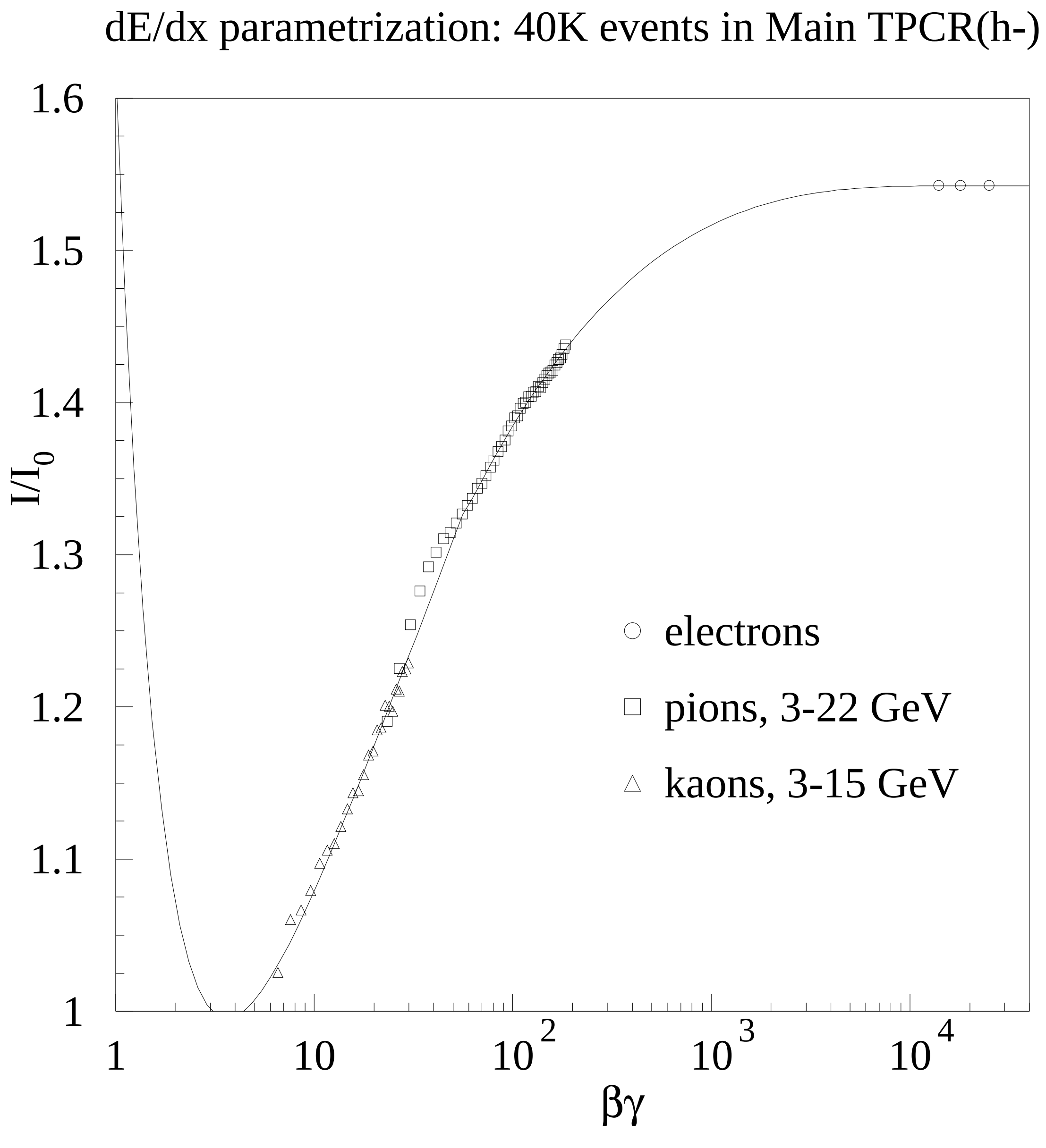

Figure 6.3: The parametrization of the relativistic rise showing pions, kaons and electrons in the extended momentum range from 3-22 GeV. The data is normalized to the minimum of the ionization, I_0. The same systematic S shape in the pion and kaon regions can be seen at low momentum.

are not a huge problem. 4 Gaussian fits become more and more difficult and impossible below about 5 GeV/c, because the K/p gaussians are too close together and completely unresolveable. The fit used to extract the final parametrization(used for determining the final spectra) only uses those data points above 7 GeV/c. This parametrization is shown in Fig. 6.4.

6.3.3 Resolution

The most important parameter in determining the resolving power of a detector to perform particle identification and separation is the dE/dx resolution, defined as

$$Resolution = \frac{\sigma(dE/dx)}{\langle dE/dx \rangle}.$$

Recall that the empirical Allison + Cobb prediction for the NA49 detector based on pressure, number of samples and sample size was about 4.5%. Typically detector systems reach resolution values which vary by about .5% above or below the Allison + Cobb predictions. The best resolutions achieved at NA49 fall within these general guidelines. A plot of the resolution as a function of momentum is shown in Fig. 6.5. At the lowest momentum the resolution is around 4.9%. This is a slight overestimate of the best resolution achieveable on a single pion peak alone, which is about 4.7%. This is an overestimation because the quoted resolution describes

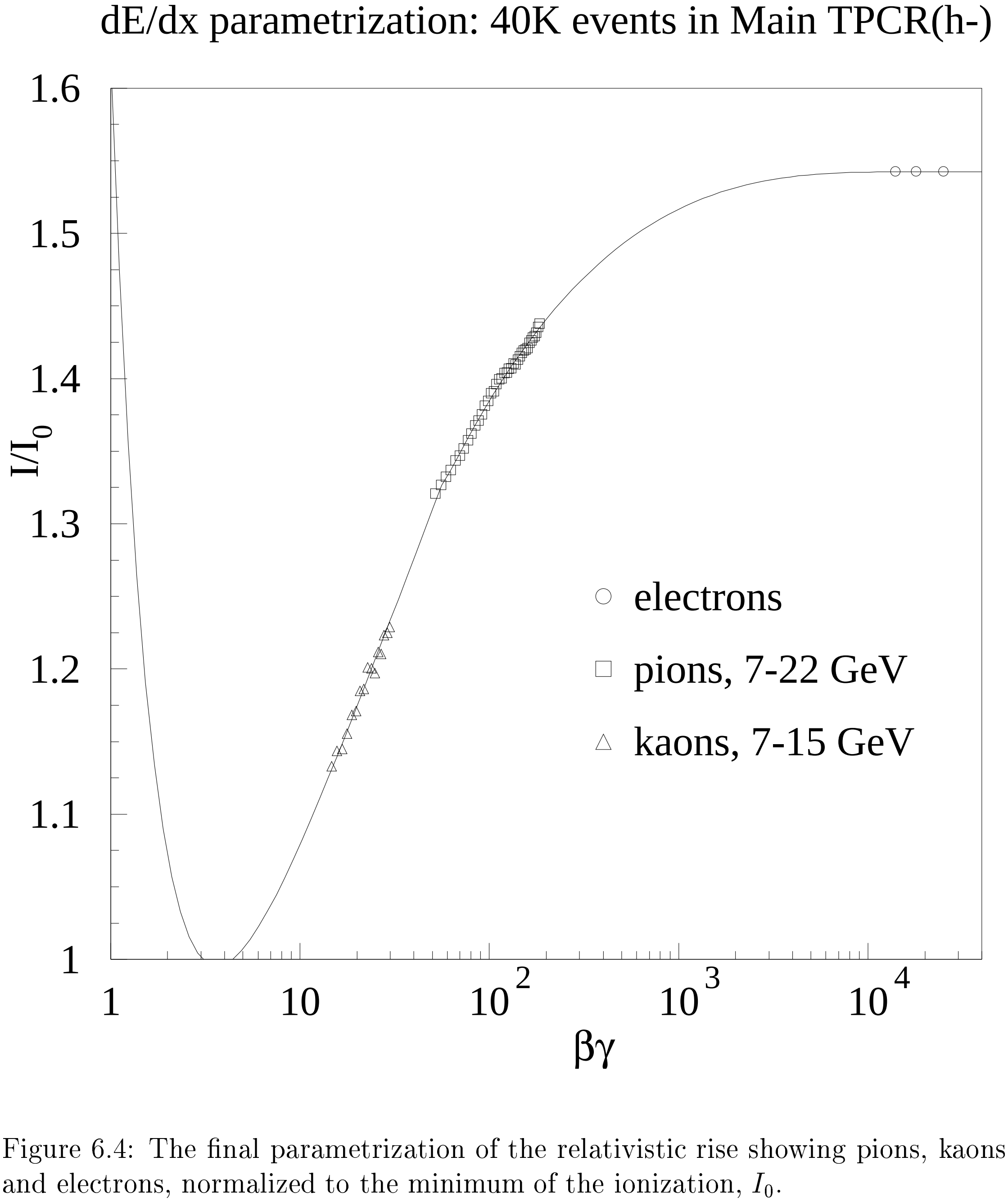

Figure 6.4: The final parametrization of the relativistic rise showing pions, kaons and electrons, normalized to the minimum of the ionization, I_0.

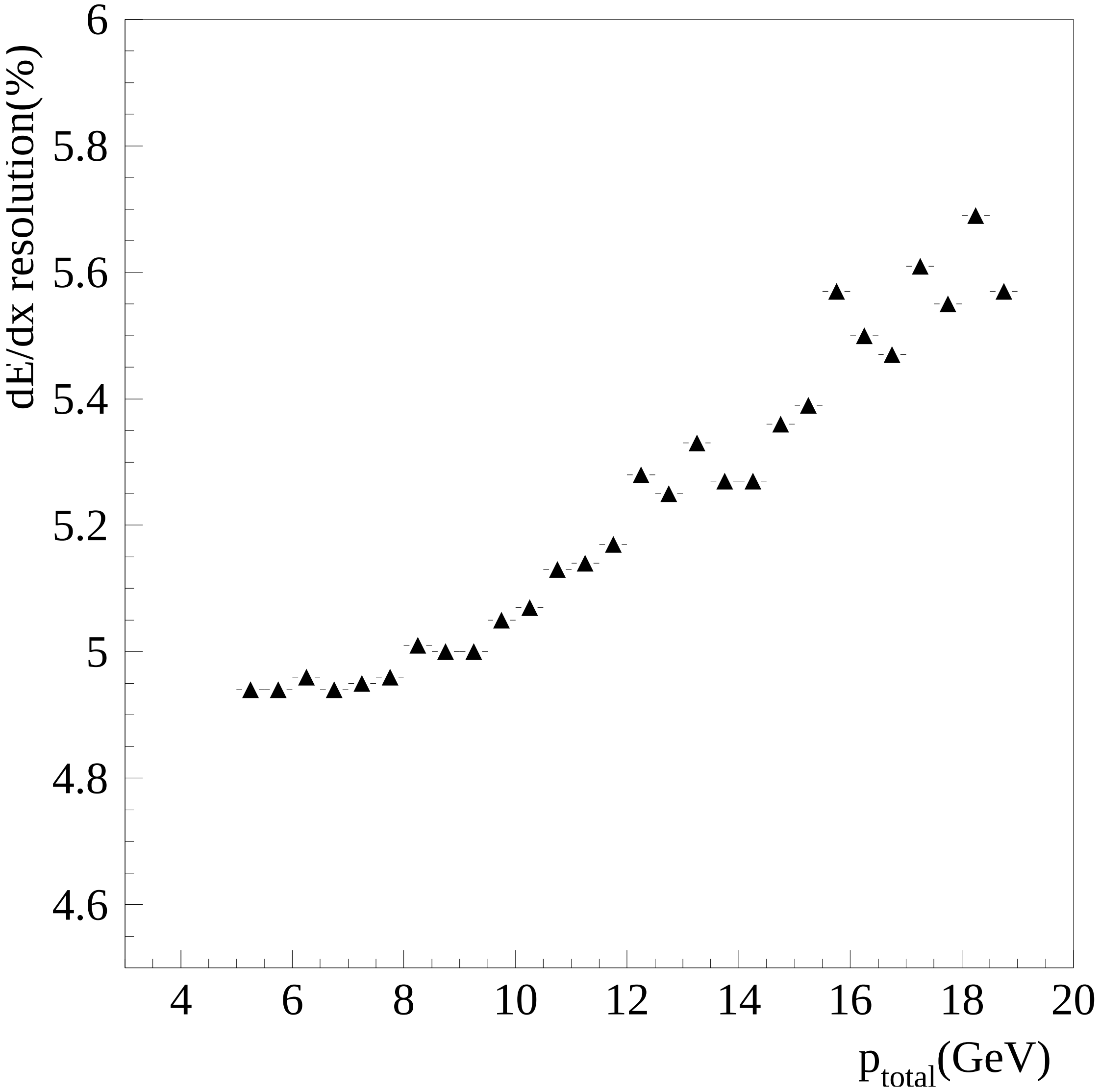

Figure 6.5: The resolution plotted as a function of momentum for negative hadrons(h-). The resolution increases as a function of momentum, beginning at around 4.9% and rising to 5.6% at around 20 GeV/c.

the best fit to one common resolution describing all the particle species. In reality the electron and kaon gaussians suffer more broadening from the tails of the large gaussian peak, and the electron peak itself is usually a little wider than the other peaks. This is probably due to the fact that hadronic scatterings off of various detector materials usually create electrons which do not actually come from the target vertex and so are slightly misidentified in momentum, but not causing them to vary substantially from the primary vertex and thus not be reconstructed by the momentum module.

The major problem with the dE/dx, is that the resolution rises strongly with momentum to about 5.6% at 20 GeV/c, as shown in Fig. 6.5. Recall that in the NA49 detectors, an increase in total momentum moves a particle's trajectory closer to the beamline. Thus an increase in momentum is correlated with an increase in particle density, as we move towards the untrackable 'pencil' region very close to the beamline. This is why the MTPC's have a central gap, because the average two-track separation in the pencil region is less than the two track resolution capabilities of the detector, which is around 1-2 cm. The probable cause of the increase in resolution as a function of momentum is due to cluster merging as we move to regions of higher particle density.

The NA49 TPC's tracking environment becomes increasingly dense as we move inward towards the SR and finally HR sectors. Merging of particle clusters becomes a serious concern, as a sizeable fraction of the ionization clusters are merged in either the time or pad direction. For dE/dx purposes, one would prefer to include none of these clusters in a calculation of the truncated mean, as they are less reliable. They are less reliable because of the present means of cluster splitting in the NA49 cluster finder. The NA49 cluster finder searches for clusters by looking for time samples of charge which are over threshold, as described in ∮ 3.2. If two neighboring clusters happen to be merged(are overlapping) in the time or pad direction, the charge is split by looking for a dip in the middle of the two clusters. The charge is split by cutting the two clusters at the dip and sending the charge to the cluster on either side of the dip. This is not the ideal method for accurate charge assignments, but the quickest from a software re-construction standpoint and from a simplicity standpoint. At present, alternative cluster-finders are being developed which attempt to do gaussian fits to either all clusters or a subset of the more problematic merged clusters which need more effective charge spliting for dE/dx purposes.

A quantitative understanding of the magnitude of the merging problem is given from the cluster quality information. All clusters have quality flags which include the following:

- CLS_MRG_TIME ⇒ clusters are merged in the time direction
- CLS_MRG_PAD ⇒ clusters are merged in the pad direction

Ideally all clusters which were flagged by the cluster finder in this way(having their charge information split as previously mentioned) would be thrown out. The problem is that they compromise to large a fraction of the actual clusters, which would lead to a degradation of resolution due to a lack of samples. For the most densely packed environment, the HR sectors of the MTPC, $\sim 20\%$ of the clusters are merged (including both time and pad merging) for h- in MTPCR, while $\sim 35\%$ of the clusters are merged for h+ in the MTPCR. The h+ merging is substantially worse because of the extra protons, whose high momentum puts them preferentially in the HR sectors. The merging is not as bad in the SR and SR' sectors where track densities are much lower. Such an effect could clearly be responsible for the observed resolution degradation as a function of momentum.

Chapter 7

Particle Identification via dE/dx

7.1 Data Set and Cuts

The data sets used for the analysis in this thesis are all from the November 1995 data runs at CERN. All analyzed data is from MTPCR only, avoiding systematics between MTPCR and MTPCL. The STD+ runs used, producing h- in MTPCR, are runs 808-820, containing $\sim$ 40,000 events. The STD- runs used, producing h+ in MTPCR, are runs 914-915, containing $\sim$ 25000 events. All of the data in these runs were taken with the NA49 'central' trigger. This trigger corresponds to the top 5% of the inelastic cross sections, or impact parameters $b \leq 4fm$.

A number of quality cuts were applied to the data, including the following:

- total momentum cut: $6 < p_{total}(GeV/c) < 60$

- truncated mean < 650 ADC counts

- vertex cut: $|b_y| < 10cm$

- n_max_point > 65 points (clusters)

The first cut on total momentum describes the effective range of the relativistic rise where $\pi/K/p$ separation can be performed via dE/dx. Below 6 GeV/c the kaon and proton ionization branches are strongly merging(completely merged by 3 GeV/c), making particle separation impossible in this regime. Above 60 GeV/c, a similar problem is encountered as all particles are rapidly approaching the Fermi plateau, where the $\pi/K/p$ branches again merge and make separation impossible.

The second cut on the truncated mean is used to remove the ionization signals of double or triple tracks. The average truncated mean in the chamber is around 400-500 counts, so trace amounts of doubly ionizing tracks exist around 1000 ADC counts. These are simply due to overlapping tracks which are too close to separate into two tracks. This cut has little practical effect on the analysis, as these large ionization values are only a tiny tail on the right side of the electron's gaussian distribution.

The vertex cut is required of every track which is successfully reconstructed by the momentum module. The vertex cut removes a majority of secondaries, which are created in interactions of primary tracks with materials or via decays. These tracks do not point back to the primary vertex and so are removed through this cut.

The final cut on the number of points is used to require tracks to have a large number of samples for good dE/dx resolution. The tracker itself requires a normal track to have 25 points, and this additional cut, specific to the dE/dx analysis, makes the point requirements more stringent. This cut disallows any tracks coming from the far right-side upstream corner of MTPCR from being considered, where tracks crossing the chamber cross less than 65 padrows, and therefore cannot have more than 65 samples. More than 90% of the tracks do have more than 65 found clusters, where the number of found clusters is defined to be n_point. However, even if the tracks have the possibility of having greater than 65 found points, not all tracks have this many due to statistical fluctuations along the track. Ideally, one would cut on the actual number of points on the track, n_point. The reason n_point was not used is there is no way to realistically connect to the Monte Carlo data used in the acceptance and efficiency corrections. The MTPC simulator used in the efficiency corrections does not correctly predict the observed distribution of points, making a cut on this variable impossible. However the n_max_point distribution, defined as the maximum number of points a track could have, agrees very well with the Monte Carlo point distribution, making cuts in the two regimes comparable and thus practical. N_max_point is 90 for a track crossing every padrow, and is less for those at large angles covering a limited region of the MTPC.

7.2 Acceptance

The NA49 MTPC's were designed to complement each other with respect to trying to measure the full phase space of particle production. If we consider pion production, The MTPC's window for pion acceptance(down to $p_T = 0$) begins at around $y \sim 4$. Mid-rapidity pions($y_{mid} \sim 3$), being so light, are bent out of the acceptance of the MTPC before they arrive. VTPC1 and VTPC2 are able to fill in the acceptance of these missing mid-rapidity pions, as they are positioned closer to the target.

The acceptance for negative pions in MTPCR is shown in Fig. 7.1. This acceptance plot includes the momentum cut $6 < p_{tot}(GeV/c) < 60$. The data between the sloped lines and to the right of the vertical line was used in the analysis. The data below the lower sloped line is lost due to the limited geometrical acceptance of MTPCR as well as the lower momentum cut. The data above the upper sloped line is lost due to the upper momentum cut, although very little is lost here as the high p_T production of pions at large rapidities is very small. p_T-y boxes with less than 80% acceptance were not used in the analysis due to the large systematic errors associated with extrapolating from limited acceptance.

The similar acceptance for positive pions in MTPCR is shown in Fig. 7.2. This acceptance plot includes a slightly more restricitive momentum cut, $6 < p_{tot}(GeV/c) < 50$. Above 50 GeV/c the fits to the h+ spectra are problematic and

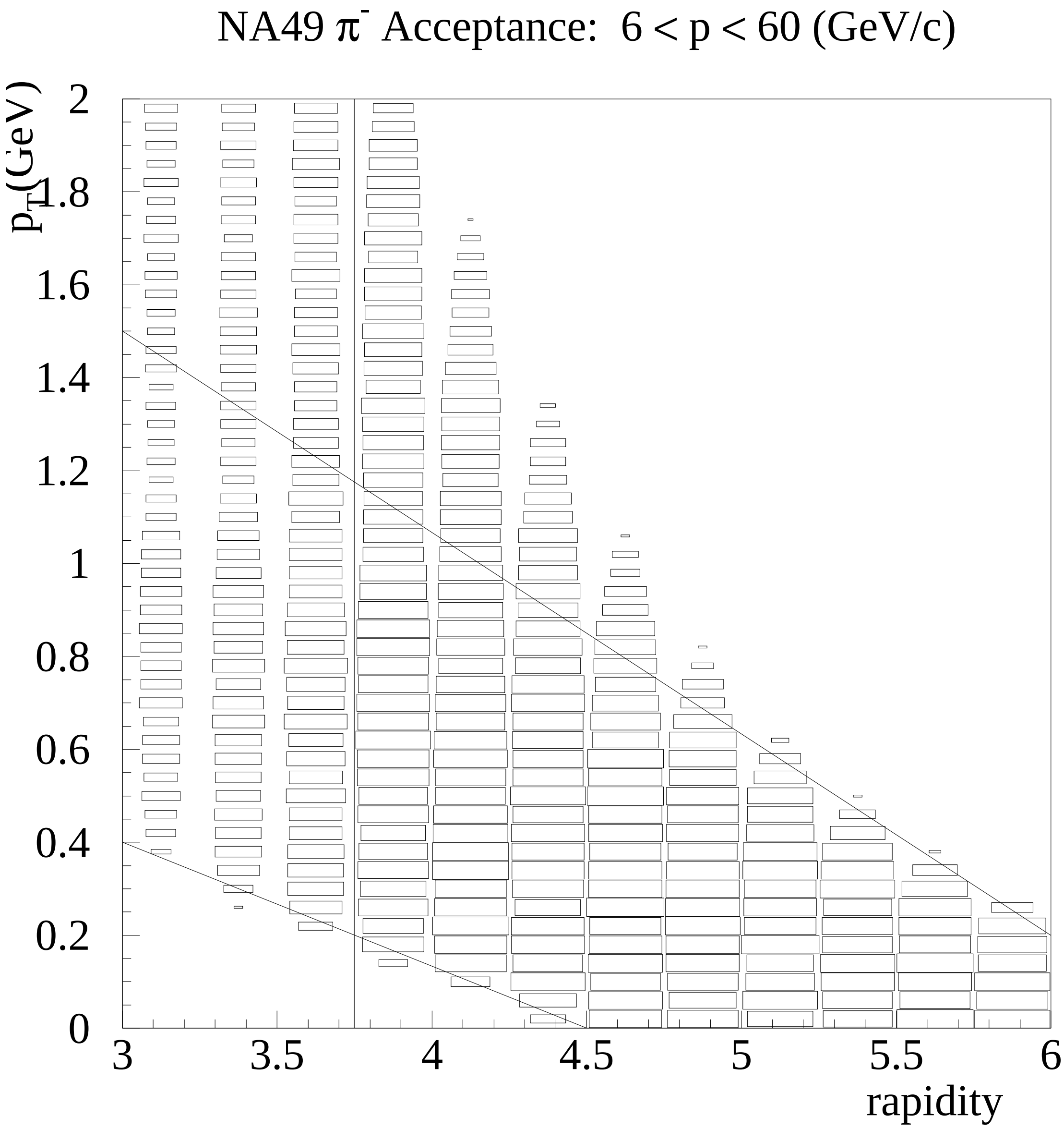

Figure 7.1: Acceptance for negative pions. Data between the sloped lines and to the right of the vertical line was used in the analysis.

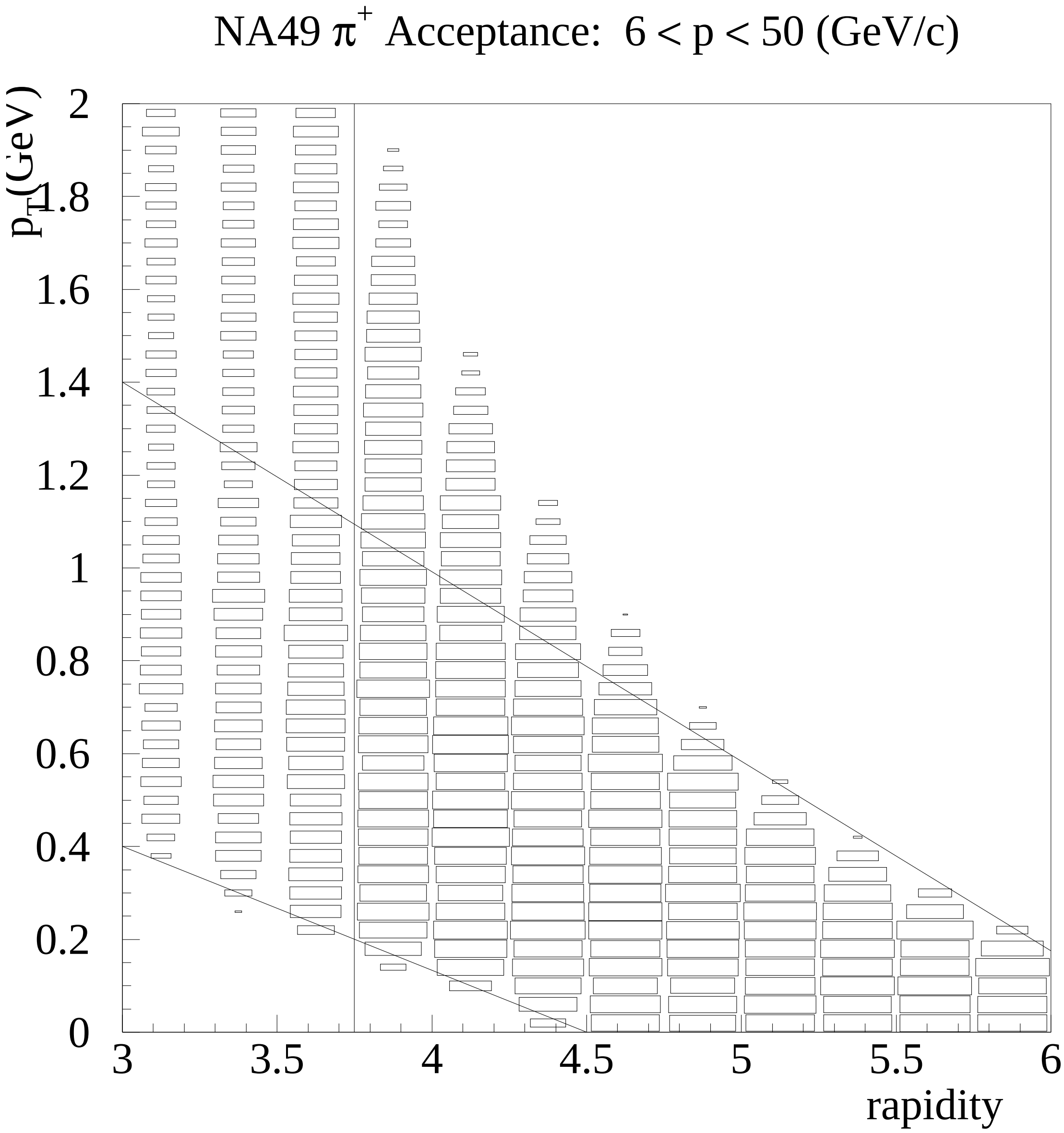

Figure 7.2: Acceptance for positive pions. Data between the sloped lines and to the right of the vertical line was used in the analysis.

therefore were not used. This is due to the fact that the h+ spectra are dominated by protons, which are very close to the kaon branch, and have the worst resolution since they are almost exclusively in the HR sectors at these momenta. This slightly more restrictive cut has little impact on the overall acceptance, only removing a small portion of the high p_T acceptance.

7.3 Statistical Deconvolution Procedure

The parametrization derived from the data is used in the deconvolution of the dE/dx spectra, which yields single-particle identified spectra on a statistical basis. The parametrization provides the most probable values, μ_i for the four particle species as a function of momentum. These 4 μ_i are used to reduce the number of degrees of freedom in the final fit to the data from 9 to 5. So with the fixed μ_i the free parameters for the final fit are 4 heights or yields(C_i's of the gaussian peaks at the central value and one common percentage width(σ_i for the four particle species. The five parameter fit to a superposition of four gaussians is again performed, with a functional form

$$F(dE/dx, p, C_i, \sigma_i) = \sum_i C_i \cdot exp\left(-\frac{(dE/dx - \mu_i)^2}{2\sigma_i^2}\right) with \;\; i = e^-, \pi^-, K^-, \overline{p} \;\; ,$$

where the μ_i are now fixed. The fits are performed in 0.5 GeV/c momentum bins over the full range of the acceptance. Examples of these final fits in a given momentum bin for both h- and h+ are shown in Figs. 7.3 and 7.4.

The results of these 5 parameter final fits to the data provide a function describing the dE/dx spectra for each momentum bin. These functions provide the heights of the 4 gaussian fit for any track with a given dE/dx and momentum. At this point the statistical deconvolution of the spectra can be extracted. For each track the probability of the track being a pion(or kaon, proton or electron) is given by

$$prob(\pi) = \frac{h(\pi)}{h(\pi) + h(K) + h(p) + h(e)} \quad ,$$

where the h's are the gaussian heights of each particle species at the given dE/dx and momentum value. The denominator represents the sum of the gaussian heights(or yields) of each particle species and is therefore equivalent to the value of the function(which is the superposition of 4 gaussians) at the given dE/dx and momenta value of the track in question. These fractional probabilities are then summed and binned into either rapidity, p_T, or m_T histograms for each particle type and represent the final(uncorrected) spectra. These final uncorrected spectra need to be corrected for acceptance and efficiency losses, which will be discussed in $\oint$ 7.7 and $\oint$ 7.8.

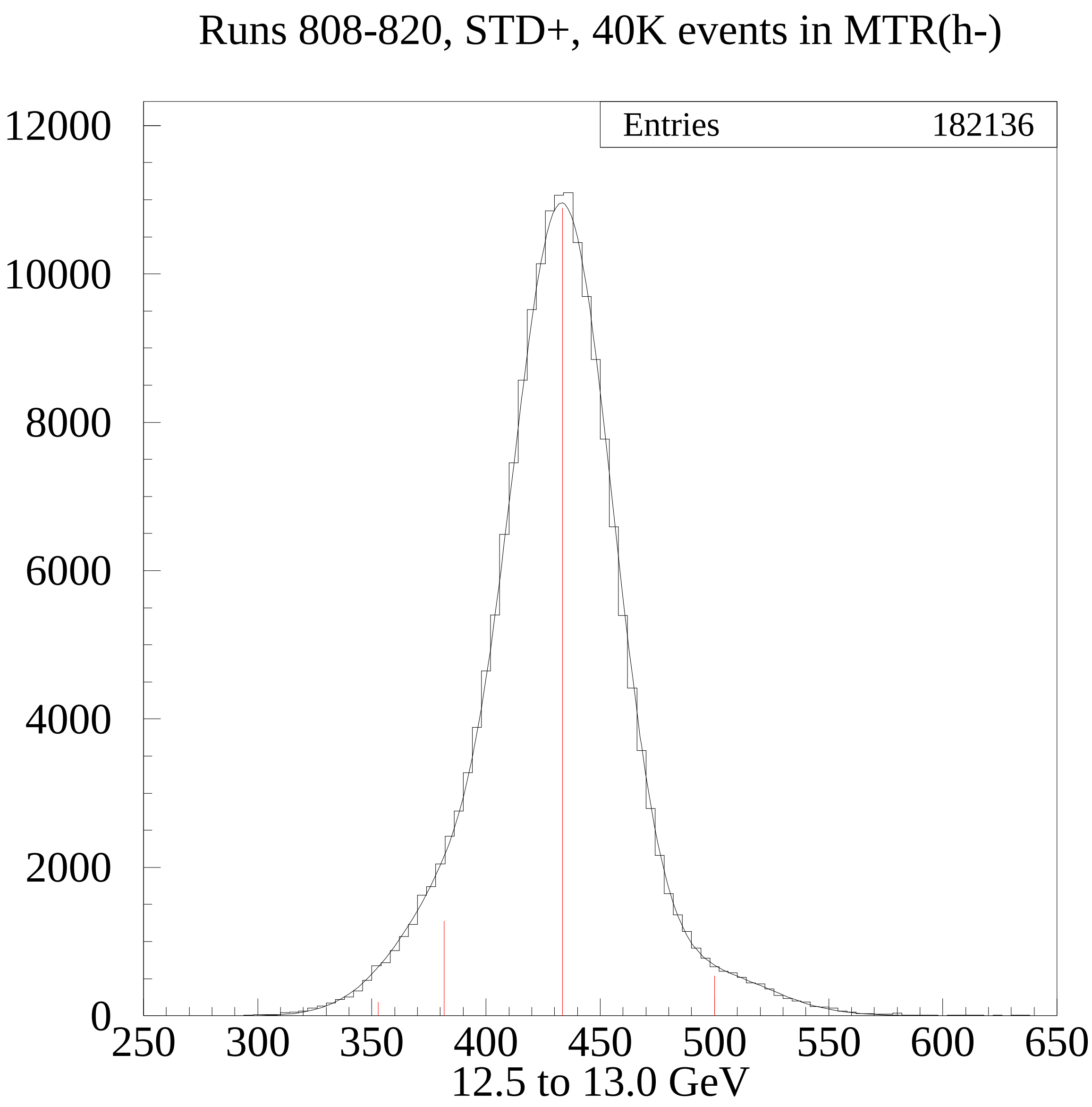

Figure 7.3: The final 5 parameter fit to the superposition of four gaussians for the 4 particle species, $e^-, \pi^-, K^-, \overline{p}$. Shown here is h- data in the momentum range $12.5 < p(GeV/c) < 13.0$.

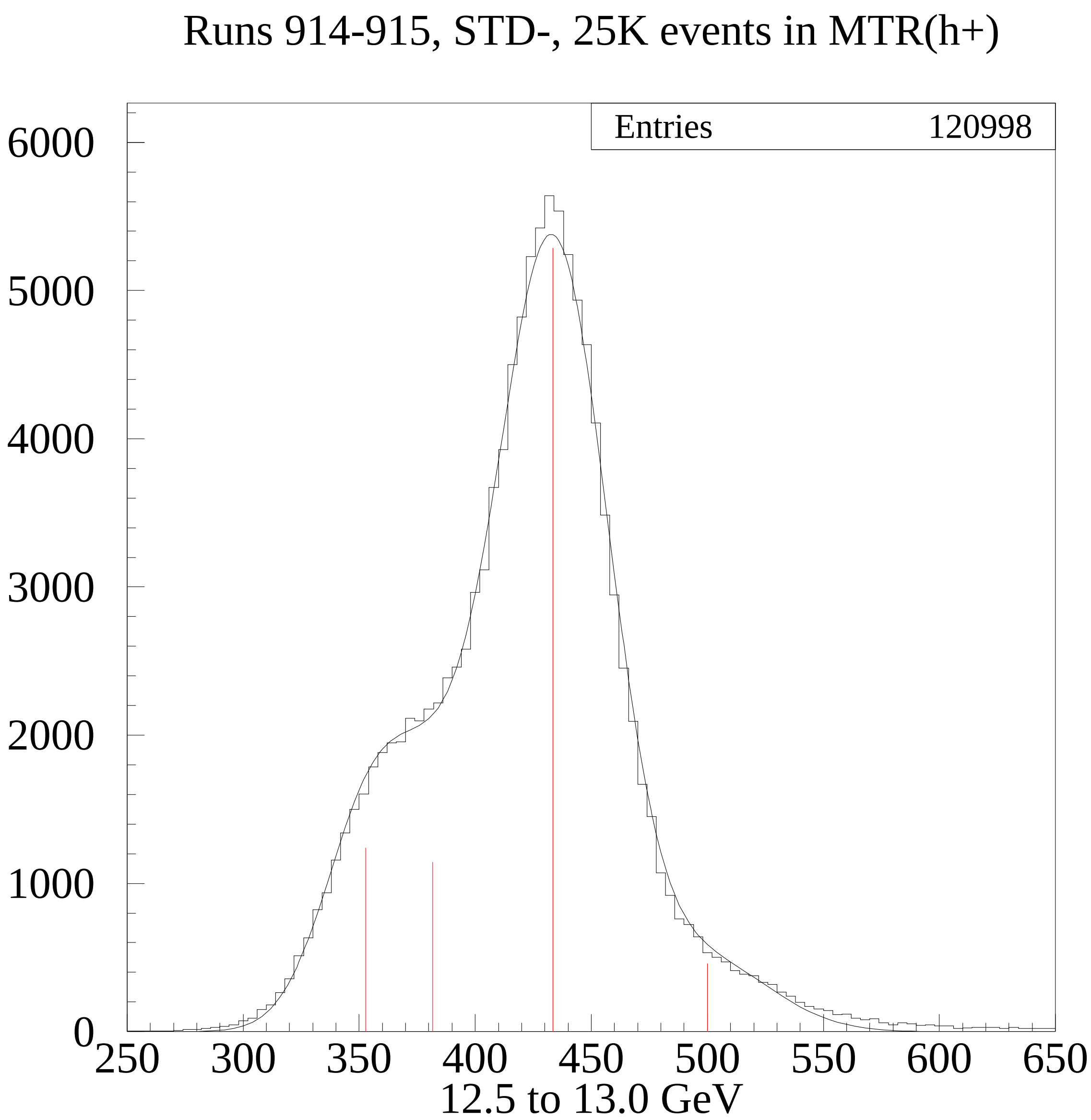

Figure 7.4: The final 5 parameter fit to the superposition of four gaussians for the 4 particle species, e^+, π^+, K^+, p^+. Shown here is h+ data in the momentum range $12.5 < p(GeV/c) < 13.0$.

7.4 Systematic Error from Parametrization

The primary source of systematic errors in the statistical dE/dx convolution procedure comes from the error in the parametrization. In order to quantize this systematic error, the four most probable energy values(the μ_i's), are varied in the final fitting procedure. Recall that these μ_i's are given by the parametrization. The μ_i's are varied by an amount equivalent to the error in the fitted values of the parametrization, and the subsequent variation in the final particle yields are determined. The final particle yields are dependent upon the height of the gaussian at the mean value and the sigma of the gaussian according to

$$N_i = \sqrt{2\pi} \cdot C_i \cdot \sigma_i \quad ,$$

where N_i is the total number of particles for each species, C_i is the guassian height or yield at the mean value μ_i, and σ_i is the width of the gaussian distribution for each species. Thus errors in both the heights and widths determine the final error in the yield.

The variation of the height(yield) of the various particle species at the mean dE/dx value is shown in Fig. 7.5. The data is for h- particles in the 10 GeV/c momentum bin. The mean value of each particle species is varied by $\pm$ 2%, which is equal to the error in the parametrization. The variation of the height varies for the different particle species, and is most extreme for electrons and anti-protons.

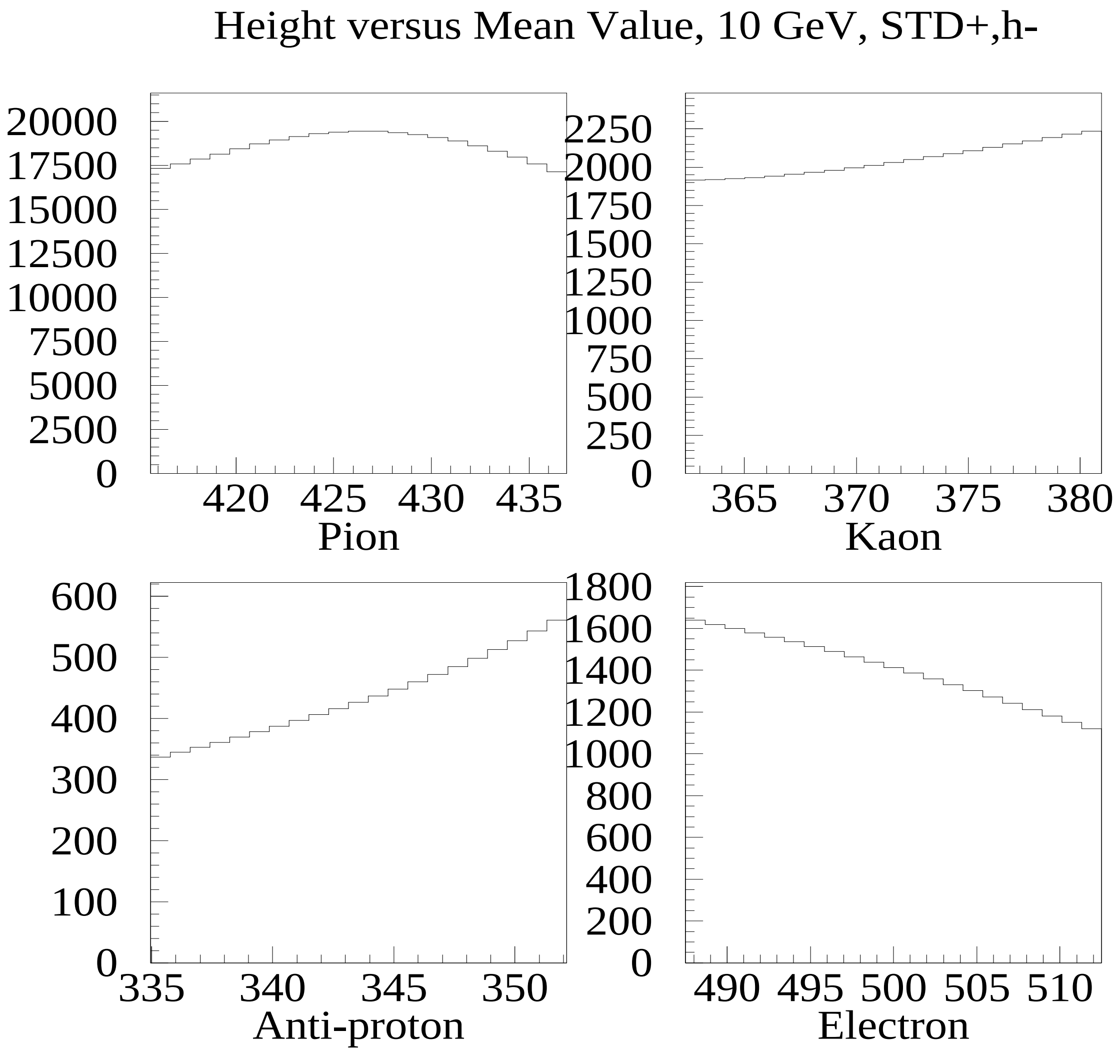

Figure 7.5: The variation in the height(yield) of the various particle species at the mean dE/dx value in the 10 GeV/c momentum bin. The mean value(μ_i) of each particle species is varied by $\pm$ 2%, which is equal to the error in the parametrization which yields the μ_i's used in the analysis.

Table 7.1: Systematic error(δ_i's) in the total particle yields due to the error in the parametrization. The error in the parametrization gives a $\pm$ 2% error in the mean values of the dE/dx(μ_i) for each particle species, which gives rise to the systematic error.

δ_π	δ_K	δ_e	$\delta_{\overline{p}}$
7%	7%	11%	22%

This result stems from these gaussians being at the far right and left of the 4 gaussian superposition. The shapes of these distributions make intuitive sense; the large central pion peak loses yield if we move off the mean value, as yield will be given to the kaon and electron gaussians on either side of the pion peak. Because the anti-proton and electrons are at the edges of the 4-gaussian superposition, they do not display a maximum like the pions. If we vary the anti-proton mean value, it gains yield from the kaon peak as the mean value moves towards the right and continuously loses yield as the mean value moves left towards nothing. The inverse behavior takes place for the electrons, as expected.

The subsequent variation of the widths for each particle species is shown in Fig. 7.6. This variation is combined with the height information to give the final variation in the total particle yield in Fig. 7.7. The systematic error in the final total particle yield is species dependent, being more severe for the anti-protons due

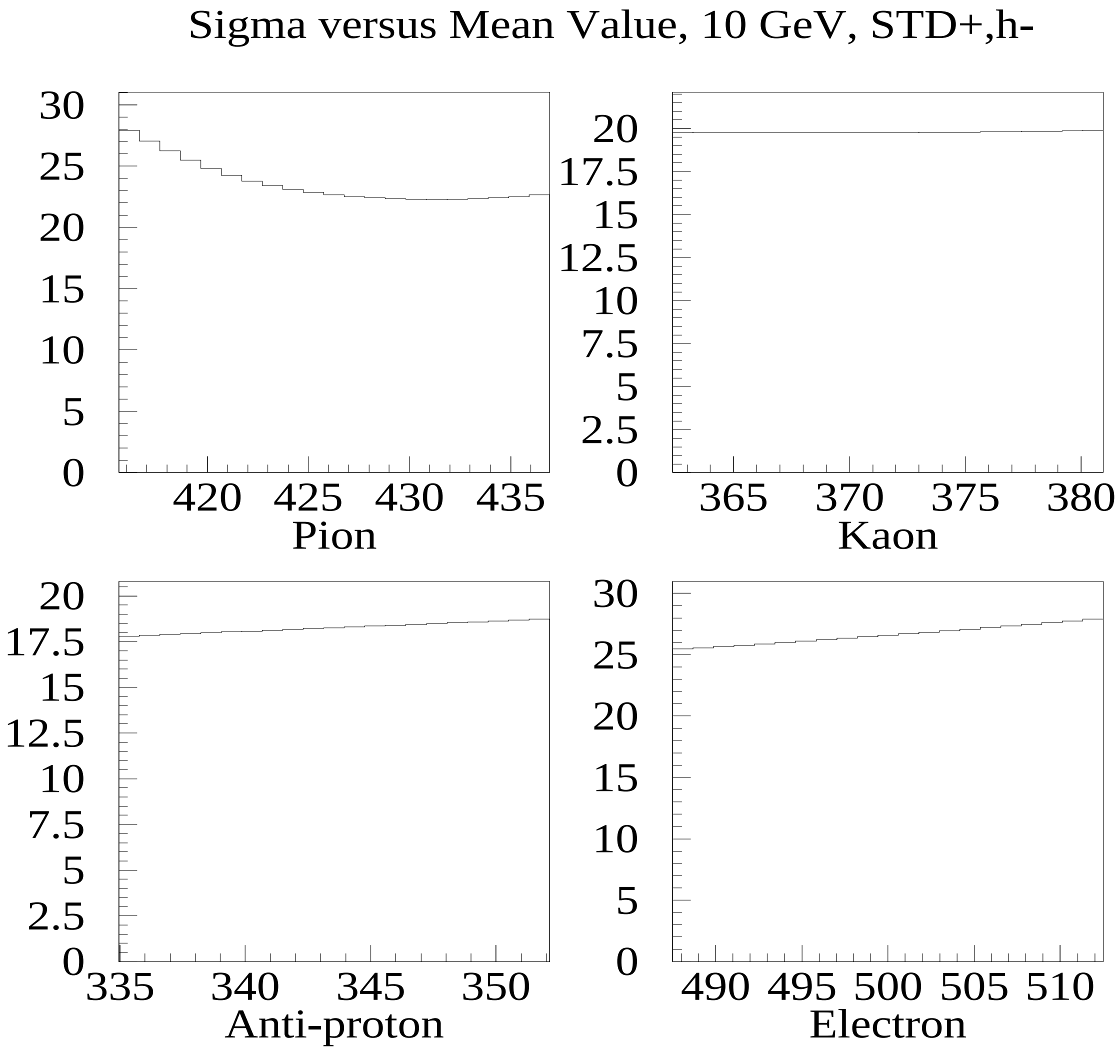

Figure 7.6: The variation in the width of the various particle species at the mean dE/dx value in the 10 GeV/c momentum bin. The mean value(μ_i) of each particle species is varied by $\pm$ 2%, which is equal to the error in the parametrization.

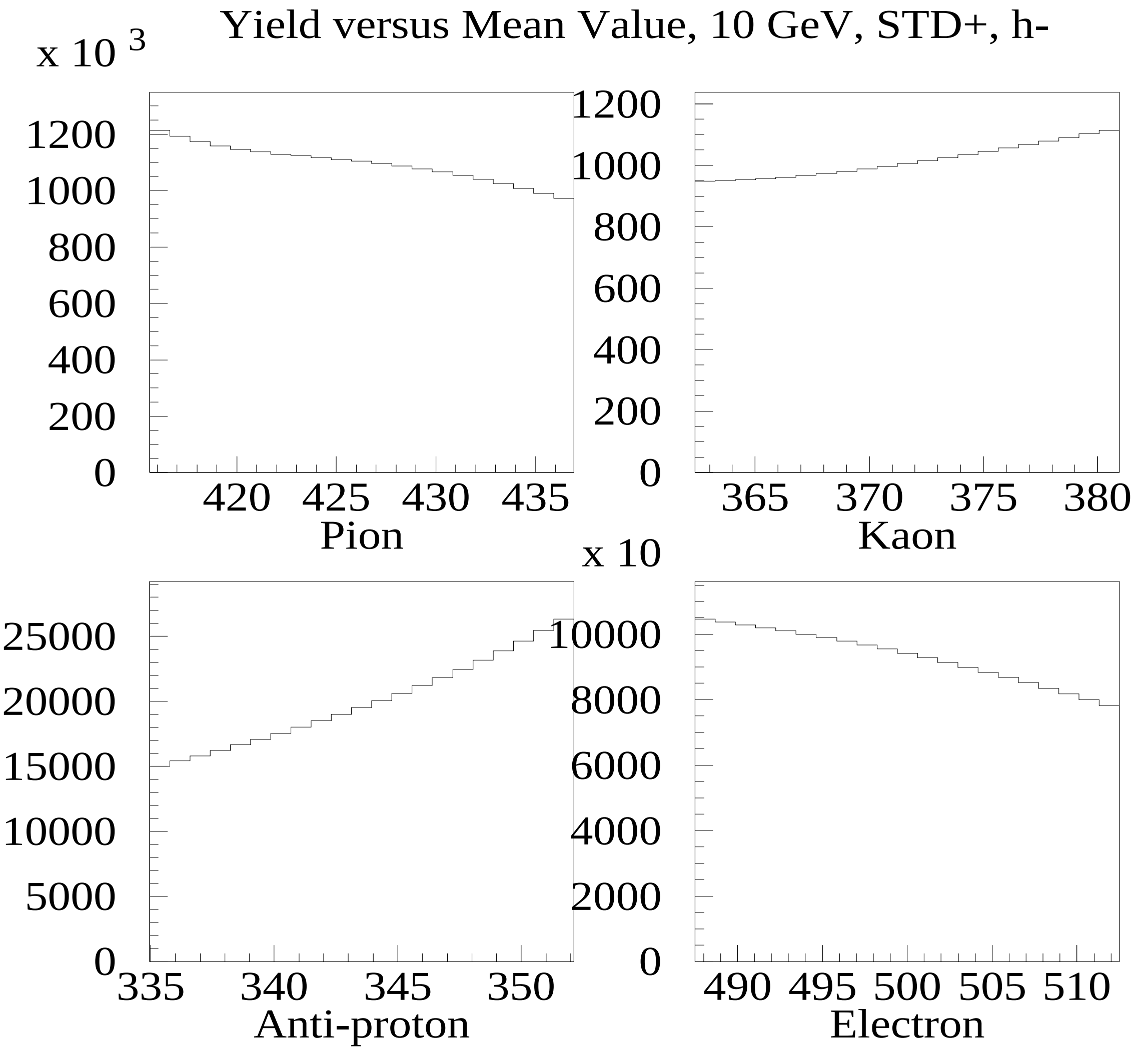

Figure 7.7: The variation in the yield of the various particle species at the mean dE/dx value in the 10 GeV/c momentum bin. The mean value(μ_i) of each particle species is varied by $\pm$ 2%, which is equal to the error in the parametrization.

to tiny production rate. The systematic error in the pions, kaons and electrons is similar, at around 10%. The final systematic error is shown in Table 6.1.

7.5 Introduction to Spectra Corrections

The initial $y - p_T$ distributions of charged pions that are generated by the statistical deconvolution of the dE/dx spectra must be corrected for a number of effects. The data must be corrected for the acceptance of the detector, components of which are a limited geometrical acceptance of the detector, lost acceptance due to kinematic cuts, and acceptance lost to particle decays. The data must also be corrected for the efficiency of the NA49 track reconstruction program, MTRAC. Every actual track which passes through the detector volume will not be accurately reconstructed, and so must be corrected for. These acceptance and efficiency corrections are generated in $y - p_T$ bins(to be discussed), and then on a bin-by-bin basis the product of these two fractional correction factors are applied to the data. This procedure yields the final spectra:

$$N_{final} = N_{measured} \cdot \frac{1}{acceptance} \cdot \frac{1}{efficiency},$$

where the N's are the number of produced particles in each $y - p_T$ bin.

7.6 Monte Carlo Simulations

There are several steps necessary to perform either the acceptance or efficiency corrections, both of which require several computer simulations to help model what is happening in the actual physical systems, generically called Monte Carlo simulations. The tools which are necessary to adequately simulate a real event include:

- event generation capability
- detector simulation
- TPC response simulation

The first requirement is an event generation package, which produces a fictitious set of tracks(including particle types, trajectories, momenta etc...) which are representative of an actual NA49 central Pb+Pb event, or which are appropriate for some correction task. Two types of event generation packages are used for this analysis. The first is to generate a simple 'flat-phase space' particle distribution, where tracks of one particle species are produced in a homogeneous fashion, equally spaced to fill up a certain $y - p_T$ space. These flat-phase space distributions are used for the acceptance corrections.

The second, more realistic type of event generation is performed using the VENUS package[Wern87]. VENUS is a microscopic 'string' model which describes particle production in relativistic heavy-ion collisions via the formation and fragmentation of color strings among the partons in the projectile and target nucleons. The output of a VENUS simulation is a set of particles with kinematic values which fairly accurately describe the observed particle production rates over a range of different energies and target-projectile systems. Since the efficiency corrections need a track distribution which closely resembles the actual particle production in the NA49 MTPC's, VENUS is used for this correction.

The next simulation package that is needed is one which realistically simulates the passage of elementary particles through matter, specifically the matter of the NA49 detector environment. This is performed using the GEANT package[Gean94], which is a powerful general simulation package which can be used to simulate any detector configuration. GNA49[Jaco93] is the specific simulation package which has been developed to describe the NA49 configuration. In the GEANT simulation each piece of the active detector system is modeled as a superposition of simple geometrical volumes of gas or solid, of a given material type. GEANT is able to simulate the passage of a particle through each of these geometrical volumes, taking into account all normal physical processes such as energy loss, Coulomb scattering, nuclear scattering and so forth. The output of GEANT is a record of the trajectories of the input particles(flat-phase space or VENUS here) through the detector volumes, as well as the energy deposition in each volume, recorded as an idealized set of space points. These GEANT space points are positioned over the center of the individual pads in the padrows of the MTPC.

The final Monte Carlo tool needed to do spectral corrections is a program which simulates the TPC response to the energy deposition contained in the existing Geant space points. Each Geant hit is the seed for the creation of a charge cluster. The MTPC simulator, MTSIM[Toy94], models the formation and transportation of a charge cluster to the pad plane and the subsequent generation of a signal by the readout electronics. Built into the simulator are most of the key ingredients of electron drift and detection, including the pad response function, shaper width, sense wire geometry, diffusion constants, and drift velocity of the gas.

7.7 Acceptance Corrections

Acceptance corrections are necessary due to the finite geometry of most detectors; it is rare that a detector's geometric coverage contains the full phase space(y-p_T) production of a given particle. Thus the acceptance must be simulated in order to understand what the acceptance is, as well as to correct for where the acceptance is incomplete. In this analysis the acceptance correction corrects for

- the limited geometrical coverage of MTPCR
- the additional loss of particles due to kinematic cuts in momentum and maximum number of track points
- particles that decay before they reach MTPCR(small effect for pions)

The acceptance correction is performed for pions using a flat phase-space production in the following range:

- $3 < y_\pi < 6$
- $0 < p_T(GeV/c) < 2.5$

These flat phase-space pions are then passed through the NA49 GEANT, GNA49. The kinematic cuts of $\oint$ 7.1 are imposed, and the pions are allowed to undergo hadronic scattering in the detector materials and decay. The scattering loss, as well as the decay of the pions into muons are both very small effects, of less than 1% each. The special design of the NA49 field cages to be nearly zero mass, combined with the helium bags in between detectors makes the amount of material in the flight path small, limiting multiple Coulomb scattering and hard hadronic scattering losses. The MTPC is about 12 m away from the target, so the long lifetime of the pion($c\tau = 7.8045m$), extended by its gamma boost, makes the pion decay rate small.

The acceptance correction factors are determined as a function of y and p_T. The rapidity bins are 0.25 units and the p_T bins are 50 MeV wide, both determined by the desired binning of the data for the final spectra. The correction factors are computed from the inverse of the ratio of all non-decaying tracks that are found in MTPCR after the momentum and point cuts, divided by the total number of initial tracks created. The distribution of generated flat phase-space negative

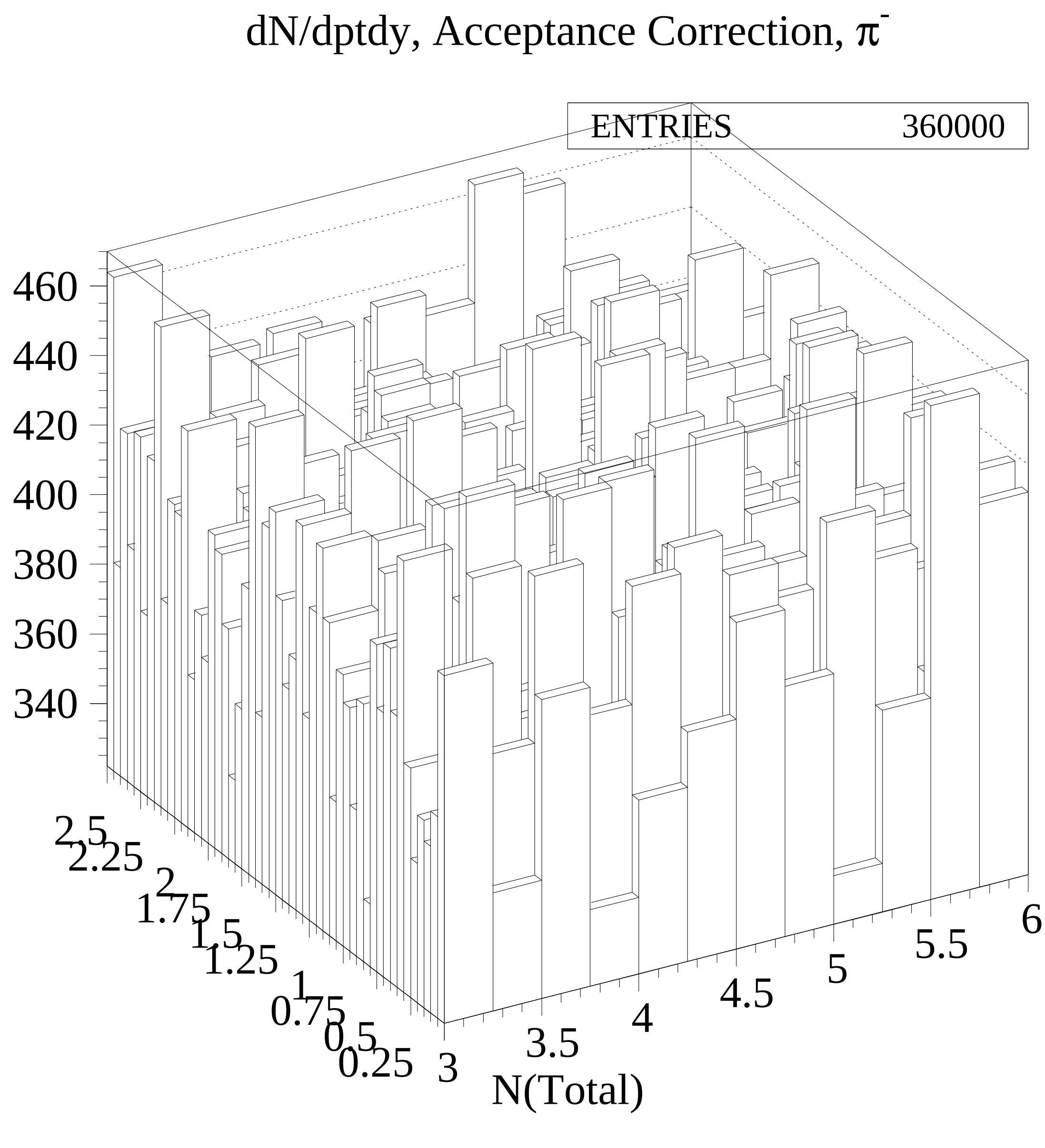

Figure 7.8: Acceptance correction plot for negative pions, showing the total initial distribution of flat phase-space tracks.

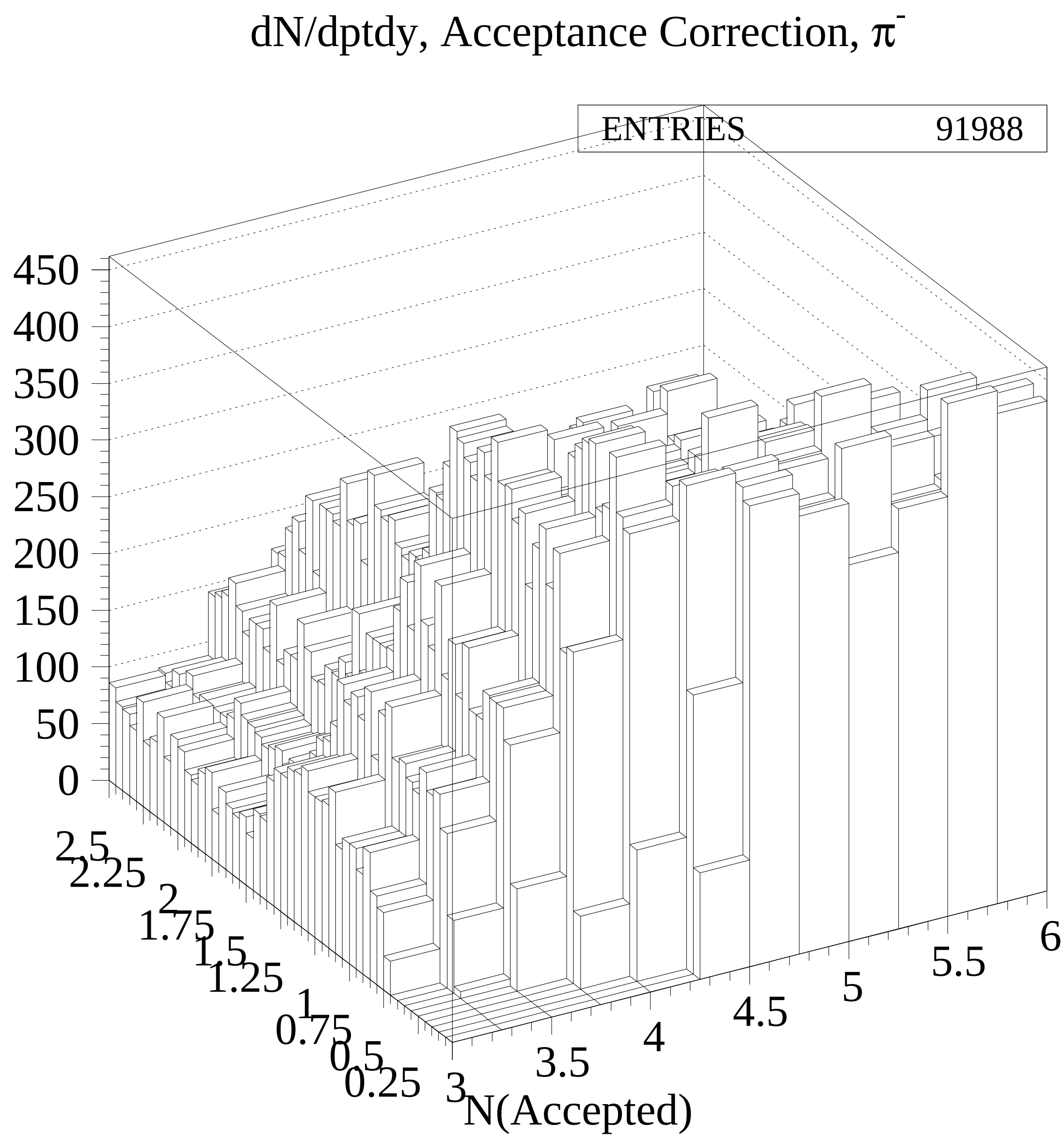

Figure 7.9: Acceptance correction plot for negative pions, showing the total number of tracks accepted into the geometrical acceptance of MTPCR after kinematic cuts and decays.

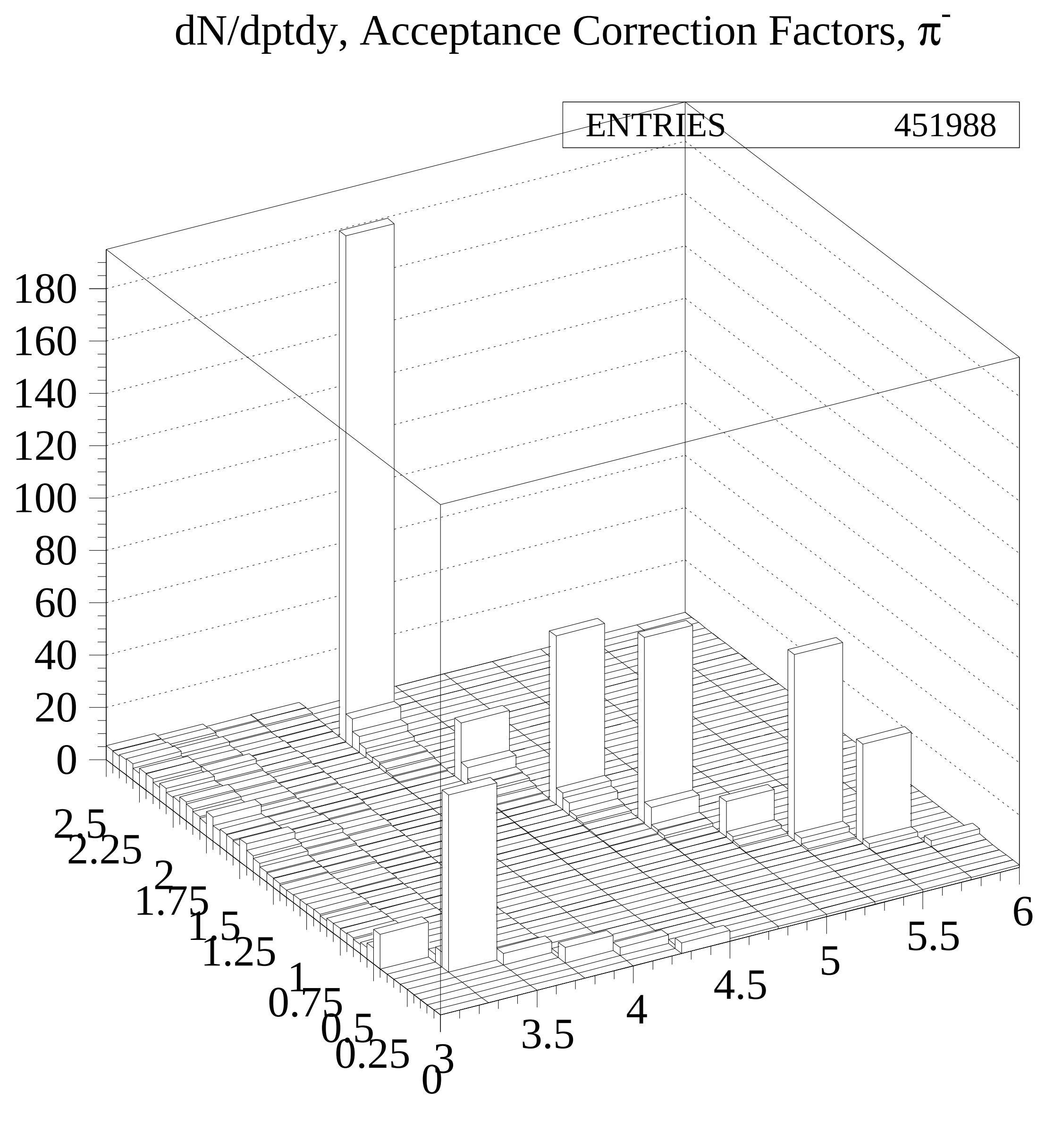

Figure 7.10: Acceptance correction plot for negative pions, showing the final acceptance correction factors.

pions is shown in Fig. 7.8, again with $3 < y_\pi < 6$ and $0 < p_T(GeV/c) < 2.5$. The total number of tracks that are accepted is shown in Fig. 7.9. As seen, for $y > 4.25$ there is full acceptance down to $p_T = 0$, which is crucial to measure the low p_T enhancement of the pion spectra due to resonance decays. The final acceptance correction factors are shown in Fig. 7.10. This plot mainly illustrates where the acceptance 'edges', or where the acceptance is quickly lost(correction factor becomes large). The correction factors away from these acceptance edges are all close to 1, being a bit larger only to account for particles lost in the gaps between sector types or decays.

7.8 Efficiency Corrections

Efficiency corrections are necessary in order to compensate for the fact that the tracking module, MTRAC, is imperfect and does not always successfully reconstruct every track which passes through the TPC. Although the tracker does an excellent job, reconstructing about 98% of the pions studied in this analysis, some tracks are lost due to 2-track resolution limitations and other systematics.

In order to perform tracking efficiency corrections, we need a simulated TPC environment which is as close to the actual event as possible. For acceptance calculation a simple flat phase-space distribution is fine, but to study efficiency we need a realistic track distribution and TPC response. Thus VENUS events are used, passed through GNA49, and finally through MTSIM to simulate the TPC response. Unlike in the acceptance corrections, a realistic TPC response is necessary to study the tracking efficiency. Two-track resolution losses are caused by diffusion, geometry, and electronics parameters, which must be included in the simulation.

The efficiency corrections are also determined as a function of y and p_T. The rapidity bins are .25 units of rapidity and the p_T bins are 50 MeV wide, both determined by the desired binning of the data for the final spectra. The efficiency correction factors are determined from the inverse of the ratio of all tracks that are successfully reconstructed by the tracking module, divided by the initial distribution of tracks which are accepted into the TPC with the dE/dx specific cuts. The distribution of generated VENUS negative pions which are accepted into MTPCR with the dE/dx specific cuts is shown in Fig. 7.11, again with $3 < y_\pi < 6$ and $0 < p_T(GeV/c) < 2.5$. The total number of tracks from this distribution that are then successfully reconstruced by the tracking module is shown in Fig. 7.12. As the total entries illustrates, the tracking efficiency is very good, as less than 2% of the tracks are lost due to tracking inefficiencies. The final efficiency correction factors are shown in Fig. 7.13.

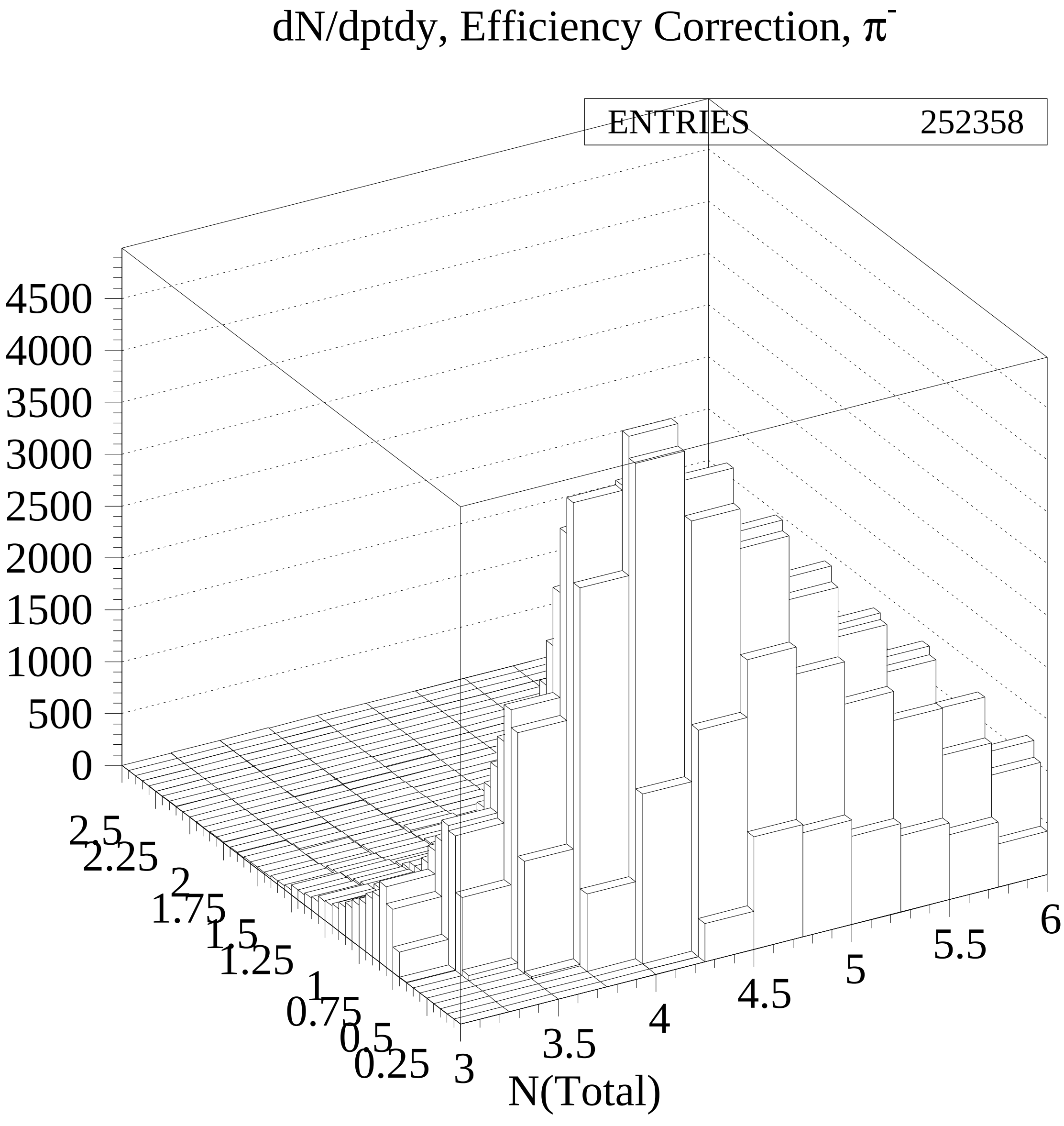

Figure 7.11: Efficiency correction plot for negative pions, showing the total initial distribution of accepted VENUS tracks.

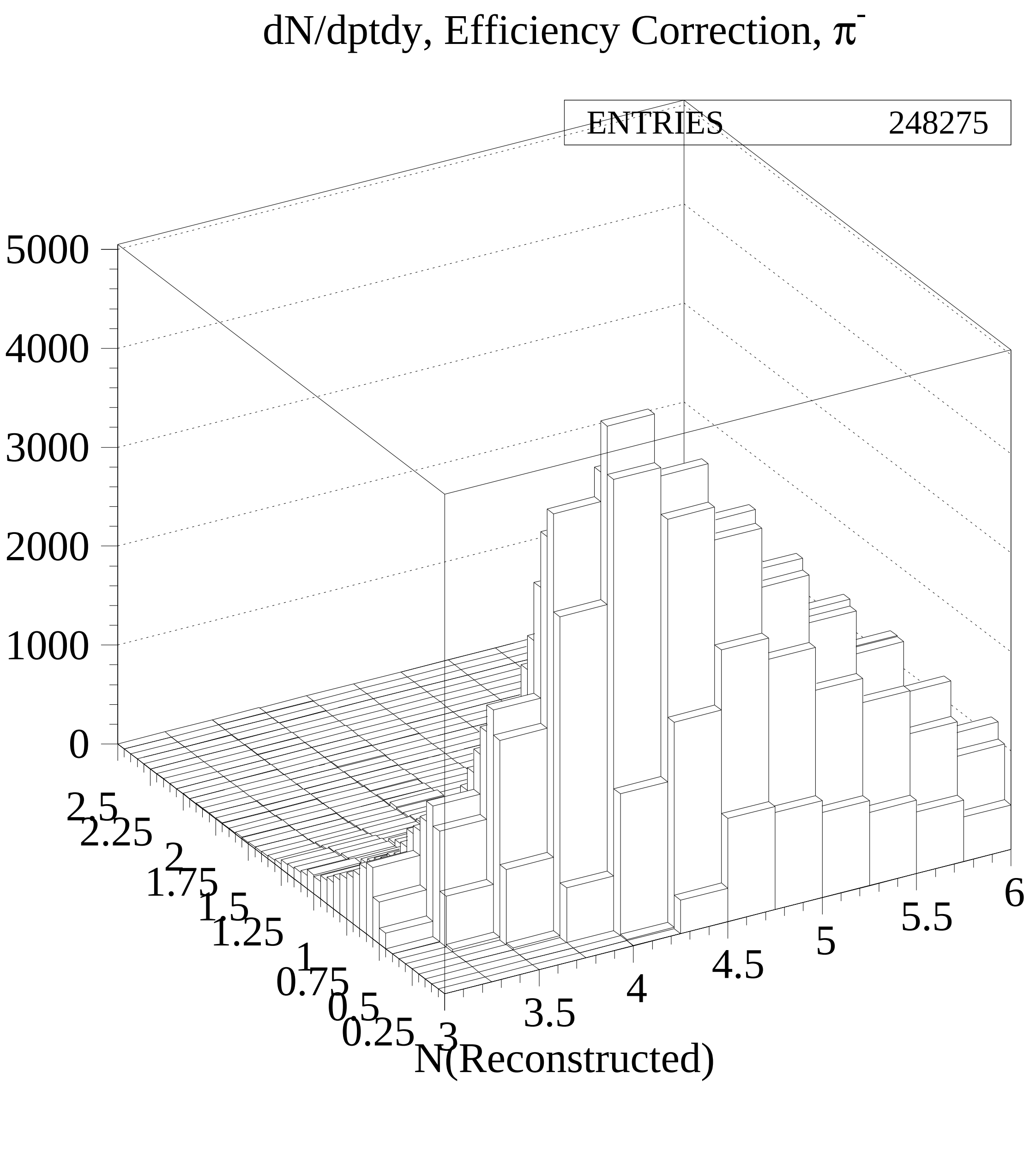

Figure 7.12: Efficiency correction plot for negative pions, showing the final distribution of accepted VENUS tracks which are also reconstructed successfully by the tracking module.

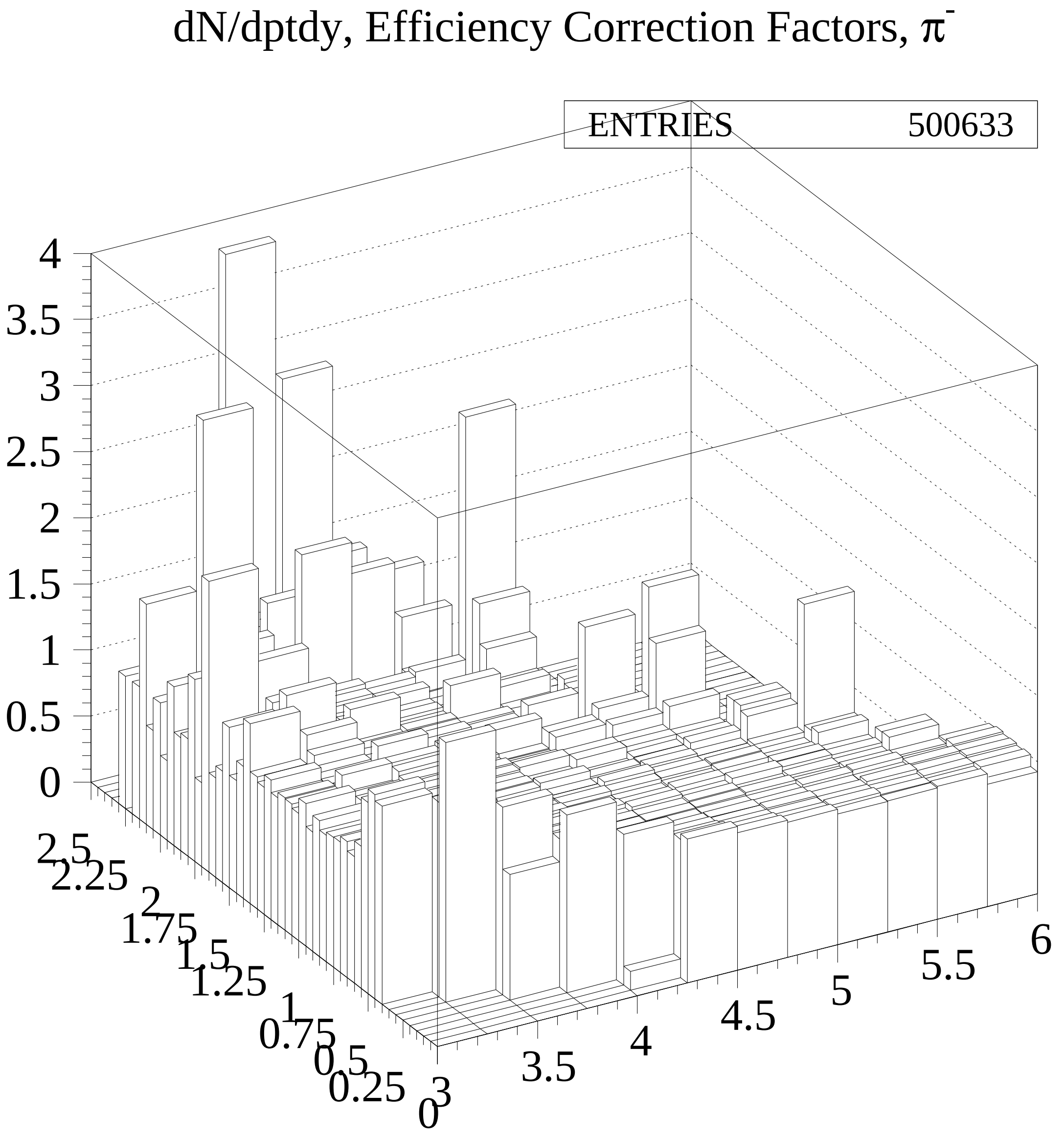

Figure 7.13: Efficiency correction plot for negative pions, showing the final efficiency correction factors.

Chapter 8

Results

8.1 Introduction

In the preceeding chapters, the dE/dx physics analysis was introduced. In addition to the several corrections performed on the raw dE/dx information, a global parametrization was developed to describe each particle's mean dE/dx value as a function of $\beta\gamma$, or equivalently momentum for a particle of a given mass. This parametrization was used to perform the final 4-gaussian fits to the data, from which the raw yields of pions can be extracted. These raw yields are then corrected for geometrical acceptance, hadronic scatterings, and decays, as well as for tracking inefficiencies. This chapter reviews the resulting spectra and phenomenon for positive and negative pions, and includes the following:

- transverse momentum(p_T) and transverse mass(m_T) distributions

- the resulting inverse slope parameters(effective temperatures, T)
- rapidity(y) distributions, and integrated yields
- the famous 'low-p_T excess' of pions
- the so-called 'Coulomb effect' of pions

The distributions of a particle species in rapidity and transverse momentum(or transverse mass) provide insight into the reaction dynamics as well as the mechanisms for particle production. The spectral analysis of pions is complicated by the deviation of the pions p_T spectra from a thermal spectrum at low p_T. This deviation is thought to result primarily from a large low-p_T enhancement of the pion spectra from resonance decays. The spectra are further distorted at the lowest p_T's by the Coulomb Effect, whereby the positive and negative pions are distorted differently by the large net positive charge of the stopped protons. This distortion is analagous to the spectral distortions of positive and negative beta decay from a positively charged nucleus, in which the positrons receive a kick away from the charge, while the electrons are sucked in towards the charge.

8.2 Pion Transverse Momentum Spectra

A thermal description and fit of single-particle spectra is motivated by the observed exponential shape of many hadron transverse momentum distributions[Jone96].

Under the assumption of a thermalized particle source with temperature T, which emits particles with mass m isotropically, the invariant transverse momemtum spectra is given by Hagedorn[Hage83] as:

$$\frac{1}{p_T}\frac{dN}{dp_T} = C(T) \cdot m_T \cdot K_1(\frac{m_T}{T}),$$

where C(T) is a constant, m_T is the transverse mass given by $m_T = \sqrt{p_T^2 + m^2}$, and K_1 is the modified Bessel function of order one. For $m_T \gg T$ this expression can be approximated by

$$\frac{1}{p_T}\frac{dN}{dp_T} = C(T) \cdot \sqrt{m_T} \cdot exp(-\frac{m_T}{T}).$$

The formula most commonly used for fits in the literature is an approximation of this expression where only the exponential portion is taken into account since it is the dominant factor. This leaves

$$\frac{1}{p_T}\frac{dN}{dp_T} = C(T) \cdot exp(-\frac{m_T}{T}).$$

This form is justifiably used in the high $p{-}T$ production regime of the SPS[Gyul95]. Since the transverse mass is given by $m_T = \sqrt{p_T^2 + m^2}$ we can write

$$\frac{1}{m_T}\frac{dN}{dm_T} = \frac{1}{p_T}\frac{dN}{dp_T},$$

and all the previously derived p_T distributions can also be described as invariant m_T distributions.

In Figs. 8.1 and 8.2 the invariant m_T distributions for negative and positive pions are shown in the rapidity range $3.75 < y < 5.5$, and in the p_T range defined by the acceptance discussed in $\oint$ 7.2. These data are binned in 0.25 rapidity bins and 50 MeV p_T bins. The spectra are shown as $1/m_T dN/dm_T$ plotted versus the transverse kinetic energy $m_T - m_0$, where m_0 is the pion rest mass. Each spectra is then subsequently scaled down by a factor of 10 so that all the data can be clearly seen on the same plot. A fit of the form

$$\frac{1}{m_T}\frac{dN}{dm_T} = C(T) \cdot exp(-\frac{m_T}{T})$$

has been performed to each spectrum for $m_T - m_0 > 0.2$ GeV. For $m_T - m_0 > 0.2$ GeV, the data is well described by the exponential form, as is evident from the nice linearity for all rapidity slices. However a clear deviation of the spectra from this linear behavior is seen below $m_T - m_0$ values of 0.2 GeV. The deviations are more severe for the π^- than for the π^+. These deviations will be referred to as the 'low-p_T pion excess' and will be quantized and discussed further in $\oint$ 8.4.

The details of the shape of the pion spectrum are more clearly seen by looking at the shape of the dN/dp_T transverse momentum spectra for a given individual rapidity slice, where the spectra are now seen as curves rather than in the linear

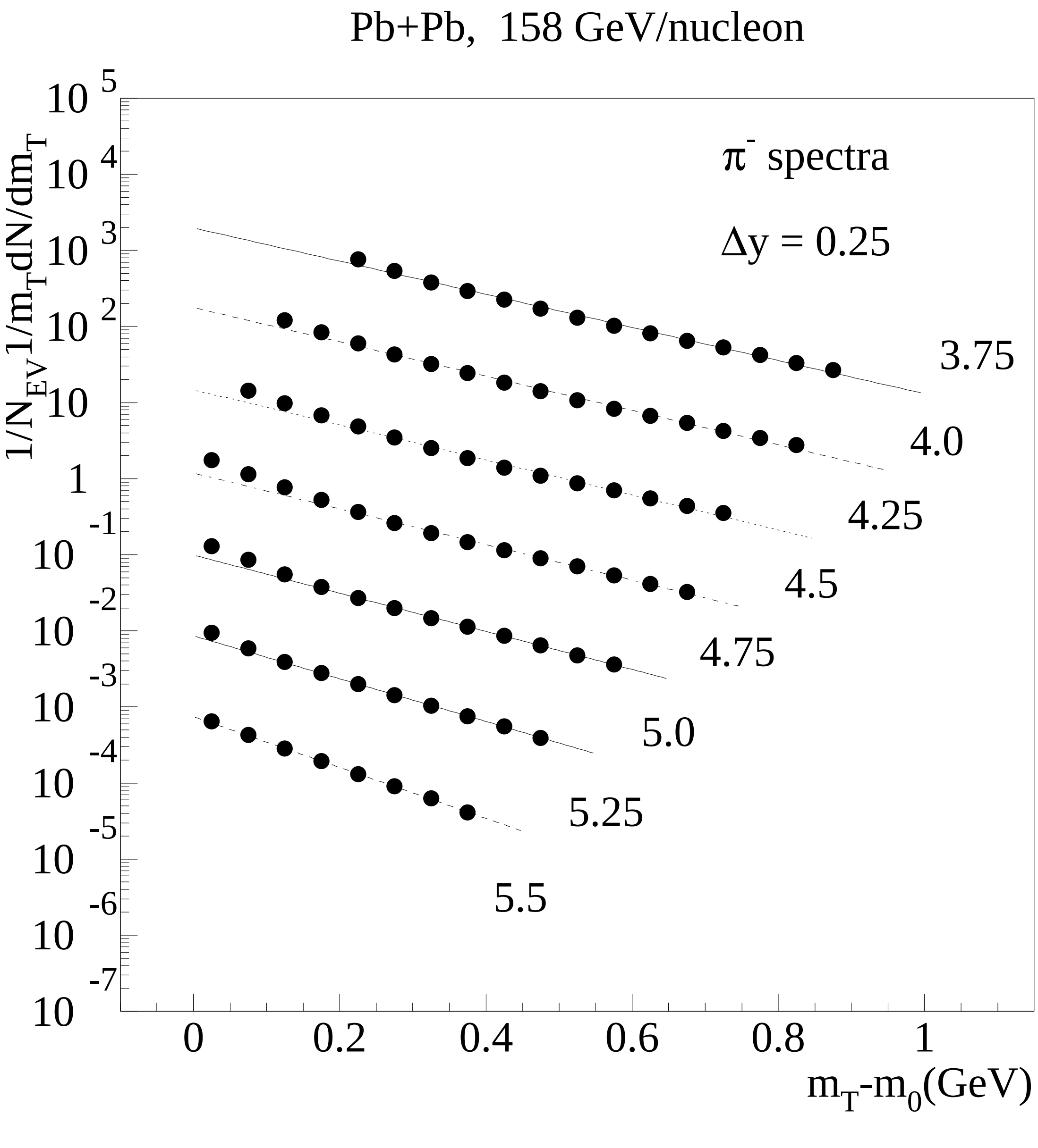

Figure 8.1: m_T spectra for negative pions. The data is binned in 0.25 units of rapidity, and each successive bin is scaled down by a factor of 10. A clear excess of pions is seen at $m_T - m_0$ less than 0.2 GeV, decreasing as a function of increasing rapidity.

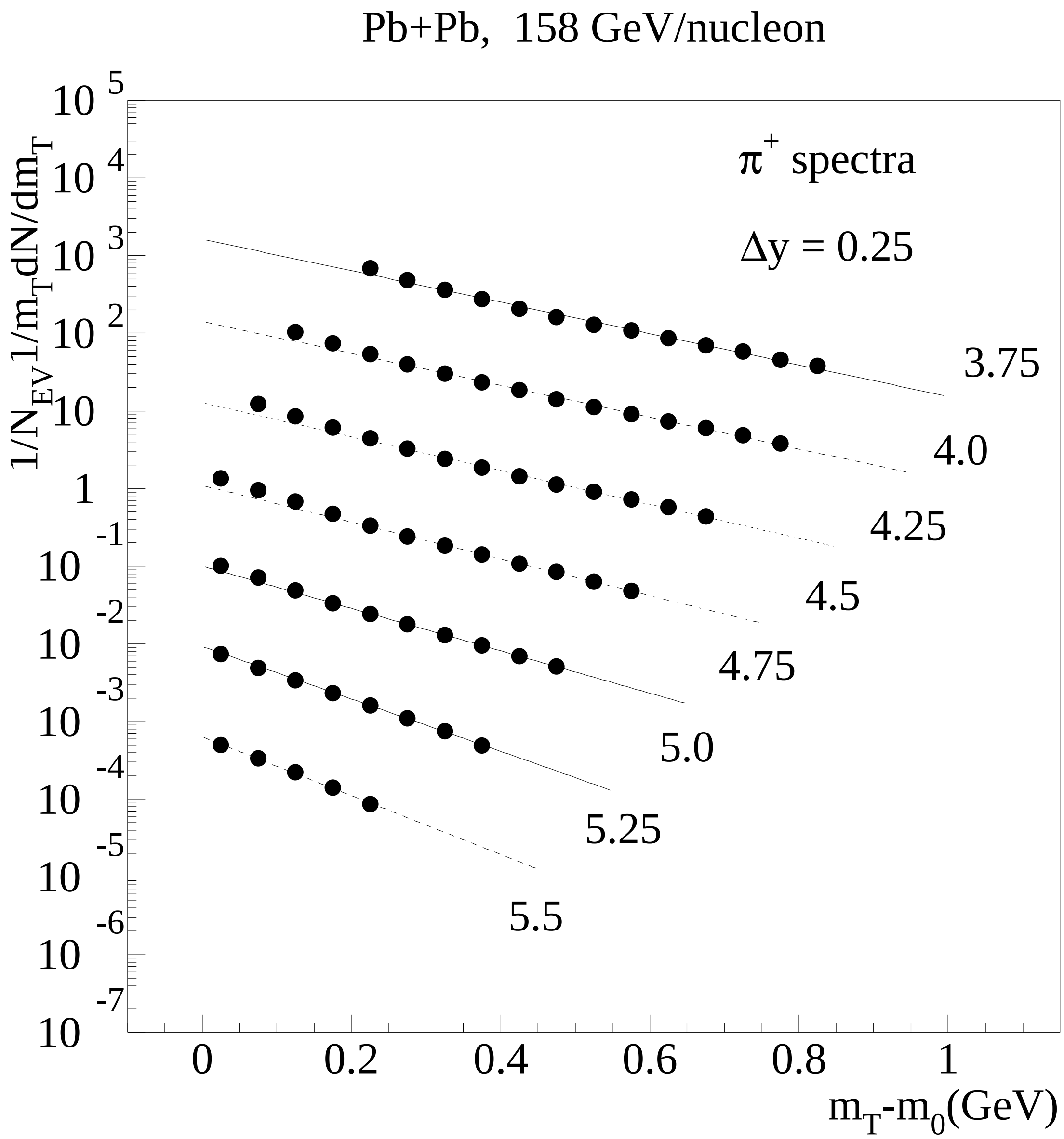

Figure 8.2: m_T spectra for positive pions. The data is binned in 0.25 units of rapidity, and each successive bin is scaled down by a factor of 10. An excess of pions is seen at $m_T - m_0$ less than 0.2 GeV, decreasing as a function of increasing rapidity.

form above. The data is fit in two different forms, and are then shown side by side for each rapidity slice. The first fit is a single exponential fit of the form

$$\frac{dN}{dp_T} = C(T) \cdot p_T \cdot exp(-\frac{m_T}{T}).$$

This fit describes the data well above $p_T > 0.3$ GeV, where the low p_T excess is minimal. In order to fit the low-p_T excess, a fit is performed which is the sum of two exponentials of the type shown above. This type of fit has been used to describe other pion data successfully at both SPS[Bach94] and AGS[Vide95] experiments. The data cannot be fit by any single- temperature function over the full p_T acceptance, unlike the protons and kaons which have been fit successfully with a single exponential[Jone96].

The results of these single and double exponential fits are shown side by side as a function of rapidity in Figs. 8.3-8.14, where dN/dp_T is plotted versus p_T for $4.0 < y < 5.5$. Each figure again represents a quarter unit of rapidity. Figs. 8.3-8.8 represent the negative pions, while Figs. 8.9-8.14 show the positive pions.

Several qualitative features should be noted concerning these single and double exponential fits. The double exponential fits do an excellent job describing the data over the entire rapidity range, while the single exponential fits describe the data well for $p_T > 0.3$ GeV/c. Since the low-p_T excess decreases as the rapidity increases, double exponential fits are not needed beyond rapidities of ~ 5, as the

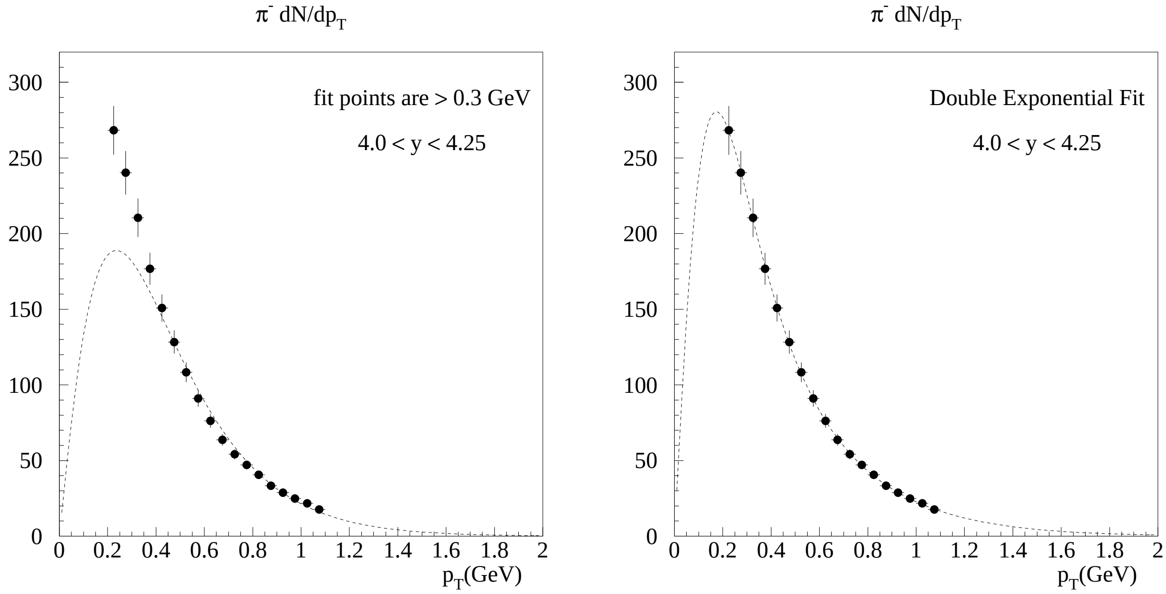

Figure 8.3: Single and double exponential fits for π^-, y = 4.0-4.25.

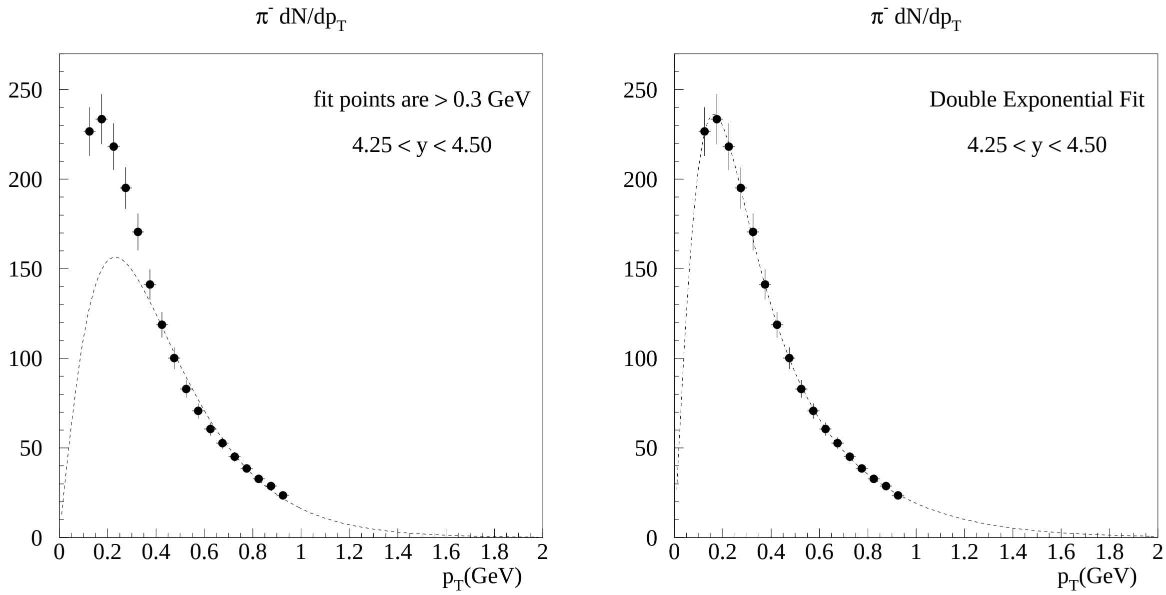

Figure 8.4: Single and double exponential fits for π^-, y = 4.25-4.50.

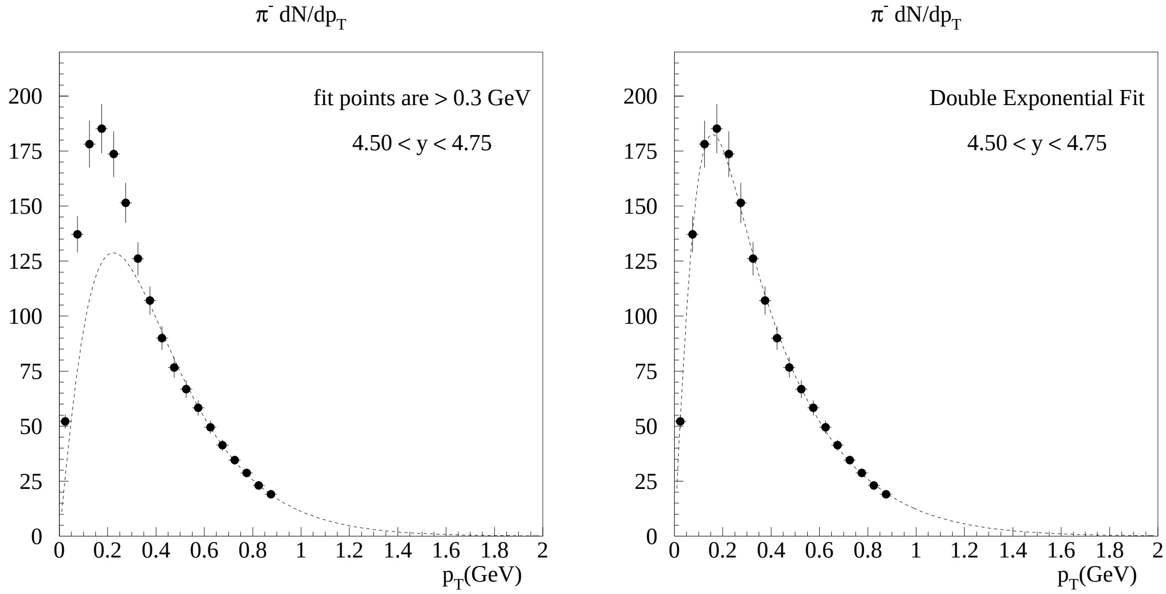

Figure 8.5: Single and double exponential fits for π^-, y = 4.50-4.75.

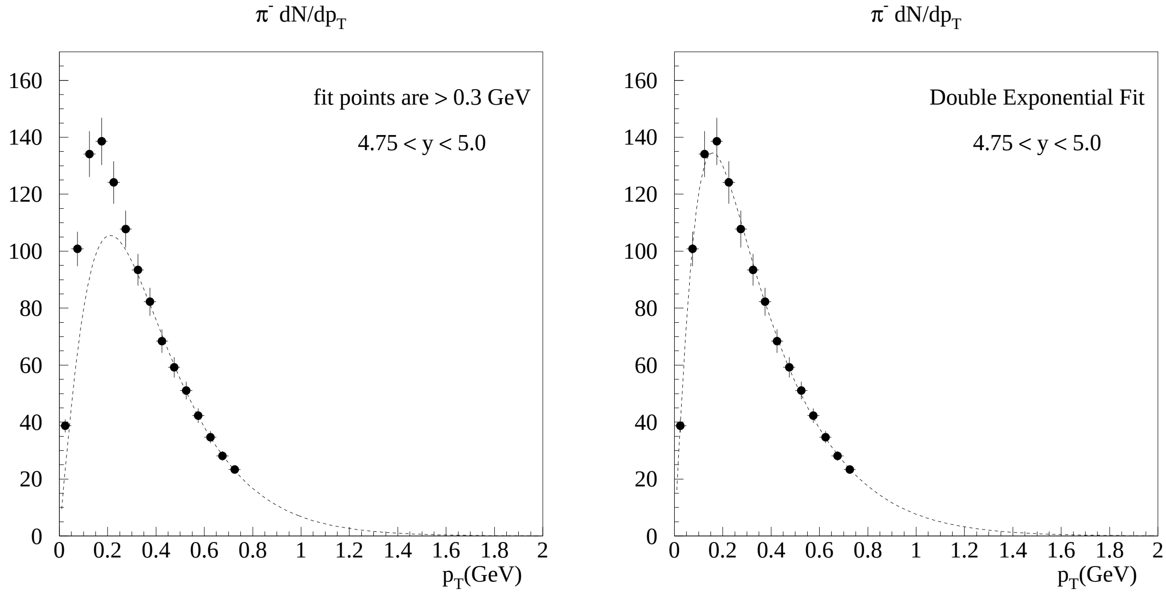

Figure 8.6: Single and double exponential fits for π^-, y = 4.75-5.0.

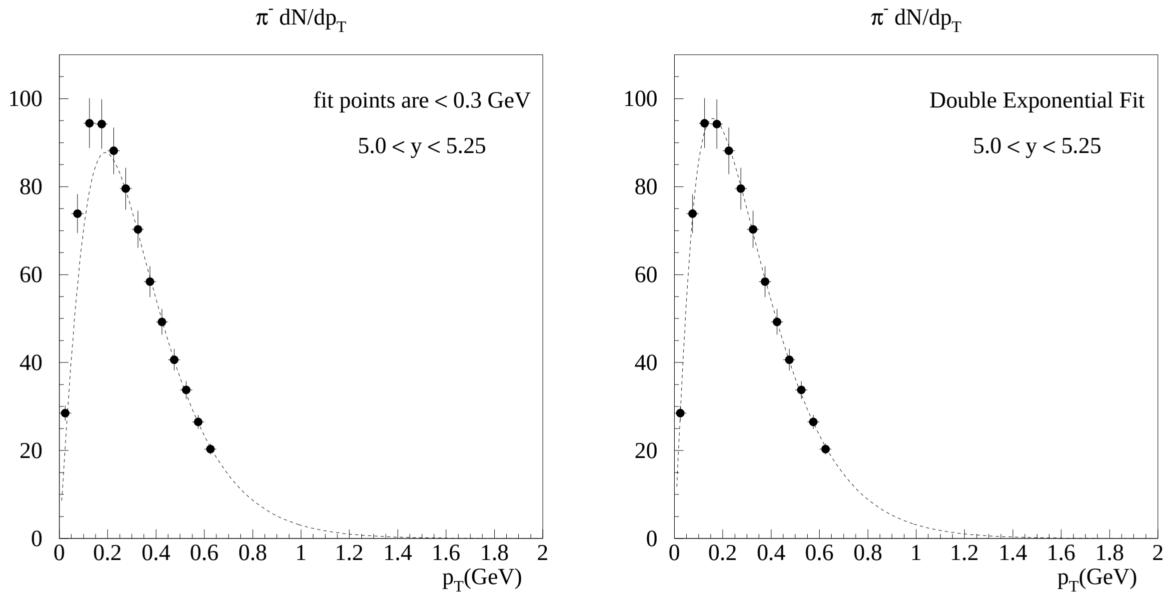

Figure 8.7: Single and double exponential fits for π^-, y = 5.0-5.25.

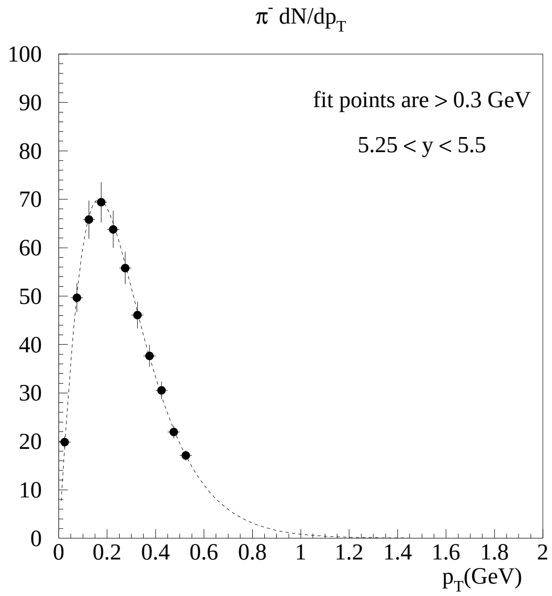

Figure 8.8: Single exponential fit for π^-, y = 5.25-5.50.

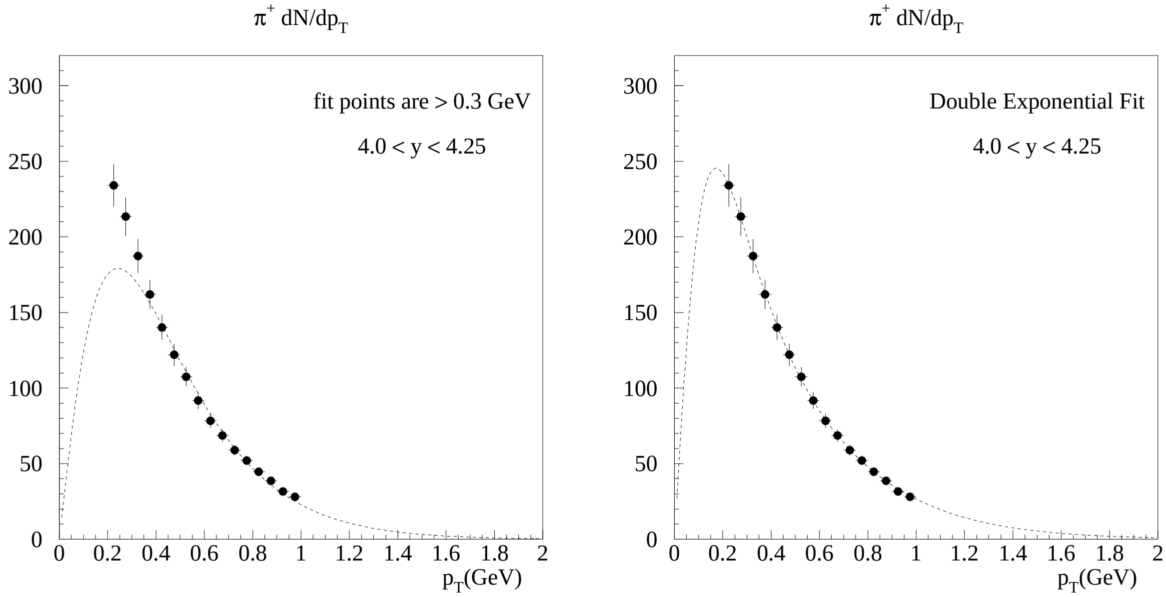

Figure 8.9: Single and double exponential fits for π^+, y = 4.0-4.25.

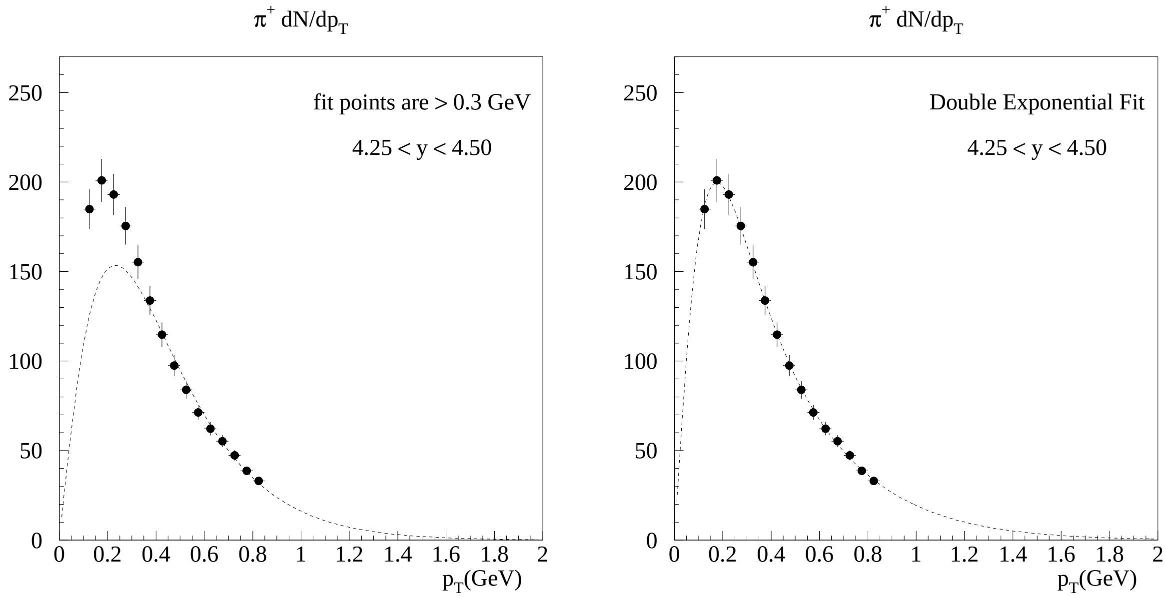

Figure 8.10: Single and double exponential fits for π^+, y = 4.25-4.50.

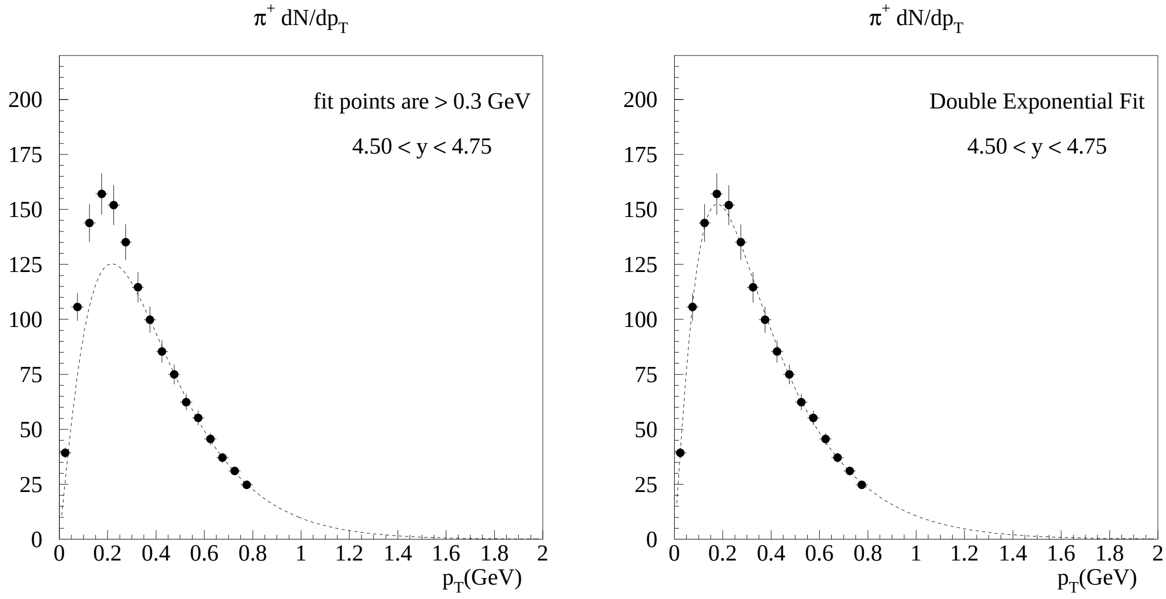

Figure 8.11: Single and double exponential fits for π^+, y = 4.50-4.75.

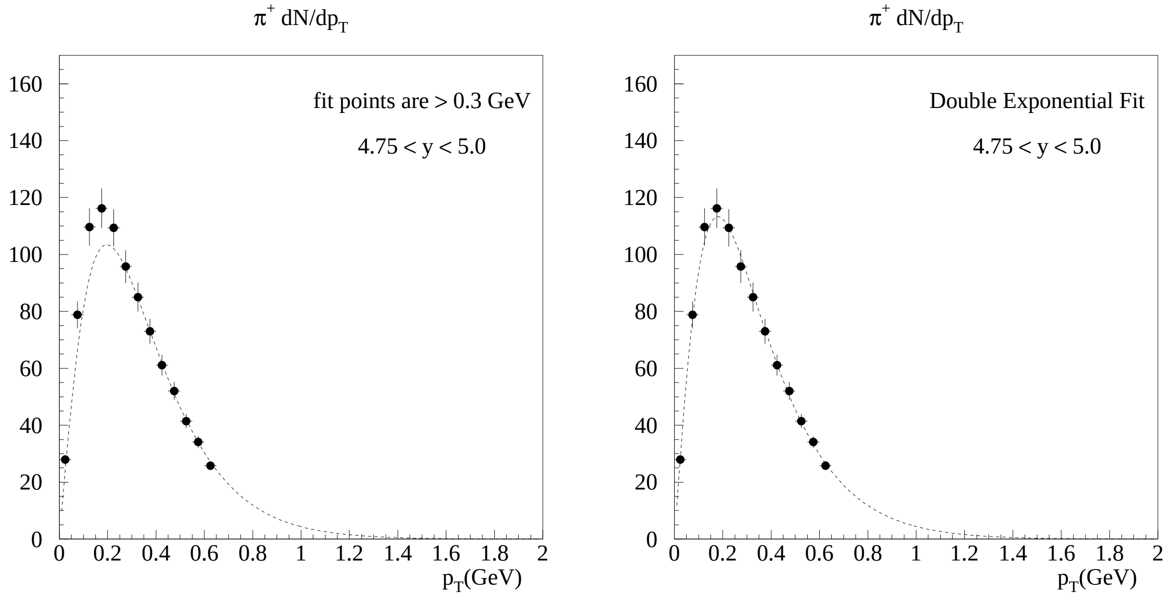

Figure 8.12: Single and double exponential fits for π^+, y = 4.75-5.0.

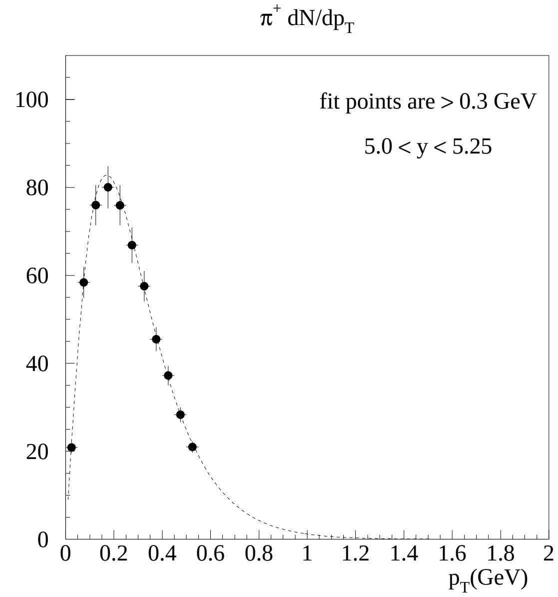

Figure 8.13: Single exponential fit for π^+, y = 5.0-5.25.

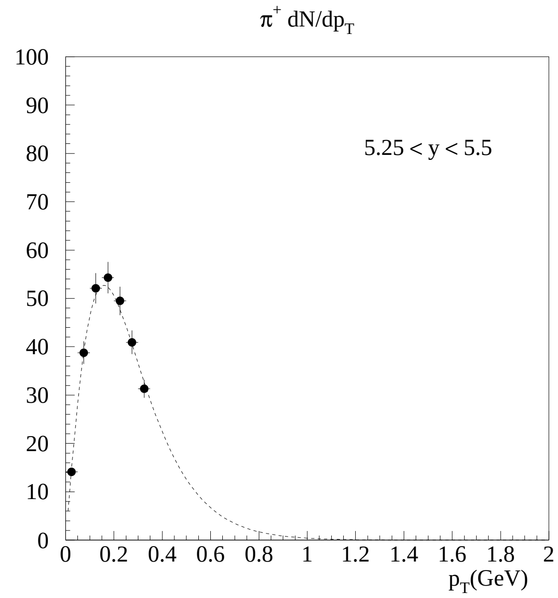

Figure 8.14: Single exponential fit for π^+, y = 5.25-5.50.

low-p_T excess is nearly gone.

8.3 Pion Inverse Slope Parameters(Effective Temperatures)

A summary of the inverse slope parameters from the single and double exponential fits are given in Tables 8.1 and 8.2. Table 8.1 shows the results of the single exponential fits to the transverse momentum spectrum, where the fit points where only $p_T > 0.3$ GeV. The temperatures for the π^- and π^+ are the same within the errors, as expected. These inverse slope parameters are in good agreement with the independent NA49 Time of Flight(TOF) results. The TOF wall has a pion acceptance which is approximately $3 < y < 5$, with a constantly varying p_T acceptance, often referred to as a 'banana' acceptance. For the TOF analysis the data was summed over the entire rapidity spectrum to perform the transverse momentum fits. There results were $T = 192 \pm 3$ for the $\pi-$, and $T = 188 \pm 7$ for the $\pi+$, which are consistent with the dE/dx results in the overlapping rapidity region.

The results of the inverse slope parameters from the double exponential fits are shown in Table 8.2. The results are given as T_1 and T_2, in the rapidity range $4.5 < y < 5.0$. Beyond rapidities of ~ 5 the low-p_T excess is nearly gone, thus only single exponential fits are appropriate. Below rapidities 4.5 the low-p_T acceptance does not extend all the way to $p_T = 0$, and the fits to the low-p_T excess are less

Table 8.1: Pion inverse slope parameters(in MeV) from single exponential thermal fits, $p_T > 0.3$ GeV.

rapidity bin	π^+(MeV)	π^-(MeV)
4.00–4.25	209±6	203±4
4.25–4.50	199±5	198±5
4.50–4.75	184±6	189±5
4.75–5.00	160±16	176±8
5.00–5.25	133±19	153±10
5.25–5.50	120±6	127±15

Table 8.2: Pion inverse slope parameters(in MeV) from double exponential thermal fits. T_1 describes the high p_T normal thermal distribution, T_2 describes the contribution from the low p_T enhancement.

rapidity bin	$T_1(\pi^+)$	$T_2(\pi^+)$	$T_1(\pi^-)$	$T_2(\pi^-)$
4.50–4.75	200±13	94±14	205±11	82±10
4.75–5.00	166±10	94±25	188±13	74±14

reliable due to a decreasing number of data points. T_1 describes the temperature of the dominant portion of the fit, and gives temperatures approximately 10 MeV higher than the single exponential fits. The second temperature, T_2, describes the thermal source of the low-p_T excess. The physical origin of this second thermal source is a manifestation of the underlying resonance decay structure[Soll90]. The thermalized resonances will then decay, always sharing their energy between 2 or more particles, leading to the lower temperature for the second source(by a little more than a factor of 2).

These extracted slope parameters should not be viewed as the temperature, T, of a hot, thermalized pion source. Recent theoretical devleopments and experimental results have shown that these inverse slope paramters should be viewed as *effective temperatures* which describe both the freezeout temperature(random thermalized motion in local rest frame), T_0, of the thermal source and any collective transverse flow which may be present. The compression and subsequent explosion of the nuclear fireball is thought to give each particle species in the fireball a common collective flow velocity, β, which has been shown to contribute to the measured inverse slope parameters[Bear96]. In hydrodynamics, matter flows, i.e. all particles flow at a common collective velocity. Classically, the collective kinetic energy will then depend on the particle mass; particles with higher mass will have higher energy. The slope parameter is a measure of the kinetic energy induced by the transverse motion, including both the thermal and collective modes. Thus for particles with similar thermal sources, those with higher mass should have higher slope parameters if substantial collective flow is present.

The fact that the inverse slope parameters are rising for particle species with higher masses at NA49 confirms this behavior. Recent NA49 analyses[Jone96] summarizing the inverse slope parameters for different particle species give $T_{protons} \approx 300 MeV$, $T_{kaons} \approx 220 MeV$, and $T_{pions} \approx 190 MeV$ from the dE/dx and TOF analyses. The high temperature of the baryons suggests substantial collective transverse flow is being generated in these collisions, although it is unclear why the intermediate mass kaons show only a small increase over the pion effective temperatures.

One method used to characterize these different slope parameters is a model employing a thermal source with collective expansion. Such models yield two parameters to describe the spectra for different particles: a common thermal freezeout temperature(T_0) and a collective transverse flow velocity(β). A fit of this form to the NA49 data[Stac97] yields $T_0 = 160$ MeV, and $\beta = 0.30$. A similar analysis by the NA44 collaboration[Bear97] to their transverse mass spectra yields a similar result, with $T_0 = 167$ MeV, and $\beta = 0.36$.

8.4 Pion Low p_T Excess

A low-p_T enhancement of pion spectra has been observed by several experiments at both the BNL AGS[Hemm94, Barr94, Vide95] and CERN SPS[Akes90, Murr94, Bach94]. Several theoretical explanations have been posed over the years[Simo94], including collective transverse flow, the decay of small QGP droplets, and secondary pion production in thick targets. But several theorists have also recognized that a large, undeniable contribution to the low-p_T excess is coming from the influence of hadronic resonances[Brow91, Soll94]. It has been shown[Simo94] that at AGS energies the dominant contribution to the pions for $p_T < 300$ MeV is from baryonic resonances, primarily the $\Delta(1232)$, but also the N^* and Δ^*. At SPS energies, both baryonic and mesonic resonances give significant contribution. The mesonic resonances include the ρ, η, η' and ω. The nucleons and pions produced from the decay of a baryonic resonances(or pions produced from mesonic resonances) share the parent resonance's energy and thereby produce a relatively 'cold' component in the pion spectrum compared to those pions produced from non-resonance interactions.

The low-p_T pion excess for both $\pi-$ and π^+ can be seen in the previously mentioned Figs. 8.3-8.14. The excess is seen to be larger for $\pi-$, presumably due to the neutron/proton asymmetry in the incoming nucleons. Since there are a larger number of neutrons than protons, the baryonic resonances such as the Δ would produce more $\pi-$ than π^+[Ahle96]. The excess for both $\pi-$ and π^+ is peeked toward mid-rapidity, as the effect is decreasing at larger rapidities and is gone by y=5 for π^+, and y=5.25 for $\pi-$.

A summary of the pion low-p_T excess as a function of rapidity is given in Table 8.3. Here the excess is defined to be the difference of the pion yield from the single and double exponential fits, divided by the yield from the single exponential fit. Total pion yields(extrapolating to the full phase space in y and p_T) will be given in the following section, however the excess from these total yields is 25% for $\pi-$ and 23% for π^+.

8.5 Integrated Pion Yields

In order to determine the pion rapidity density dN/dy as a function of rapidity, the transverse momentum dN/dp_T spectra must be fit and integrated to include the entire p_T range from 0 to ∞. In order to obtain the total charged pion multiplicities over the full phase space, the yields from the individual rapidity slices must be fit

Table 8.3: The low-p_T excess quantized as a function of rapidity, between $4.0 < y < 5.5$.

	Excess(%)	
rapidity bin	π^+	π^-
4.00–4.25	20.1	24.4
4.25–4.50	17.1	26.1
4.50–4.75	12.6	21.5
4.75–5.00	5.1	15.5
5.00–5.25	0	6.2
5.25–5.50	0	0

over y to a gaussian form and integrated over the entire rapidity range.

The resulting yields from the individual rapidity slices for $\pi-$ are given in Figs. 8.16 and 8.17. The analogous yields for the $\pi+$ are given in Figs. 8.18 and 8.19. The points in figures 8.16 and 8.18 include the rapidity slices from $3.75 < y < 5.50$, and are extracted from the integration from 0 to ∞ in p_T of the single exponential fits. Since these fits only use values of $p_T > 0.3$ GeV, they can be extended down to rapidity 3.75. The points in figures 8.17 and 8.19 include the rapidity slices from $4.25 < y < 5.5$, and are extracted from the integration of the double exponential fits. These data points start at y = 4.25, which have sufficient low-p_T coverage to begin performing double exponential fits. All data points obtained from the exponential fits are reflected about mid-rapidty($y_{mid} \sim 2.9$). These distributions are then fit with a single gaussian function, and integrated from $-\infty < y < +\infty$ to obtain the total mean multiplicities of pions over the full phase space.

The final pions yields are summarized in Table 8.4 for the two different fitting methods. The yields from the single exponential fits to the data are called dE/dx(1), while the yields from the double exponential fits are called dE/dx(2). Also included are the NA49 Time of Flight(TOF) results from Frank Eckhardt's thesis[Eckh96]. The TOF results include the low-p_T excess. As can be seen, the TOF and dE/dx(2) results are in excellent agreement. The weakness of the double exponential fit results is from the large extrapolation to mid-rapidity, as the MTPC has no pion acceptance down to p_T=0 from $\sim y < 4$. Eventually forthcoming pion

Table 8.4: Final pion multiplicities extrapolated to full phase space. dE/dx(1) represents the results from the single exponential fits for $p_T > 0.3$ GeV, dE/dx(2) represents the total pion multiplicities from the double exponential fits, including the low-p_T excess.

	$<\pi^+>$	$<\pi^->$	$\frac{<\pi^->}{<\pi^+>}$
dE/dx(1)	533 ±42	556 ±39	1.04
dE/dx(2)	655 ±57	695 ±46	1.06
TOF	642 ±60	679 ±60	1.06

spectra from the VTPC's will make the pion identification complete, including up to mid-rapidity.

8.6 π^+/π^- Ratio(Coulomb Effect)

The Coulomb effect has been recently observed in pion spectra at both the BNL AGS[Ahle96] and CERN SPS[Bogg96], where large, high Z nuclei serve as both target and projectile in A+A collisions. This effect is analogous to the famous spectral distortions in positive and negative beta decay, often described by the so-called Fermi functions[Kran88] F(Z',p), where Z' is the atomic number of the

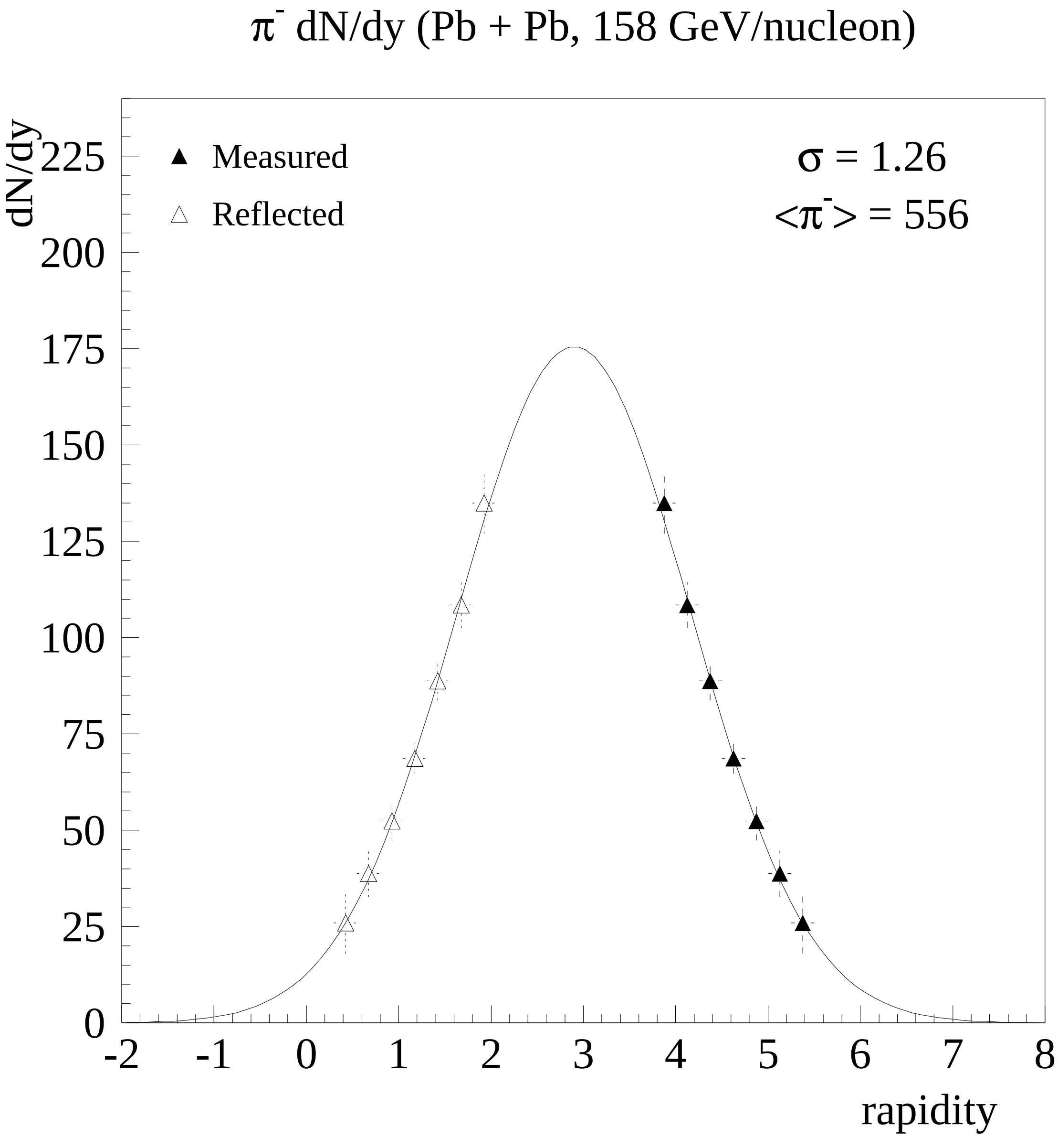

Figure 8.15: Rapidity distribution and total yields for π^-, extracted from the single exponential fits.

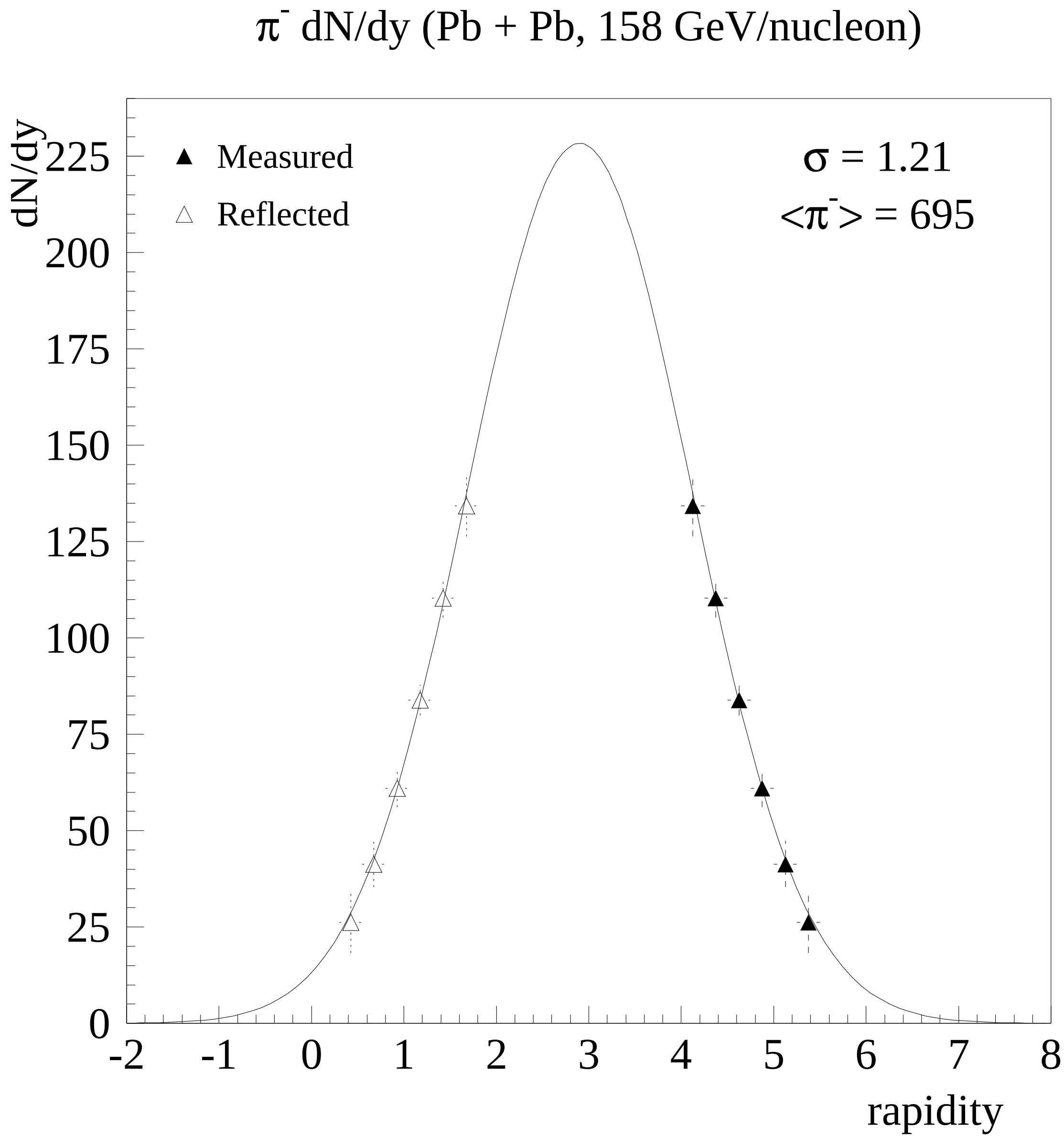

Figure 8.16: Rapidity distribution and total yields for π^-, extracted from the double exponential fits.

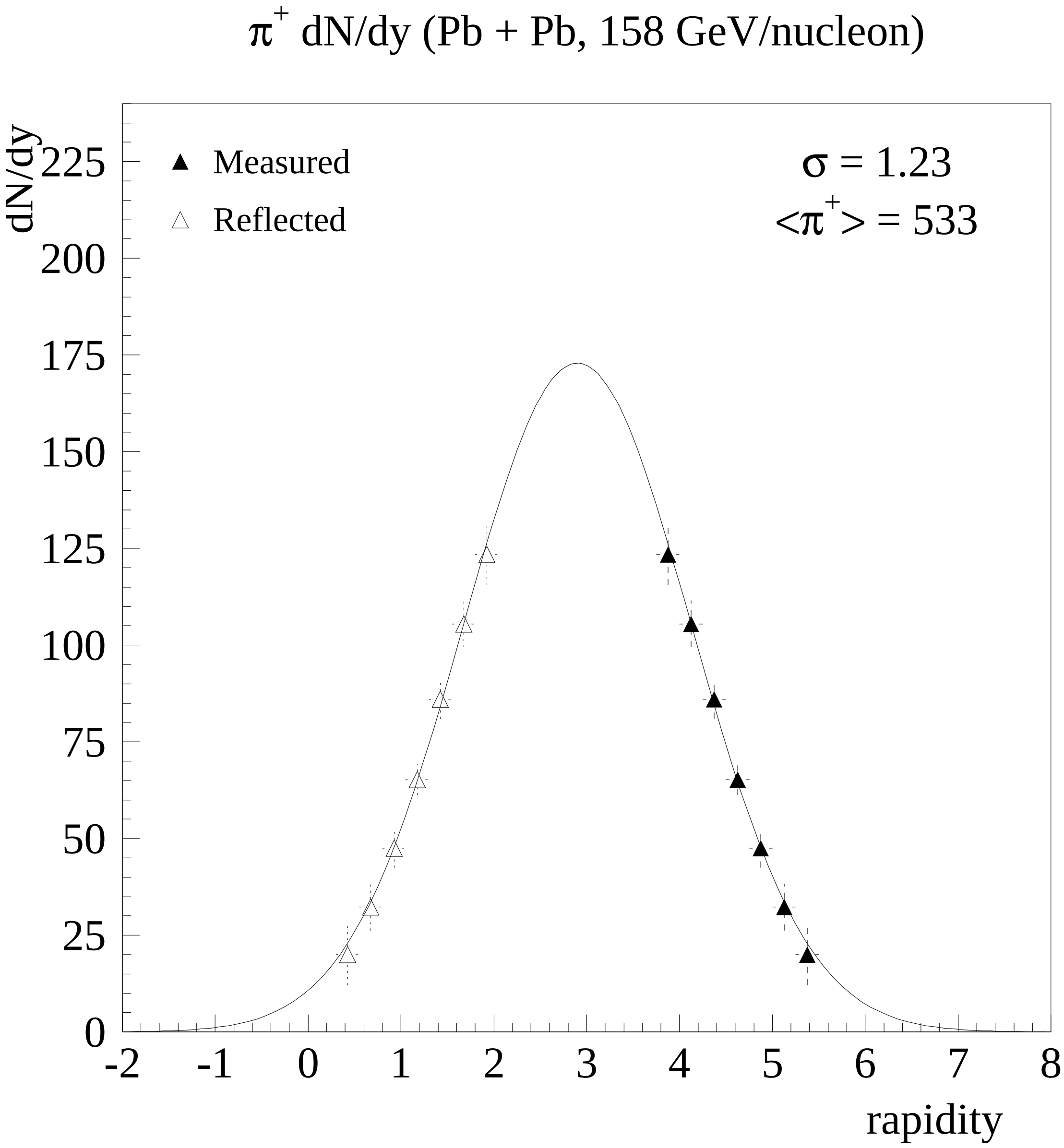

Figure 8.17: Rapidity distribution and total yields for π^+, extracted from the single exponential fits.

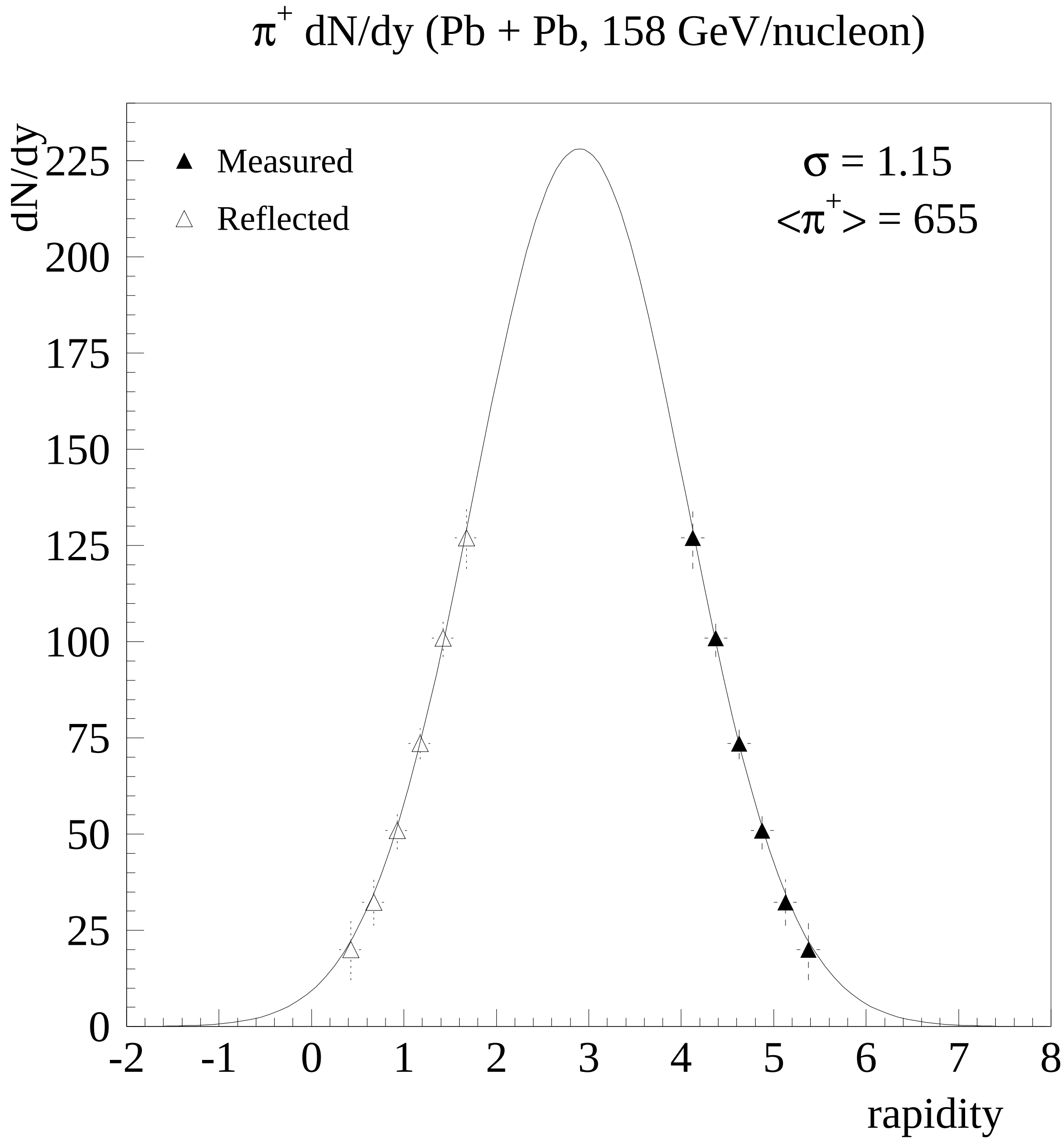

Figure 8.18: Rapidity distribution and total yields for π^+, extracted from the double exponential fits.

daughter nucleus, and p is the momentum of the ejected beta particle.

In truly heavy-ion collisions, such as the Pb+Pb collisions at NA49, the large amount of positive charge in the system can introduce additional distortions of the final particle distributions. The force of the Coulomb interaction between the positively charged protons and the positive and negative pions will be manifest as a distortion of the final momentum spectra of these pions.

The identified charged pion spectra previously shown were used to construct the ratio π^-/π^+ as a function of p_T. The result is shown in Fig. 8.19 as a function of rapidity in the range $4.25 < y < 5.0$. The data are arbitrarily normalized to unity at high p_T. As can be seen in the data, the ratio π^-/π^+ is distorted for values of $p_T < 200$ MeV, with the distortion increasing as you move towards $p_T = 0$. The ratio reaches a maximum distortion of ~ 1.5 at $p_T = 0$ for the y=4.25-4.5 rapidity bin, with the effect decreasing with increasing rapidity to a maximum distortion of ~ 1.2 for the y=4.75-5.0 rapidity bin.

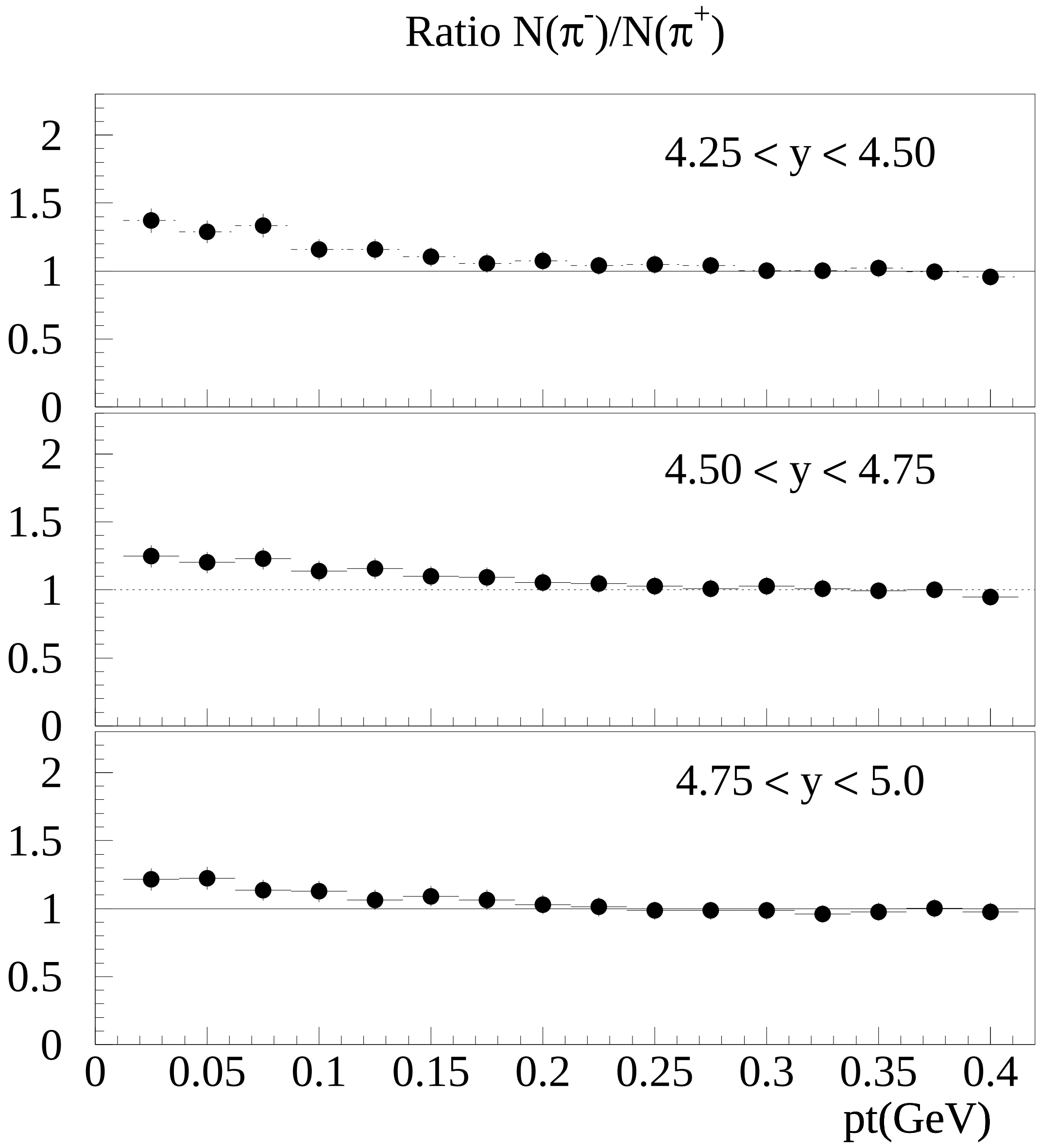

Figure 8.19: Coulomb effect on positive and negative pions in the rapidity range $4.25 < y < 5$.

Chapter 9

Discussion

In order to interpret the physics implications of the pion spectra measurements made via dE/dx, a comparison needs to be made with previous similar measurements and/or models. The NA49 pion data will be compared with experiment NA35, of which NA49 is the daughter experiment. The NA35 experiment was performed at a similar beam energy but with smaller ^{32}S projectile nuclei, and so the dependence on A can be studied and discussed. The data will also be compared with the microscopic string model VENUS. The Coulomb effect observed at NA49 will be compared with a similar measurement at the spectrometer experiment NA44, which is upstream one experiment from NA49 in the CERN North Area. Finally, the crucial subject of the implications of the pion production on the entropy, and thus Quark-Gluon Plasma formation will be discussed in detail.

9.1 Comparison with S+S Data(NA35)

As previously mentioned, NA49 is the daughter experiment of NA35. NA35 has studied collisions of ^{32}S projectiles at 200 GeV per nucleon incident energy with various targets. At NA35 the charged particles were detected in two large volume tracking chambers: the NA35 Streamer Chamber placed inside a 1.5 Tesla dipole magnet(same magnet as at NA49), and the NA35 Time Projection Chamber positioned downstream of the magnet. The NA35 pion production is derived from a measurement of negative hadrons, h-, in the Streamer Chamber. Since there is no particle identification in this chamber(except from visually identified strange particle decay topologies), the π^- multiplicity discussed here is computed from the h- yields minus the measured K^- and $\overline{p}$ yields.

The comparison of the measured π^- yield via dE/dx at NA49 is compared to the NA35 h- yield in Fig. 9.1. The total yield of NA35 negative hadrons is $\langle h- \rangle = 98 \pm 3$. After subtracting out the K^- and $\overline{p}$ yields the NA35 π^- yield is $\langle \pi^- \rangle = 91 \pm 3$. This is to be compared with the NA49 result of $\langle \pi^- \rangle = 695 \pm 46$. The ratio of the NA49 to NA35 π^- yields gives

$$\frac{\langle \pi^- \rangle_{NA49}}{\langle \pi^- \rangle_{NA35}} = \frac{695}{91} \sim 7.5.$$

This measured ratio of the pion yields is similar to the ratio of the number of nucleons for the two nuclei, which is $(416/64) = 6.5$. The actual ratio of participants

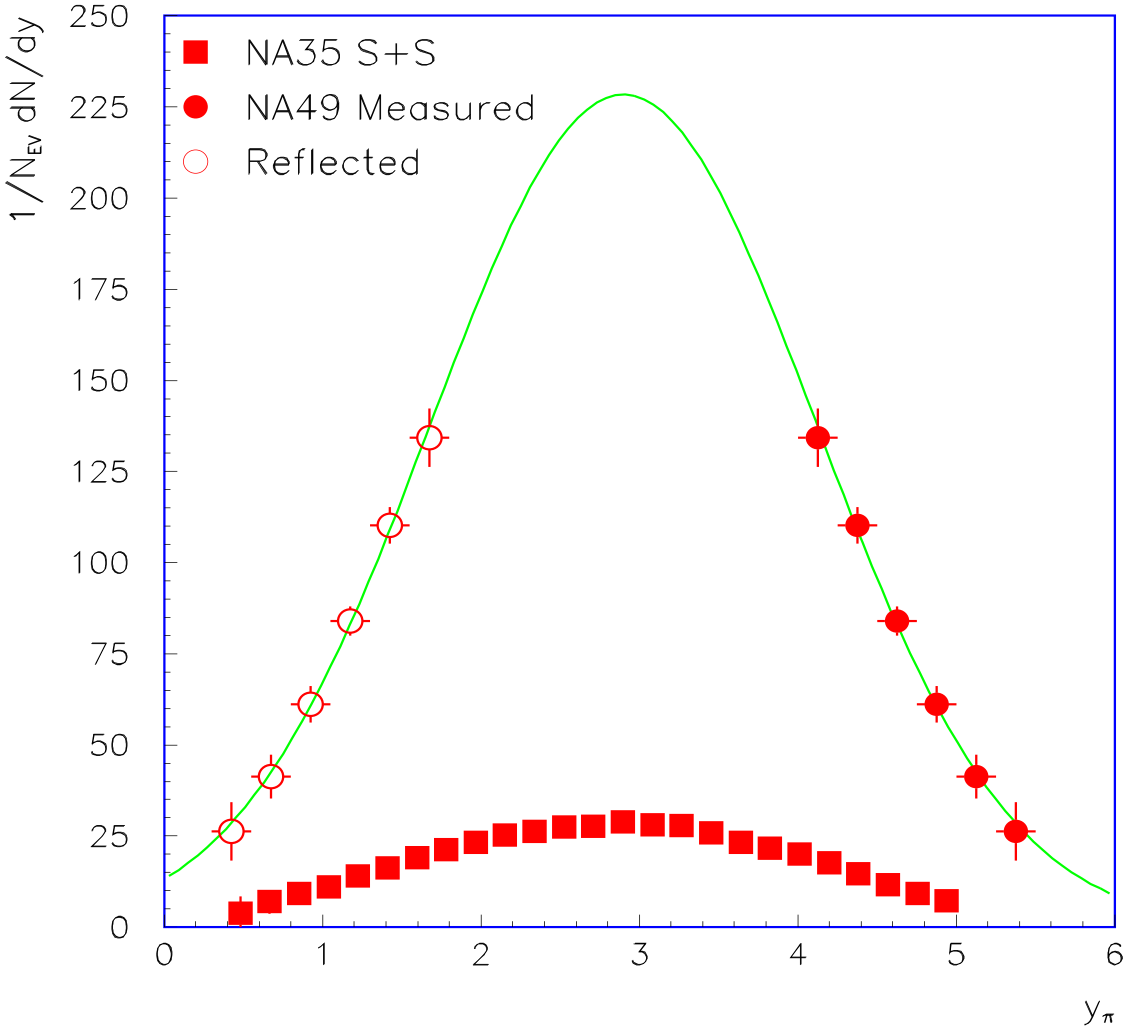

Figure 9.1: NA49 and NA35 pion production comparison. The squares represent the NA35 h- yield, with $\langle h- \rangle = 98 \pm 3$. The circles represent the NA49 dE/dx π^- yield, with $\langle \pi^- \rangle = 695 \pm 46$.

will be a little higher due to more surface to volume ratio in the smaller ^{32}S nucleus, and is found to be (390/58) $\sim$ 6.7[Albe95]. So to first order it appears that the increase in pion production in going from NA35(^{32}S nuclei) to NA49(^{208}Pb nuclei) scales according to the number of participants. This is similar to other NA49 results, which have found that the kaon yield scales with the ratio of participants[Marg96]. Since many observers in the heavy ion community were expecting exciting new behavior in moving from ^{32}S to ^{208}Pb beams, these scaling results are somewhat disappointing, in that they don't suggest any substantially new physics is taking place. However it does suggest the reaction mechanisms are similar for the two systems, with the Pb+Pb collisions merely having a larger interaction volume. One conclusion is that if the QGP is either formed or not formed at the SPS with ^{32}S beams, the same scenario takes place when the system size is increased to ^{208}Pb. We will return to this point in $\oint$ 9.4, when the relation of the pion production to the entropy is discussed.

Inverse slope parameters(effective temperatures) were also measured for negative hadrons at NA35[Bach94]. The h- spectra were binned in one-unit rapidity bins, and then fit with a two-component thermal fit as with the NA49 dE/dx fits. NA35 fit the h- from $1 < y < 2$, which corresponds to the rapidity range $4 < y < 5$ due to reflection about mid-rapidity($y_{mid} \sim 3$). It should be mentioned that there is some contamination due to K^- and $\overline{p}$ in the h- fits, though it should be minimal. No similar fits were done for h+ at NA35 due to the proton contamination and a

Table 9.1: Pion inverse slope parameters(in MeV) from double exponential thermal fits. T_1 describes the high-p_T normal thermal distribution, T_2 describes the contribution from the low-p_T enhancement.

rapidity bin	$T_1(\pi^-)$	$T_2(\pi^-)$
NA49: 158A GeV/c Pb+Pb		
4.50–4.75	205±11	82±10
4.75–5.00	188±13	74±14
NA35: 200A GeV/c S+S		
4.00–5.00	188 ±8	83 ±6

lack of PID in the streamer chambers for spectral deconvolution.

The comparison of the the two slope parameters, T_1 and T_2, from the double exponential fits of both experiments are shown in Table 9.1. The NA49 results are the π^- results described in $\oint$ 8.3, while the NA35 results are for h- in the rapidty range $4 < y < 5$, which corresponds to the overlapping acceptance region of the NA49 π^- dE/dx analysis. The temperature T_2 for the resonance decays leading to the low-p_T pion excess is found to be similar for both systems, at $\sim$80 MeV. The temperature T_1 of the dominant portion of the spectra is also found to be similar for both systems, although slightly higher in the Pb+Pb system. This may be due to more collective flow in the larger Pb+Pb system(presumably caused by increased compression).

9.2 VENUS Comparisons

9.2.1 The VENUS Model

The VENUS model[Werner87] is a microscopic parton-string model which has been very successful in describing particle production in a variety of different nucleus-nucleon and nucleus-nucleus collisions, over a range of different energies. Unlike macroscopic hydrodynamical models, the VENUS model attempts to model nuclear collisions via keeping track of the individual, microscopic parton-parton collisions within nucleons. During these collisions, particle production takes place via the formation and fragmentation of strings among the partons in the projectile and target nucleons. These strings are formed via the colour excitations between two partons; the strings then fragment as they are stretched, breaking into smaller and smaller fragments until all such fragments are below a given mass threshold. These final fragments are identified as the final state produced particles. The probability of two particles interacting in the initial nuclear collisions or in secondary scatterings is calculated via a geometrical Glauber calculation, using measured values for various inelastic cross-sections.

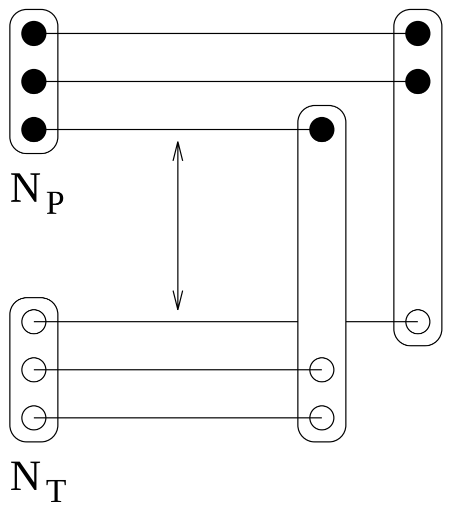

Figure 9.2: A simple example of colour exchange and string formation in nucleon-nucleon collisions.

The simplest such string formation in a nucleon-nucleon collision is shown in Fig. 9.2. The projectile nucleon N_P and the target nucleon N_T are represented by their three valence quarks, which are enclosed by a line, indicating that they form a colour neutral object. Colour exchange(indicated by the arrow) between a quark of N_P with one quark of N_T changes the colour structure, leading to two strings involving a diquark from N_P and a quark from N_T and vice versa. The time evolution of this system would involve the string fragmentation and particle production described above. This chosen example, in which the nucleon is represented by only its three valence quarks is an oversimplification. As is well know, a nucleon does not only contain valence quarks but also a sea of non-valence quarks and gluons. These higher order diagrams are also considered in the VENUS model.

9.2.2 NA49/VENUS Comparison

The comparisons of the transverse mometum(p_T) spectra for positive pions are shown in Figs. 9.3 and 9.4. In the plot the dashed curve is the VENUS 4.12 prediction, while the data points are from the dE/dx analysis. Also shown as a solid line is the single exponential fits to the dE/dx data, with the fit points being $p_T > 0.3$ GeV(i.e. the fits described in ∮ 8.2 which exclude the low-p_T excess). Two primary qualitative features of the VENUS predictions should be noted. The first is that the VENUS spectra are consistently cooler than the data, i.e. have less high-p_T pion production. The second is that the VENUS predictions do not adequately describe the low-p_T excess. This is probably due to the fact that the VENUS code does not incorporate resonance production in its string formalism. The fact

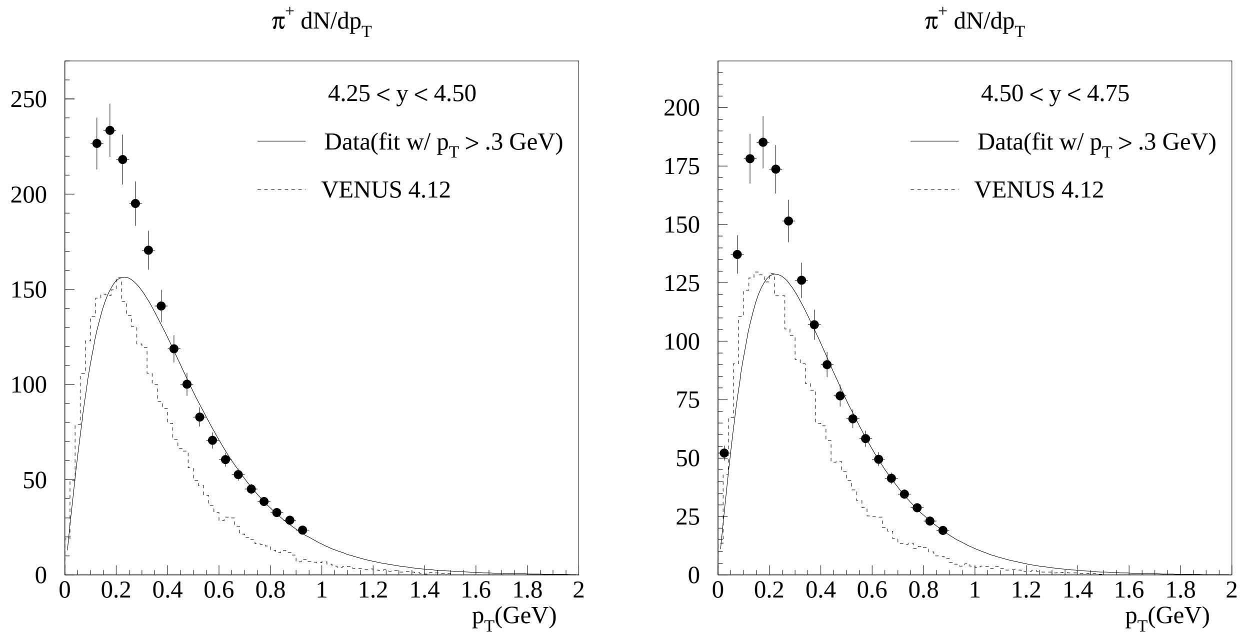

Figure 9.3: Comparison of positive pion p_T spectra from VENUS and the NA49 dE/dx analysis, in the rapidity range $4.25 < y < 4.75$.

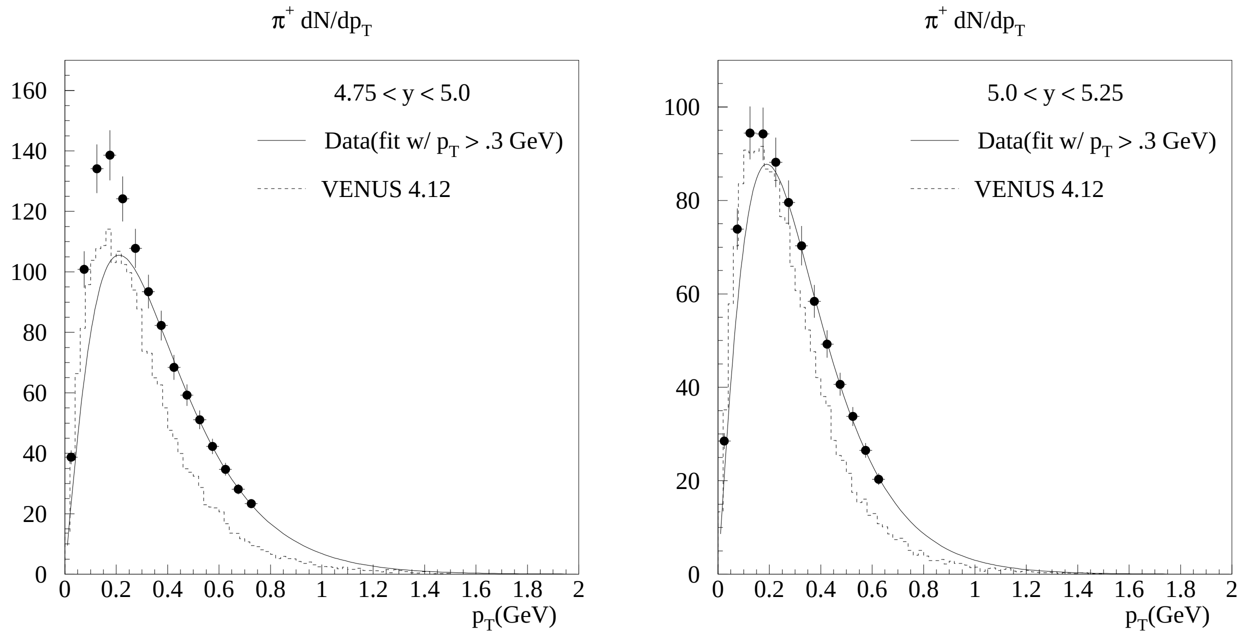

Figure 9.4: Comparison of positive pion p_T spectra from VENUS and the NA49 dE/dx analysis, in the rapidity range $4.75 < y < 5.25$.

Table 9.2: Final pion multiplicities extrapolated to full phase space. dE/dx(1) represents the results from the single exponential fits for $p_T > 0.3$ GeV, dE/dx(2) represents the total pion multiplicities from the double exponential fits, including the low-p_T excess. Also shown are the VENUS results. The VENUS results are in good agreement with the dE/dx(1) results which excludes the low-p_T excess.

	$<\pi^+>$	$<\pi^->$	$\frac{<\pi^->}{<\pi^+>}$
dE/dx(1)	533 ±42	556 ±39	1.04
dE/dx(2)	655 ±57	695 ±46	1.06
VENUS	513	542	1.06

that VENUS misses the low-p_T excess has been documented previously[Simo94, Eckh96]. As the low- p_T excess in the data disappears(at y $\sim$ 5), the VENUS code does a better job of describing the data.

Figs. 9.5 and 9.6 show the VENUS π^+ and π^- dN/dy rapidity distributions. Also shown are the dE/dx results with the single exponential fits to p_T spectra. As can be seen, there is reasonable agreement between the VENUS spectra and the dE/dx spectra which exclude the low-p_T excess. VENUS underpredicts the yields near mid-rapidity and overpredicts the yields near the target and beam rapidities. As shown in Table 9.2, the integrated yields of the VENUS spectra are similar,

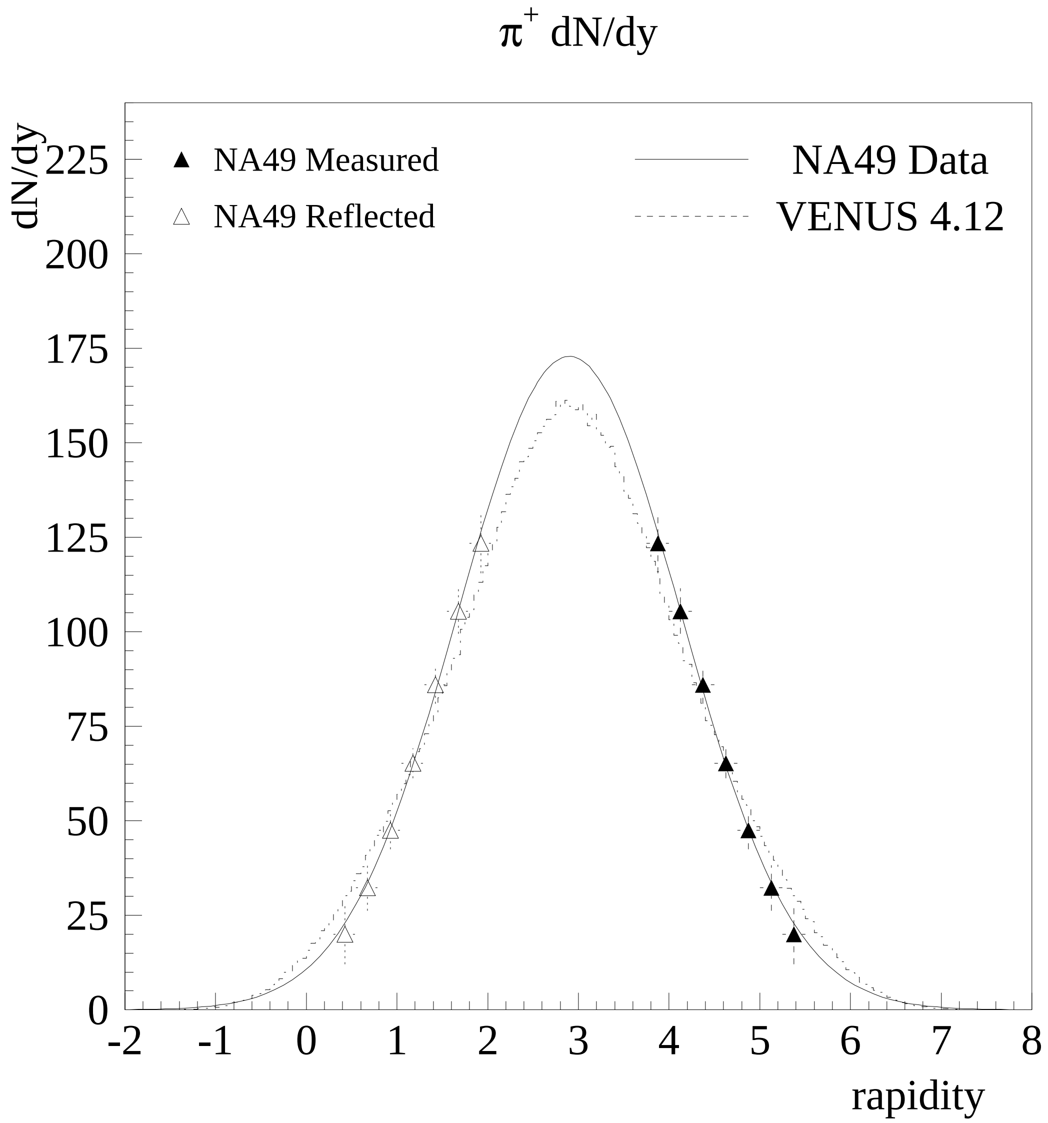

Figure 9.5: A comparison of positive pion dN/dy spectra from VENUS and the NA49 dE/dx analysis(excluding the low-p_T excess).

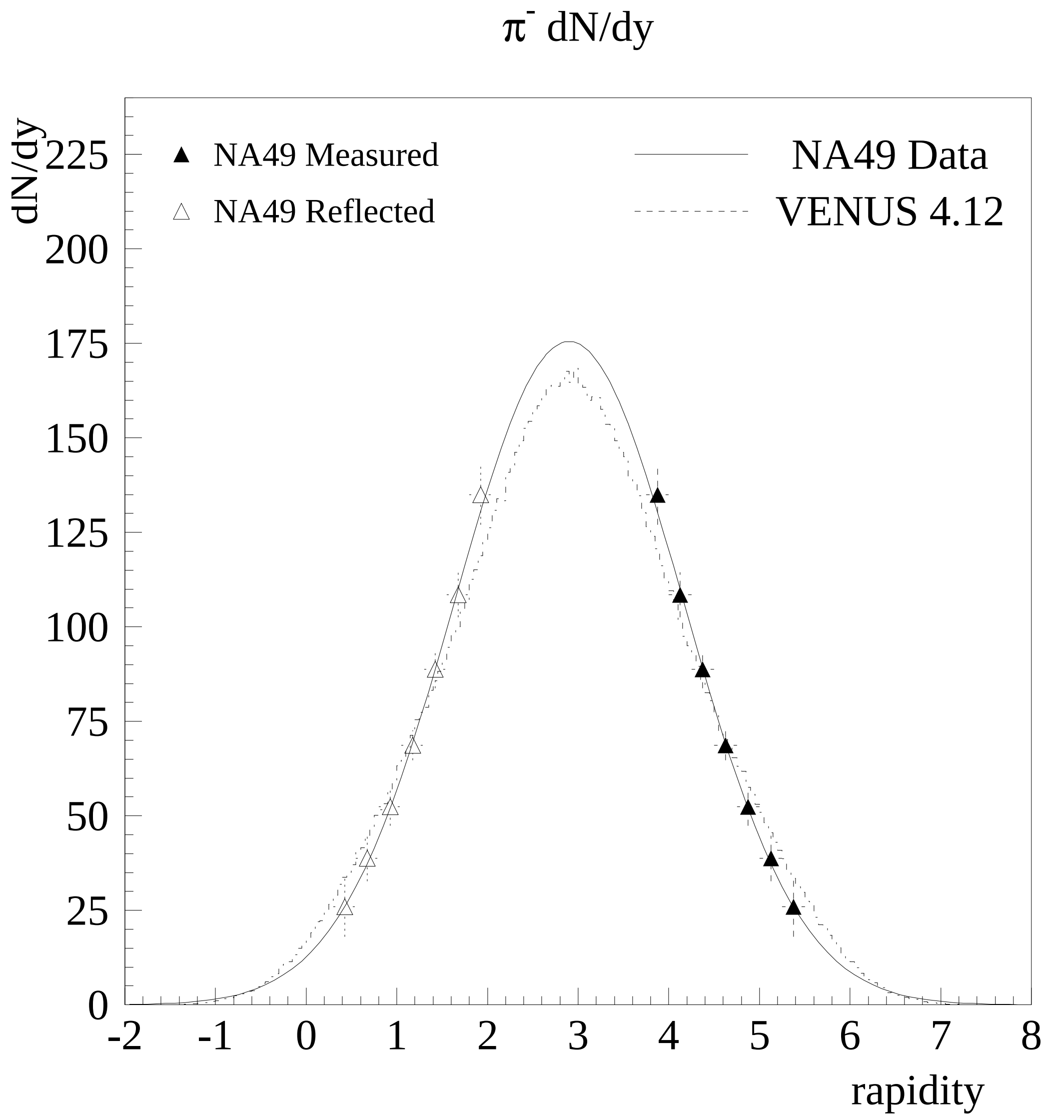

Figure 9.6: A comparison of negative pion dN/dy spectra from VENUS and the NA49 dE/dx analysis(excluding the low-p_T excess).

although a bit below the dE/dx yields from the single exponential fits.

9.3 NA44/NA49 Coulomb Effect Comparison

In truly heavy-ion collisions, such as the Pb+Pb collisions at NA49, the large amount of positive charge in the system can introduce additional distortions of the final particle distributions. The force of the Coulomb interation between the positively charged protons and the positive and negative pions will be manifest as a distortion of the final momentum spectra of these pions. The results of this distortion from the NA49 dE/dx analysis were presented in $\oint$ 8.6, and the results are again shown here in Fig. 9.7. The data are shown for 3 different rapidity slices from $4.25 < y < 5$ in order to analyze the rapidity dependence of the Coulomb distortion for the Pb+Pb system. Recent results published by the NA44 collaboration are shown in Fig. 9.8 in the rapidity range $3 < y < 4.1$. The experimental ratios π^-/π^+ are shown for different colliding systems, which are from top to bottom:

- 158 A·GeV/c Pb+Pb collisions
- 200 A·GeV/c S+Pb collisions
- 200 A·GeV/c S+S collisions

As can be seen in the data the Coulomb distortion for the smaller Z systems of S+S and S+Pb are minimal, whereas the distortions are substantial for the high Z symmetric Pb+Pb collisions. The NA44 Pb+Pb pion spectral distortions have been explained by introducing a longitudinal co-moving charge of $Z_{eff} = 40$ per unit rapidity in a model calculation[Bear96]. This is in agreement with the published NA44 stopping spectrum[Bear96b], which found a dN/dy for stopped protons of $\sim$ 35-40 around mid-rapidity.

Recall that the NA49 Coulomb distortions shown in Fig. 9.7 are not at mid-rapidity, but more than a unit away from mid-rapidity. In order to qualitatively understand if the Coulomb distortions should be more or less than the NA44 distortions at mid-rapidity, we would need to know how much charge has been stopped to these rapidities. The preliminary NA49 proton stopping spectra is shown in Fig. 9.9. This distribution is derived from a simple plus-minus-minus analysis. In strong interactions, the total baryon number is conserved, i.e. all initial baryons must reappear in the final state. Together with the other 'good' quantum number, the total electric charge, the extraction of the net proton rapidity density is achieved by subtracting the spectra of positive(h+) and negative(h-) hadrons, the '(+)-(-)' method. An additional correction is made for the K^+/K^- asymmetry. The K^+/K^- asymmetry has been found to be $\sim$ 1.6 from the kink and TOF analyses. The π^-/π^+ assymetry, which is $\sim$ 1.06 is not addressed in this analysis. A more accurate '(+)-(-)' method is presently being pursued, where the pions are identified and removed and then a subtraction is done.

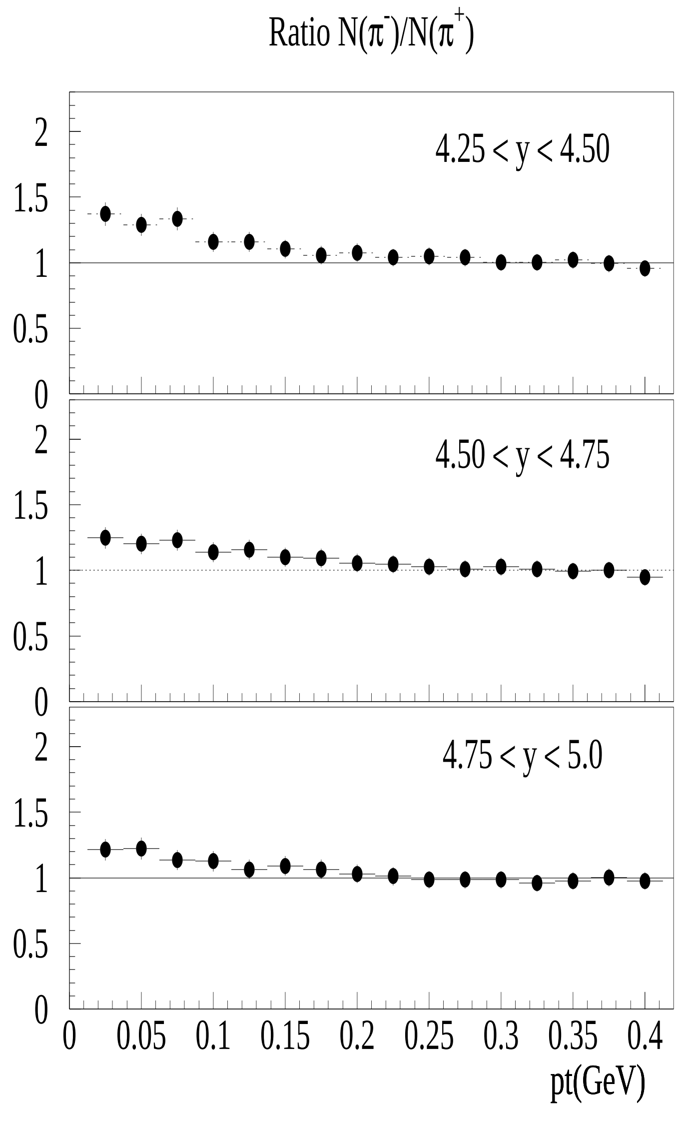

Figure 9.7: Coulomb effect on positive and negative pions in the rapidity range $4.25 < y < 5$.

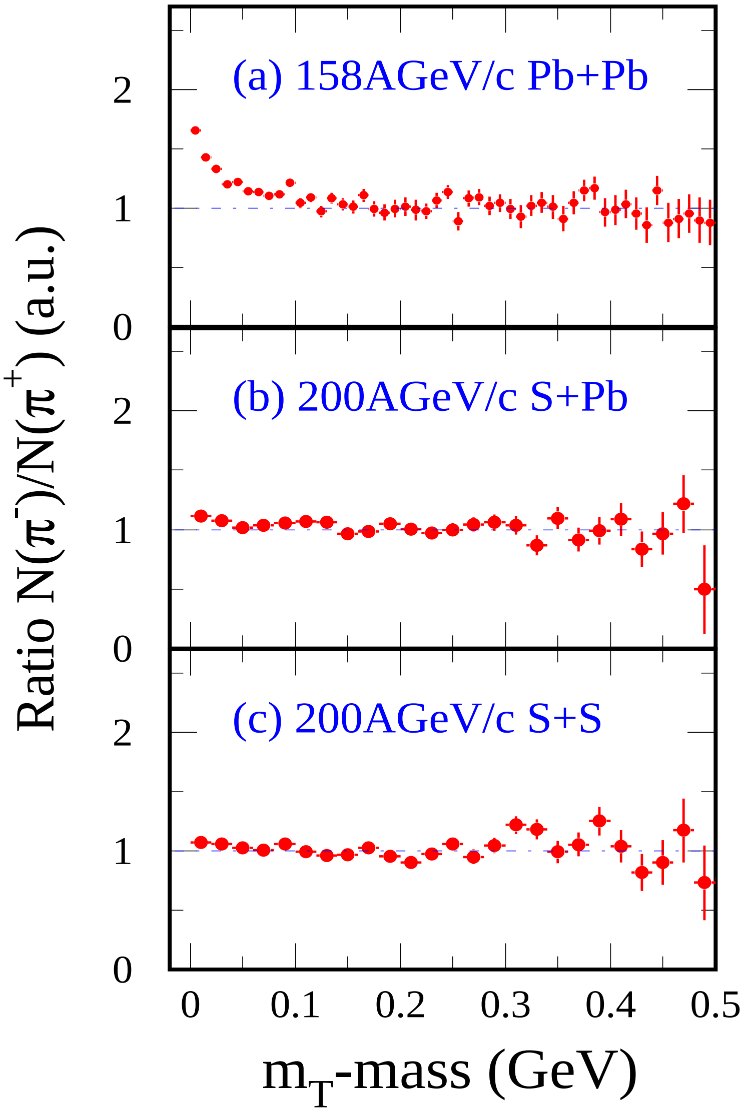

Figure 9.8: Experimental Ratios π^-/π^+ from (a) 158 A·GeV/c Pb+Pb collisions, (b) 200 A·GeV/c S+Pb collisions, and (c) 200 A·GeV/c S+S collisions. The data are arbitrarily normalized to unity at high p_T.

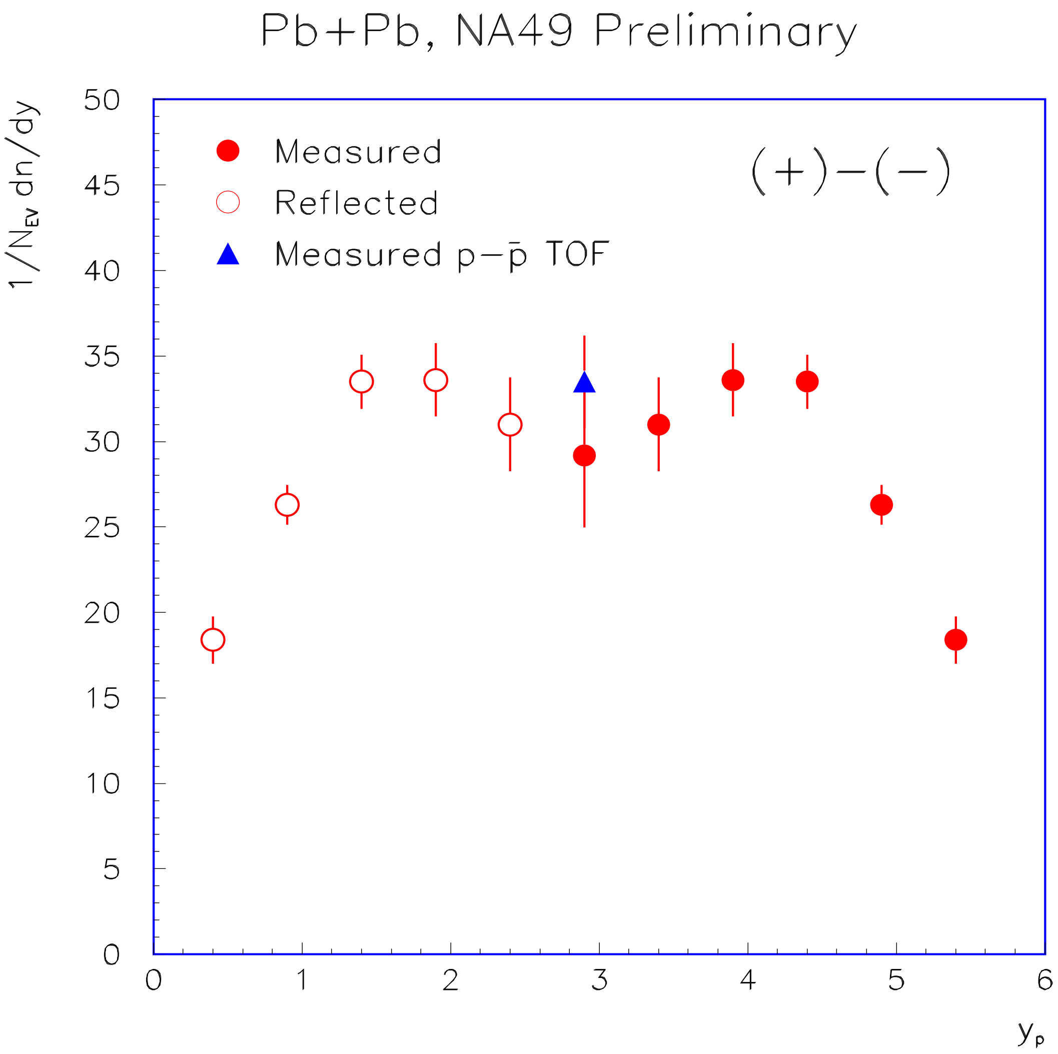

Figure 9.9: The preliminary NA49 stopping spectrum, extracted from a plus-minus-minus analysis.

The NA49 stopping spectra is slightly lower than the NA44 stopping spectra, with a dN/dy of protons around 30-35 at mid-rapidity. The central plateau of baryons extends from mid-rapidity to a rapidity of $\sim$ 4.5, at which point the dN/dy of protons starts to sharply fall off. This is in agreement with the measured Coulomb distortions in Fig. 9.7. The Coulomb effect is largest in the bin nearest mid-rapidity($4.25 < y < 4.5$), with a magnitude which is comparable to the NA44 distortions. The distortion then decreases in the next two rapidity slices, which follows from the decreasing quantity of charge(net protons) which is stopped to these rapidities.

9.4 Pion-Entropy Discussion

The most important question to answer from the latest Pb+Pb experiments is whether or not a Quark-Gluon Plasma has been formed during the reaction. In the absence of a smoking gun, several different experimental signatures are being scrutinized. In particular, Gaździcki has discussed the entropy produced in central nucleus-nucleus collisions[Gazd95b]. He concludes that the enhancement of entropy (i.e., particle) production in central S+S collisions at 200A GeV (as compared to that near 12A GeV) may be interpreted as the manifestation of an increase, by about a factor of three, in the effective number of degrees of freedom in the early stages of the collision. The transition from hadronic to partonic degrees of freedom, and the formation of a quark-gluon plasma (QGP) at some energy between that of the AGS and the SPS is hypothesized.

The Gaździcki analysis uses the formalism of the Fermi "F" variable approach previously motivated in ∮ 1.10, applying the formalism to investigate entropy production in central nucleus-nucleus collisions. The data used are compiled in[Gazd95a]. Recall that besides that in the pions, entropy is also contained in the other particles produced (mainly kaons) and is also transferred to the participant nucleons in the form of increased energy. Thus the total entropy, in units of entropy per pion, is estimated[Gazd95b] using

$$S = 3 \cdot (\langle h^- \rangle - \langle K^- \rangle) + k \cdot \langle K/\bar{K} \rangle + \delta \cdot \langle N_p \rangle \ ,$$

as in ∮ 1.10.1.

In Fig. 9.10, $S/\langle N_p \rangle$ is plotted vs. F for NN (N_p=2) and central AA collisions. This plot is essentially Fig. 5 of [Gazd95b], with the addition of SPS data from NA49 for 158A GeV Pb+Pb collisions (F = 3.81). The pion data comes from this thesis and the kaon data comes from [Marg96]. Relative to the (nearly linear) trend of the NN and the lower-energy AA data, the SPS 158A GeV Pb+Pb and 200A GeV S+S data show an enhancement of entropy production, and lie on a line of steeper slope. In the spirit of the Fermi/Landau approach used in [Gazd95b] it is natural to interpret this as an "unusual increase of the entropy density at the early stage" of the collision, and further, to assume that this is due to an increase

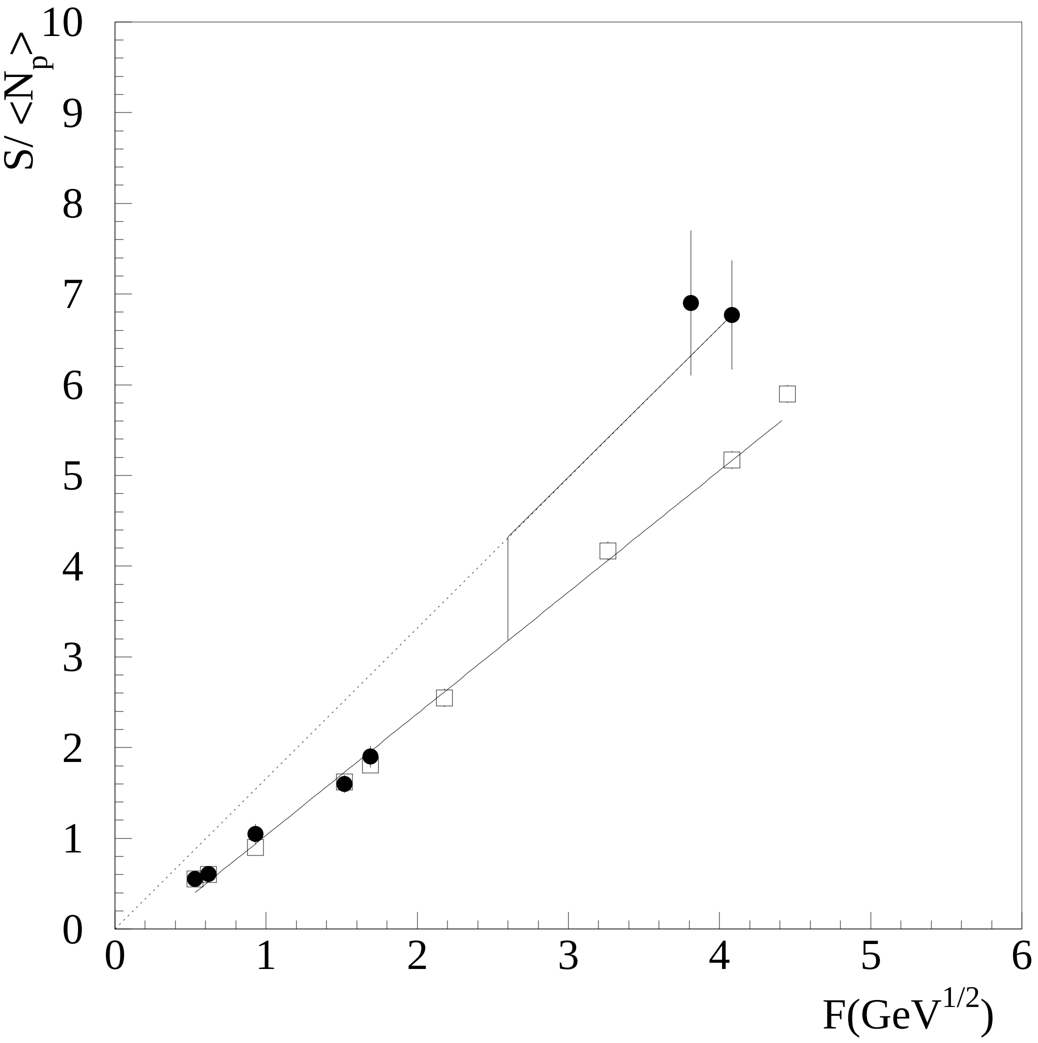

Figure 9.10: $S/ < N_p >$ is plotted vs. F for NN(open squares) and central AA(closed circles) collisions, including the NA49 point at F=3.81.

in the effective number of degrees of freedom (g) as is expected in the creation of deconfined (partonic) matter.

9.4.1 Proton-Nucleus Data

While the above interpretation is certainly plausible, it hinges upon several assumptions: e.g., that the F dependence of $\langle h^{-}\rangle_{AA}$ or $\langle\pi\rangle$ is linear in F. Clearly it is possible to fit the AA data in Fig. 9.10 with a quadratic F dependence. There is no proof that this is the correct behavior; however, this possibility is suggested by the F dependence of the pA multiplicities. Recently it has been shown[Brad97] that in pA collisions the F dependence of particle production multiplicities, $\langle h^{-}\rangle_{pA}$, also appears to be nonlinear. Since we know that QGP formation is unlikely in pA systems, the non-linear F dependence seen in both systems may be due to re-scattering or some other mechanism, and not the formation of a QGP.

9.5 Conclusion

Is the enhanced pion production seen at SPS energies in the S+S and Pb+Pb systems indicative of QGP formation? At present this question cannot be definitively answered. A similar enhancement seems to take place at high energies in pA collisions, suggesting that re-scattering may be the mechanism causing enhancement in both pA and AA collisions(and not a QGP). Similar geometrical re-scattering models have explained the so-called strangeness enhancement seen at the AGS and SPS energies[Lee88, Mats86b]. Certainly data inbetween the AGS and SPS energies will be a crucial step in trying to understand whether the enhancement in pion production seen at the SPS is a discontinuous jump or a smooth transition from lower energies. At this time, no other clear, unambiguous signatures have been presented as independent declarations that the QGP has been formed at SPS energies. Final agreement within the heavy ion community on the plasma formation will probably require either one or both of the following:

- clear, undisputable evidence of discontinuous behaviour in some observable, such as the entropy production from pions, that cannot be explained by any normal hadronic interaction
- simultaneous, but perhaps less undisputable confirmation of several of the various different proposed signatures of QGP formation

Since neither of these criteria have yet been met, the formation and existence of the QGP in the SPS Pb+Pb system cannot be confirmed.

Bibliography

[Abac95] S. Abachi and the D0 Collaboration, "Observation of the Top Quark," Fermilab preprint FERMILAB-PUB-95/028-E, 1995.

[Abe88] K. Abe et al., *Phys. Lett. B*, 200:266, 1988.

[Abe95] F. Abe and the CDF Collaboration, "Observation of the Top Quark in $p\overline{p}$ collisions with the CDF detector at Fermilab," Fermilab preprint FERMILAB-PUB-95/022-E, 1995.

[Ahle96] L. Ahle et al., Proceedings of Quark Matter '96, *Nuc. Phys. A*, 610:139c, 1996.

[Akes90] T. Akesson et al., *Z. Phys. C*, 46:361, 1990.

[Albe93] T. Alber at al., *Z. Phys. C*, 64:195, 1994.

[Albe95] T. Alber et al., *Phys. Rev. Lett.*, 75:3814, 1995.

[Alli80] W. M. Allison and J. H. Cobb, *Ann. Rev. Nucl. Part. Sci.*, 30:253, 1980.

[Ambr86] K. Ambrus, Ph.D. Thesis, Universtiy of Heidelberg, 1986.

[Bach94] J. Bachler et al., *Phys. Rev. Lett.*, 72:1419, 1994.

[Barr93] J. Barrette et al., *Phys. Rev. Lett.*, 70:2996, 1993.

[Barr94] J. Barrete et al., "Particle Spectra and Correlations from Experiment E814," Proceedings of Quark Matter '94, *Nuc. Phys. A*, 566:183c, 1994.

[Barr96] J. Barrette et al., *Nucl. Phys. A*, 610:153, 1996.

[Bear96a] I. G. Bearden et al. for the NA44 Collaboration, "Hadron Distributions - Recent Results from the CERN Experiment NA44," Proceedings of Quark Matter '96, *Nuc. Phys. A*, 610:175c, 1996.

[Bear96b] I.G. Bearden et al. and the NA44 Collaboration, *Phys. Lett. B*, in print, and CERN Preprint CERN-PPE/96-107.

[Bear97] I.G. Bearden et al. and the NA44 Collaboration, *Phys. Rev. Lett.*, 78:2080, 1997.

[Beav92] D. Beavis, et al., *Physical Review C*, 45:299, 1992.

[Bele56] S. Z. Belen'kii and G. A. Milekhin, *Soviet Physics JETP*, 2:14, 1956.

[Bies96] F. Bieser et al., "Design and Performance of TPC Readout Electronics for the NA49 Experiment," LBNL preprint LNBL-39171 UC-413, and submitted to *Nucl. Inst. and Meth.*, July 1996.

[Bjor83] J.D. Bjorken, *Phys. Rev. D*, 27:140, 1983.

[Bogg96] H. Boggild et al.(NA44 Collaboration), *Phys. Lett. B*, 372:339, 1996.

[Brad96] F. P. Brady and J. Dunn, "Effect of ADC Threshold on Cluster Charge and dE/dx," NA49 Internal Note #85, WWW and submitted to *Nucl. Instr. and Meth.*

[Brad97] F. P. Brady and J. Dunn, "Comment on Entropy Production in Nuclear Collisions," NA49 Internal Note #114, WWW and submitted to *Z. Phys. C.*

[Broc97] R. Brockman et al., "The NA49 Large Acceptance Detector for an Investigation of Pb-induced Reactions at the CERN SPS," in preparation and to be submitted to *Nucl. Inst. and Meth.*

[Brow91] G. E. Brown et al. *Phys. Lett. B*, 253:19, 1991.

[Bura80] A. J. Buras, "Asymptotic Freedom in Deep Inelastic Processes,"*Rev. Mod. Phys.*, 52:199, 1980.

[Busz84] W. Busza and A. Goldhaber, *Phys. Lett. B*, 139:235, 1984.

[Chen84] For a nice discussion see T. Cheng and L. Li, *Gauge Theory of Elementary Particle Physics*, Clarendon Press, Oxford, 1984.

[Coll84] J. C. Collins and M. J. Perry, *Phys. Rev. Lett.*, 34:1353, 1984.

[Eckh96] F. Eckhardt, Ph.D. Thesis, University of Marburg, 1996.

[Ferg95] M. I. Ferguson and H. G. Fischer, "A Brief Explanation of Kalib Factors," NA49 Internal Note #68, WWW, 1995.

[Ferm50] E. Fermi, *Prog. Theor. Phys.*, 5:570, 1950.

[Fern86] R. Fernow, *Introduction to Experimental Particle Physics*, Cambridge University Press, Cambridge, 1986.

[Fisc94] H. G. Fischer, private communication.

[Foka94] Y. Foka, Ph.D. thesis. University of Geneva, 1994.

[Gazd95a] M. Gaździcki and D. Röhrich, *Z. Phys. C*, 65:215, 1995.

[Gazd95b] M. Gaździcki, *Z. Phys. C*, 66:659, 1995.

[Gazd96a] M. Gaździcki and D. Röhrich, *Z. Phys. C*, 71:55, 1996.

[Gazd96b] M. Gaździcki, University of Frankfurt preprint IKF-HENPG/2-96.

[Gazd97] M. Gaździcki, University of Frankfurt preprint IKF-HENPG/1-97.

[Gean94] Application Software Group, *Geant User's Guide*, CERN, 1994.

[Geic89] Christoph Geich-Gimbel, *Int. Jour. of Mod. Phys.* 4:1527, 1989.

[Geis91] W. M. Geist, *Nucl. Phys. A*, 525:149c, 1991.

[Gell64] M. Gell-Mann, *Phys. Lett.*, 8:214, 1964.

[Gros73] D. Gross and F. Wilczek, *Phys. Rev. D*, 8:3633, 1973.

[Gunt94] J. Gunther, "Particle Identification by dE/dx inthe NA35 Time Projection Chamber," University of Frankfurt preprint IKF-HENPG/8-94.

[Gyul84] For a survey, see M. Gyulassy, *Nucl. Phys. A*, 418:59c, 1984.

[Gyul95] M. Gyulasssy, "Quark Matter 95: Concluding Remarks," Proceedings of Quark Matter '95, Nucl. Phys. A, 590:431c, 1995.

[Hage83] R. Hagedorn, *Z. Phys. C*, 17:265, 1983.

[Harr96] For a review see J.W. Harris, "Scaling of Nuclear Stopping in Central Nucleus-Nucleus Collisions from E_{lab} = 0.25 - 160 A-GeV," *Proceedings of the 12th Winter Workshop on Nuclear Dynamics, (Snowbird, UT)*, 1996.

[Hein88] U. Heinz, K. Lee and M. J. Rhoades-Brown, *Phys. Rev. C*, 37:1452, 1988.

[Hemm94] T. Hemmick for the E814 Collaboration, "Low p_t Pion Enhancement in ^{28}Si + Pb Collisions at 14.6 A·GeV/c," Proceedings of Quark Matter '94, *Nuc. Phys. A*, 566:435c, 1994.

[Huan95] I. Huang, S. Margetis, P. Seyboth and D. Vranic, "Reduction of the Calorimeter Data with ^{208}Pb + Pb Projectiles at 158 GeV/Nucleon in the CERN Experiment NA49," LBNL preprint LBL-36877, UC-414, March 1995.

[Jaco93] P. Jacobs, "GNA49 - NA49 Geant, Version 2", NA49 Internal Note #22, WWW, 1993.

[Jone96] P. Jones and the NA49 Collaboration, "Hadron Yields and Hadron Spectra from the NA49 Experiment," Proceedings of Quark Matter '96, *Nucl. Phys. A*, 610, 1996.

[Kars95] F. Karsh, *Nucl. Phys. A*, 590:367c, 1995.

[Klar85] A. Klar and J. Hufner, *Phys. Rev. D*, 31:491, 1985.

[Kran88] For example see Ch. 9.2 of *Introductory Nuclear Physics,* K. Krane, John Wiley and Sons, New York, 1988.

[Kueh95] A. Kuhmichel, unpublished, "Electronics Calibration in NA49", NA49 Internal Documentation, 1995.

[Land53] L.D. Landau and I. Akad, *Nauk. SSSR, Ser. Fitz.*, 17:51 and 17:56, 1953(See also Collected Papers of L. D. Landau, Nos. 74 and 88, ed. D. Ter Haar, Pergamon, Oxford, 1965.).

[Lasi95] B. Lasiuk, "Magnetic Field Mapping Status Report," *NA49 Collaboration Meeting*, Munich, March 29, 1995.

[Lee88] K. Lee, M. Rhoades-Brown, and U. Heinz, *Phys. Rev. C*, 37:1452, 1988.

[Lehr83] I. Lehraus et al., *IEEE Trans. Nuc. Sci*, 30:50, 1983.

[Lete92] J. Letessier, A. Tounsi, J. Rafelski, *Phys. Lett. B*, 292:417, 1992.

[Lete93] J. Letessier, A. Tounsi, U. Heinz, J. Sollfrank, and J. Rafelski, *Phys. Rev. Lett.*, 70:3530, 1993.

[Lete94] J. Letessier, J. Rafelski, and A. Tounsi, *Phys. Rev. C*, 50:406, 1994.

[Mada84] R. Madaras and P. Oddone, *Physics Today*, August, 1984.

[Marg96] S. Margetis and the NA35 and NA49 collaborations, "Kaon Production in S+Nucleus and Pb+Pb Collisions at CERN SPS," presented at *Strangeness '96*, Budapest, Hungary, 1996.

[Marz83] C. de Marzo et al., *Nucl. Inst. and Meth.* , 217:405, 1983.

[Mats86a] T. Matsui and H. Satz, *Phys. Lett. B*, 178:416, 1986.

[Mats86b] T. Matsui, B. Svetitsky, and L. McLerran, *Phys. Rev. D*, 34:2047, 1986.

[Mock96] A. Mock, "dE/dx Status Report," NA49 Spring Collaboration Meeting, Munich, 1996.

[Murr94] M. Murray for the NA44 Collaboration, "Single Particle Spectra from NA44," Proceedings of Quark Matter '94, *Nuc. Phys. A*, 566:515c, 1994.

[Namb74] Y. Nambu, *Phys. Rev. D*, 10:4262, 1974.

[OPAL87] OPAL Collaboration, *Nucl. Instr. and Meth. A*, 260:329, 1987.

[Pome51] I. Ya. Pomeranchuk, *Dokl. Akad. Sci USSR*, 78:884, 1951.

[Rai90] G. Rai et al., *IEEE Trans. Nucl. Sci.*, 36:58, 1989.

[Rauc94] W. Rauch, *IEEE Trans. Nucl. Sci.*, 41:30, 1994.

[Renf96] R. Renfordt et al., "The NA49 Laser System," NA49 Internal Note # 90, WWW, 1996.

[Salm93] A. Salmeron, *Nuc. Phys. B*, 389:301, 1993.

[Satz90a] For a recent survey, see H. Satz in *Quark Gluon Plasma*, R. C. Hwa(Ed.), World Scientific, Singapore, 1990.

[Satz90b] H. Satz, "Heavy Ion Physics at Very High Energies," Proceedings of the Large Hadron Collider Workshop, CERN preprint CERN 90-10, ECFA 90-133.

[Shur80] E. V. Shuryak, *Phys. Rep. C*, 61:71, 1980.

[Simo94] J. Simon-Gillo, *Nuc. Phys. A*, 566:175c, 1994.

[Soll90] J. Sollfrank, P. Koch, and U. Heinz, *Phys. Lett. B*, 252:256, 1990.

[Soll95] J. Sollfrank and U. Heinz, "The Role of Strangeness in Ultrarelativistic Nuclear Collisions," CERN preprint NUC-TH/9505004, 1995.

[Stac96] J. Stachel, "Tests of Thermalization in Relativistic Nucleus-Nucleus Collisions," Proceedings of Quark Matter '96, *Nuc. Phys. A*, 610:509c, 1996.

[Ster71] R. M. Sternheimer and R. F. Peierls, *Phys. Rev. B*, 3:3682, 1971.

[Stoc91a] R. Stock et al., NA49 Proposal, CERN preprint CERN/SPSLC 91-31, SPSLC/P264.

[Stoc91b] R. Stock et al., Addendum to CERN-Proposal SPSLC/P264, CERN/SPSLC 91-52, SPSLC/P264 Ad. 1.

[Suss79] L. Susskind, *Phys. Rev. D*, 20:2610, 1979.

[Toot87] W. Toothacker, *Phys. Lett. B*, 197:295, 1987.

[Toy94] M. Toy, "MTPC Tracking Environment," NA49 Internal Note #45, WWW, 1994.

[vanH84] L. van Hove, CERN preprint CERN-TH 4055/84.

[Vide95] F. Videbaek et al. for the E866 Collaboration, "Recent Results from E866," Proceedings of Quark Matter '95, *Nuc. Phys. A*, 590:249c, 1995.

[Wale79] A. H. Walenta, J. Fischer, H. Okuno and C. L. Wang, *Nucl. Instr. and Meth.*, 161:45, 1979.

[Wein73] S. Weinberg, *Phys. Rev. Lett.*, 31:494, 1973.

[Weni95] S. Wenig, "NA49 Gas System", NA49 Spring Collaboration Meeting, CERN, 1995.

[Wern87] K. Werner, et. al., *Zeitschrift Für Physik C*, 37:57, 1987.

[Whit95] C. Whitten, unpublished, "Note on Electron Energy Deposited at Sites of ^{83}Kr Decay," NA49 Internal Documentation, 1995.

[Wien96] T. Wienold and the NA49 Collaboration, "Stopping and Collective Effects at SPS Energies," Proceedings of Quark Matter '96, *Nucl. Phys. A*, 610, 1996.

[Wils74] K.G. Wilson, *Physical Review D*, 10:2445, 1974.